Eddy-driven transports in the Antarctic Circumpolar Current system

Dissertation
zur Erlangung des Doktorgrades
der Mathematisch-Naturwissenschaftlichen Fakultät
der Christian-Albrechts-Universität zu Kiel

vorgelegt von
Jan Viebahn

Kiel, 2012

Referent/in: Prof. Dr. Carsten Eden
Koreferent/in: Prof. Dr. Peter Brandt

Tag der mündlichen Prüfung: 30.01.2012
Zum Druck genehmigt: 30.01.2012

gez. Prof. Dr. Lutz Kipp, Dekan

für Johanna

Contents

Eidesstattliche Erklärung ix

Acknowledgement xi

Zusammenfassung xiii

Summary xv

1 Introduction 1

1.1 Climate change . . . 1
1.2 The ocean's role in a changing climate system . . . 2
1.3 The Antarctic Circumpolar Current system . . . 5
1.4 Climate models and parameterisations . . . 7
1.5 The SO carbon sink and a possible Southern Hemisphere feedback mechanism 9
1.6 MOC streamfunctions . . . 12
1.6.1 Standing-eddy-free streamfunctions . . . 12
1.6.2 Streamfunctions directly computed in Eulerian space . . . 14

2 Towards the impact of eddies on the response of the Southern Ocean to climate change 17

2.1 Abstract . . . 17
2.2 Introduction . . . 18
2.3 Theoretical framework . . . 22
2.3.1 Residual-mean theory . . . 22
2.3.2 Eddy-flux closure . . . 24
2.3.3 Diagnostic model . . . 26
2.4 Numerical model and experiments . . . 28
2.4.1 Idealised numerical ACC model . . . 28
2.4.2 Experiments . . . 32

2.5 Results . . . 34
2.5.1 Eddy compensation effect . . . 34
2.5.2 Impact of horizontal resolution . . . 40
2.5.3 Effects of different eddy diffusivity parameterisations . . . 42
2.5.4 Sensitivity of the diagnostic model . . . 47
2.6 Summary and conclusions . . . 48

3 Standing eddies in the meridional overturning circulation 53
3.1 Abstract . . . 53
3.2 Introduction . . . 54
3.3 Idealised numerical SO model and experiments . . . 56
3.4 Eulerian streamfunction and mean buoyancy . . . 57
3.5 Isopycnal streamfunctions . . . 59
3.5.1 Transient and standing eddies . . . 62
3.5.2 MOCs with reduced standing eddy circulation . . . 66
3.6 Summary . . . 79
3.7 Conclusions . . . 82
3.8 Appendix . . . 83
3.8.1 General horizontal zonal integration paths . . . 83
3.8.2 No-normal-flow boundary condition in curvilinear coordinates and condition (ii) of section 3.5.2 . . . 84
3.8.3 The isopycnal streamfunction defined in isopycnal coordinates . . . 85

4 Residual-mean eddy streamfunction and quasi-Stokes streamfunction 87
4.1 Abstract . . . 87
4.2 Introduction . . . 87
4.3 Models and experiments . . . 90
4.4 Residual-mean framework . . . 91
4.4.1 NL case . . . 93
4.4.2 Flat case . . . 96
4.4.3 Hill case . . . 98
4.4.4 Series number . . . 100
4.5 Quasi-Stokes streamfunction . . . 102
4.5.1 Comparison of ψ^* and Ψ^* . . . 103

4.5.2 Differences between the series expansions of ψ^* and Ψ^* in model experiments . . . 105
4.5.3 Ψ^* in model experiments computed from an isopycnal framework . 107
4.6 Summary and discussion . . . 108
4.7 Appendix . . . 111
4.7.1 Outline of the residual-mean framework . . . 111
4.7.2 The quasi-Stokes streamfunction . . . 114

5 Synthesis **117**

Author contributions **123**

List of Figures **125**

List of Tables **131**

Bibliography **133**

Eidesstattliche Erklärung

Hiermit erkläre ich, dass ich die vorliegende Arbeit - abgesehen von der Beratung durch meinen Betreuer - selbstständig verfasst und keine weiteren Quellen und Hilfsmittel als die im Quellenverzeichnis angegebenen verwendet habe.
Diese Arbeit hat weder ganz, noch in Teilen, bereits an anderer Stelle einer Promotionskommission zur Erlangung des Doktorgrades vorgelegen.
Ich erkläre, dass die vorliegende Arbeit gemäß den Grundsätzen zur Sicherung guter wissenschaftlicher Praxis der Deutschen Forschungsgemeinschaft erstellt wurde.

Acknowledgement

Many thanks to ...

... **Carsten Eden** for providing the opportunity to realise this thesis, for all the scientific input, support, patience, guidance and constructive criticism throughout the last years and the freedom to decide on the scientific direction of this thesis.

... **Richard Greatbatch** and **Claus Böning** for always taking the time to help me with my concerns.

... **Klaus Getzlaff**, **Torben Kunz** and **Lars Czeschel** for a lot of scientific discussions and non-scientific chats, help on everyday problems, proof-reading and motivational backing.

... **the members of the TM group**, especially Sabine Niewels and Annegret Schurbohm, for a very friendly working atmosphere.

... **the staff of the IFM-GEOMAR**, especially the computing center staff (first of all Simone Knief), library staff and cleaners, for ensuring the necessary infrastructure.

... my **family** and **friends** for love and support.

Funding through DFG-SPP1158 and BMBF-SOPRAN is gratefully acknowledged.

Zusammenfassung

Diese Dissertation besteht aus drei Forschungsartikeln. Der erste Forschungsartikel behandelt entscheidende Fragen der gegenwärtigen Klimawandel-Diskussion: Wie reagiert die meridionale Umwälzzirkulation (MOC) des Südlichen Ozeans (SO) auf dekadisch-skalige Trends im Windstress-Antrieb? Inwieweit ist es den gegenwärtigen Parameterisierungen von meso-skaligen Wirbeln möglich, die entsprechenden Veränderungen im Wirbelfeld in Klimamodellen wiederzugeben? Die Ergebnisse eines idealisierten Modells des SO, für welches sowohl Wirbel zulassende wie parameterisierte Konfigurationen aufgesetzt wurden, zeigen, dass der Wirbel-getriebene Anteil der MOC dem Wind-getriebenen Anteil im Allgemeinen entgegengesetzt ist und dass die Zunahme der MOC mit stärker werdenden Winden abnimmt. Daraus ergibt sich die Möglichkeit der völligen Unabhängigkeit der MOC des SO von Änderungen im Windstress. In der Wirbel zulassenden Modellkonfiguration ist jedoch für mäßig starke Winde noch eine signifikante Zunahme der MOC zu erkennen. Die parameterisierten Modellkonfigurationen können die MOC für bestimmte Windstresse reproduzieren, jedoch wird die Abhängigkeit der MOC vom Windstress durch jede der betrachteten Parameterisierungen überschätzt. Die Ergebnisse zeigen: Um die richtige Abhängigkeit der MOC vom Windstress zu reproduzieren, ist es notwendig, die korrekte Sensitivität des Wirbelfeldes in Klimamodelle einzubeziehen. Den aktuellen Parameterisierungen von meso-skaligen Wirbeln gelingt dies jedoch nur ansatzweise.

Die Forschungsartikel zwei und drei stehen in einer konzeptionelleren Perspektive und konzentrieren sich auf eine der verbreitetsten Diagnostiken der MOC: das Konzept der MOC Stromfunktion. Der zweite Forschungsartikel klärt die Frage: Ist es möglich, eine MOC Stromfunktion zu definieren, welche gänzlich frei von stehenden Wirbeln ist? Es wird gezeigt, dass eine MOC Stromfunktion mit einem exakt verschwindenden stehenden Wirbel-Anteil dadurch erhalten wird, dass die zonale Integration entlang von tiefenabhängigen horizontalen Isolinien der zeitlich gemittelten Dichte ausgeführt wird. Dagegen führt die Integration entlang von zeitlich gemittelten geostrophischen Stromlinien, welche üblicherweise zur Neutralisierung des stehenden Wirbel-Anteils benutzt wird, im Allge-

meinen nur zu einer MOC Stromfunktion mit einem reduzierten stehenden Wirbel-Anteil.

Im letzten, dritten Forschungsartikel werden die zwei gebräuchlichsten Ansätze zur Berechnung von MOC Stromfunktionen direkt im Euler-Raum betrachtet: die Reihenentwicklung der residuellen Wirbelstromfunktion und die Reihenentwicklung der quasi-Stokes Stromfunktion. Unter Benutzung der Resultate von verschiedenen idealisierten Wirbel zulassenden zonalen Kanalmodellen werden die beiden Reihenentwicklungen bis zur dritten Ordnung der Dichtestörungen verglichen. Beide Stromfunktionen können in den Modellkonfigurationen mit flachem Boden im Ozeaninneren angemessen durch die führenden Terme der ersten oder zweiten Ordnung angenähert werden, wobei jedoch auch Terme dritter Ordnung die implizierte Zirkulation im Inneren noch signifikant beeinflussen. Desweiteren sind die Unterschiede im Ozeaninneren zwischen den beiden Reihenentwicklungen bis zur dritten Ordnung klein. Dagegen unterscheiden sich die führenden Terme in den Oberflächen- und Bodenrandbereichen deutlich. In solchen Regionen sind die ersten Terme der beiden Reihenentwicklungen von alternierendem Vorzeichen und zunehmendem Betrag, so dass die Näherungsausdrücke dort versagen. In realistischeren Modellkonfigurationen mit signifikanten topographischen Gebilden ergeben sich auch im Ozeaninneren physikalisch inkonsistente Rezirkulationszellen, welche nicht durch Terme nächst höherer Ordnung reduziert werden. Folglich ist die Diagnose der MOC aus empirischen Daten oder Resultaten realistischer Modelle durch Näherungen der residuellen Wirbelstromfunktion oder der quasi-Stokes Stromfunktion vorsichtig zu interpretieren, wenn nicht sogar zu verwerfen.

Summary

This PhD thesis consists of three research papers. The first research paper addresses crucial issues of the present climate change debate, namely the response of the meridional overturning circulation (MOC) of the Southern Ocean (SO) to decadal-scale trends in wind stress forcing, and the ability of up-to-date meso-scale eddy parameterisations to represent the corresponding changes in the eddy field in climate models. Results from an idealised SO model in both eddy-permitting and parameterised configurations show that the MOC is characterised by an eddy-driven part which generally opposes the wind-driven part and that the increase of the MOC diminishes with amplifying winds, with the possibility that the MOC in the SO may become completely insensitive to wind stress changes. However, for moderate wind stress, the MOC is still significantly increasing in the eddy-permitting model configuration. The parameterisations are able to reproduce the MOC for certain wind stresses, but all parameterisations overestimate the sensitivity of the MOC on wind stress. The results show that it is indispensable to incorporate the correct sensitivity of eddy field into climate models in order to reproduce the correct sensitivity of the MOC to wind stress and that up-to-date meso-scale eddy parameterisations are only partially successful.

The second and third research papers are guided by a more conceptual perspective and focus on one of the most common diagnostics of the MOC: the concept of the MOC streamfunction. The second research paper clarifies the question: Is it possible to define a MOC streamfunction completely void of standing eddies? It is shown that the construction of a MOC streamfunction with an exactly vanishing standing eddy part has to be performed by zonal integration along depth-dependent horizontal isolines of time-mean density. In contrast, zonal integration along time-mean geostrophic streamlines, typically applied to neutralise the impact of standing eddies, generally only leads to a MOC streamfunction with a reduced standing eddy part.

Finally, the third research paper considers the two most common approaches to calculating MOC streamfunctions directly in Eulerian space: the series expansion of the residual-

mean eddy streamfunction and the series expansion of the quasi-Stokes streamfunction. Using several idealised eddy-permitting zonal channel model experiments, the two series are compared up to third order in buoyancy perturbation. In model configurations with flat bottom, both streamfunctions may be well approximated by the first one or two leading order terms in the ocean interior, although terms up to third order still significantly impact the implied interior circulations. Further, differences in both series expansions up to third order remain small here. Near surface and bottom boundaries, on the other hand, the leading order terms differ and are initially of alternating sign and of increasing magnitude such that the low order approximate expressions break down there. In more realistic model configurations with significant topographic features, physically inconsistent recirculation cells also appear in the ocean interior and are not effectively reduced by the next higher order terms. Therefore, the diagnosis of the MOC from empirical data or realistic model results via approximations of the series expansion of the residual-mean eddy streamfunction or the series expansion of the quasi-Stokes streamfunction must be treated with care or even completely ruled out.

1 Introduction

1.1 Climate change

During the last two decades, the topic *climate change* has represented a global social discourse[1] and has served as a primary motivation for research in environmental sciences. A consensus has been reached in the scientific community (Oreskes, 2004) on an anthropogenic climate change over the past century: As reviewed and assessed by the IPCC (2007), a definite warming of the climate system since the mid-20th century is obvious from observations of increases in global average air and ocean temperatures, broad melting of snow and ice, and rising global average sea level. Additionally, global atmospheric concentrations of greenhouse gases have increased significantly (primarily carbon dioxide (CO_2), methane and nitrous oxide) as a result of human activities since the mid-18th century. At present time, they by far exceed pre-industrial values determined from polar ice cores dating back 650,000 years. It is very likely that this observed increase in anthropogenic greenhouse gas concentrations represents the main cause for the changes in the energy balance of the climate system which led to the observed warming. The primary sources of the increased global atmospheric CO_2 concentration since the pre-industrial period result from fossil fuel use and land use change, while those of methane and nitrous oxide are primarily due to agriculture.

Beside the observed increase in global average temperatures, further probably human-induced long-term and regional-scale changes in climate have been observed. These include strongly increased Arctic temperatures and decreased Arctic sea ice extent, widespread changes in precipitation, ocean salinity, extreme weather events and wind patterns. Regarding other aspects of climate, like the Antarctic sea ice extent or the meridional overturning circulation (MOC) of the global ocean, there is insufficient evidence to determine whether trends exist. Moreover, changes in key processes that drive global and regional

[1] The Intergovernmental Panel on Climate Change (IPCC) was first established in 1988 and in 1992 the UN Framework Convention on Climate Change (UNFCCC) was adopted.

climate changes are hardly clarified (e.g. El Niño-Southern Oscillation (ENSO), North Atlantic oscillation (NAO), Southern Annular Mode (SAM)) and require further investigation.

1.2 The ocean's role in a changing climate system

The ocean as a key component of the climate system[2] plays a major role also in anthropogenic climate change (Siedler et al., 2001; IPCC, 2007):

First, due to the large heat capacity of the ocean, the time scales of climate change are largely controlled by ocean heat storage. The ocean is able to accumulate heat largely in accord with the radiation imbalance resulting from the increasing concentrations of greenhouse gases and, hence, delays the full global warming. Correspondingly, observations since 1961 show that the average temperature of the global ocean has increased to depths of at least 3000 m and that the increase in ocean heat content (see Fig. 1.1) accounts for more than 90% of the increase in heat content of the earth system (mainly stored in the upper 700 m of the ocean). IPCC (2007) model scenarios show that even if all radiative forcing agents were held constant at present levels, a significant further warming trend would occur mainly due to the slow response of the ocean.

Second, sea-level rise represents a major argument in the political debates on anthropogenic climate change. It endangers the coastal areas where most of the world population lives, especially those regions where accompanying coastal erosion, flooding and increases in storm surges may occur. Observations suggest that global average sea-level rose at an average rate of 1.8 ± 0.5 mm per year over 1961 to 2003. The total 20th-century rise is estimated to be 0.17 ± 0.05 m, although the observed sea-level change shows substantial spatial variation due to geographically non-uniform changes in temperature, salinity, ocean circulation and surface atmospheric pressure. On decadal and longer time scales, global average sea-level change results from changes in the volume of water in the global ocean as a consequence of changes in the density or the total mass of the ocean. The dominant cause of global sea-level rise over the period 1993 to 2003 is estimated to be thermal expansion of seawater (i.e. a change in density) due to large-scale ocean warming. Additional

[2] About 71% of the earth's surface is covered by the different components of the ocean (including up to 6% coverage by sea ice). Therefore, absorption of solar energy, which drives the earth's climate system, is inter alia dominated by the ocean. In general, the ocean's important role in the climate system results from its ability to store and transport large amounts of heat, freshwater, and radiatively active gases around the globe and exchange these with the atmosphere.

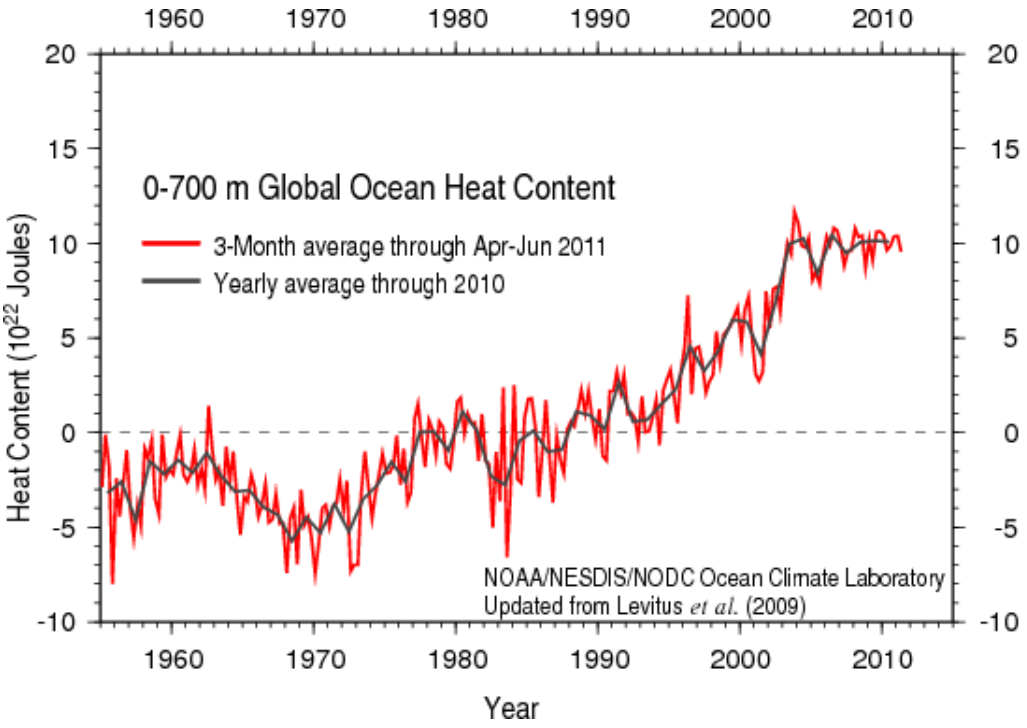

Figure 1.1: Empirical estimate of the world ocean heat content for 1955-2008 from Levitus et al. (2009).

factors contributing to recent sea-level rise are related to the increase of the total mass of the ocean and include the melting of glaciers and ice caps, changes in land water storage, and ice mass losses from the ice sheets of Greenland and Antarctica. Sea-level rise due to thermal expansion is expected to continue for many centuries, due to the time required to transport heat into the deep ocean. IPCC (2007) models actually project global sea-level to rise during the 21st century at a greater rate than during 1961 to 2003, with the main source being thermal expansion.

Third, changes in the ocean's regional pattern of heat transport and absorption, resulting from the ocean not being in balance with the changed radiative forcing, will lead to significant changes in regional climate. Thus precipitation pattern and possibly main modes of climate variability relying on ocean-atmosphere coupling (e.g. ENSO) will change. Additionally, climate variability related to the dominant modes of large-scale atmospheric variability (e.g. NAO, SAM) may be influenced.

Fourth, changes in the formation of deep watermasses at high latitudes in the North Atlantic and the Southern Ocean could lead to changes in the global MOC (see Fig. 1.2) and a major rearrangement of global climate. IPCC (2007) climate model simulations suggest

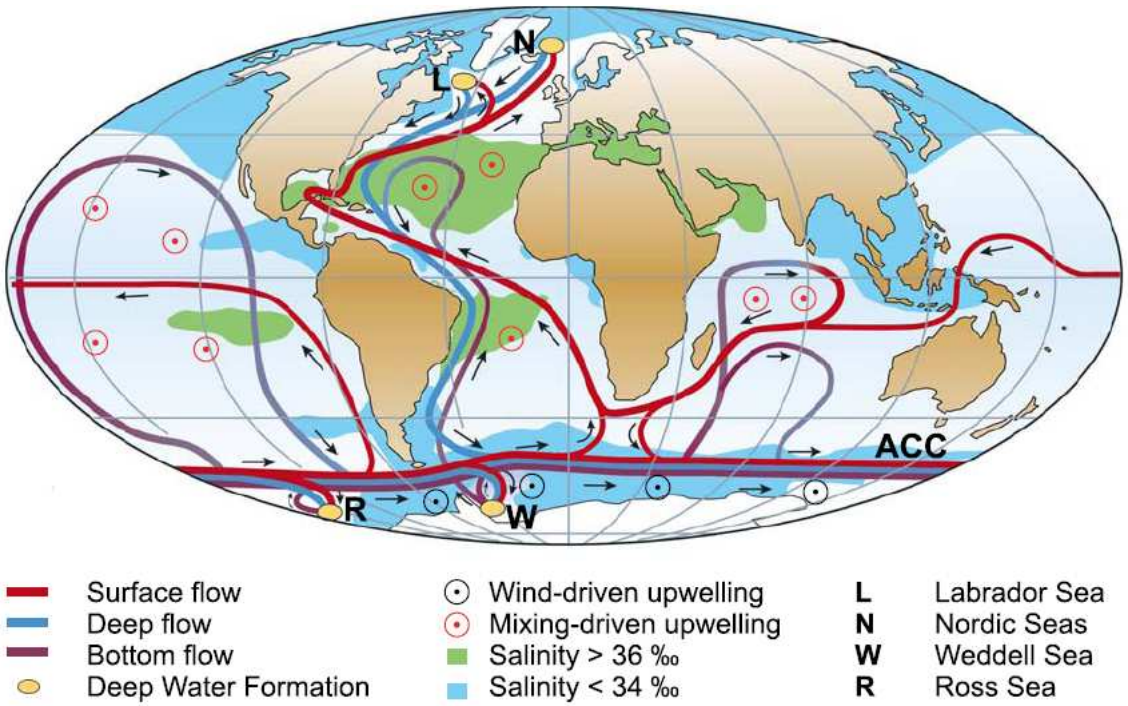

Figure 1.2: Strongly simplified sketch of the global overturning circulation system from Kuhlbrodt et al. (2007). The circulation that leads to a continuous renewal of the waters in the deep ocean by the sinking of dense waters to the abyssal ocean at high latitudes in the North Atlantic (L, N) and near Antarctica (W, R), and by widespread upwelling of these watermasses elsewhere is called global MOC. Wind-driven upwelling occurs along the Antarctic Circumpolar Current (ACC). The MOC is considered to be crucial in the climate system e.g. due to its role in the poleward heat transport and the ventilation of the deep ocean.

that the MOC transport might gradually decrease in the 21st century as a consequence of anthropogenic warming and additional freshening in the North Atlantic. However, observations of changes in MOC transport, water properties and watermass formation are ambiguous about changes in the MOC strength due to decadal variability, which obscures the long-term trend, and due to inadequate long-term observations. Therefore, over the last 50 years no clear evidence for a trend in the mean strength of the MOC could be diagnosed.

Fifth, changes in the ocean uptake or release of radiatively active gases such as CO_2 can directly feed back to the earth's climate system. The ocean is a major sink for anthropogenic CO_2 and it is estimated to store about one third of the CO_2 released annually through human activities (around 2 GtC/yr). While the rate at which the ocean stores

CO_2 increases as the atmospheric concentration rises, how and where the ocean takes up CO_2 depends on the evolution of ocean conditions (e.g. temperature and salinity, alkalinity, vertical stability, circulation and biological processes) which are influenced by, and are influencing, a changing atmosphere. Factors limiting the oceanic uptake of CO_2 are the rate at which the gas can be transferred across the air-sea interface[3] and the rate at which carbon is transported from the surface layer to the deep ocean. Since ocean currents can transport CO_2 over large distances, the location of storage of carbon may be distant from the site of air-sea exchange (see Fig. 1.3). In particular, because of the limited rate of vertical transport in the ocean, more than half of the anthropogenic carbon can still be found in the upper 400 m and is absent in most of the deep ocean. In general, there are three principal mechanisms by which dissolved gases such as CO_2 (as well as heat and freshwater) may be transported by the ocean: In the North Atlantic the overturning circulation (related to deep convection) is considered to be the dominant mechanism, while in the North Pacific the intense western boundary current related to the gyre circulation represents the primary motor. Finally, in the Southern Ocean the time-variable ocean eddies are suggested to be the dominant feature in the meridional tracer transport. The focus of this PhD thesis lies on the Southern Ocean (SO), to which we turn in the next section.

1.3 The Antarctic Circumpolar Current system

The SO is the region south of 30° S and connects the Atlantic, Indian and Pacific Oceans via a circulation feature which is central in the ocean's role in climate: the Antarctic Circumpolar Current system. Its horizontal flow, the eastward flowing Antarctic Circumpolar Current (ACC), is the largest ocean current on earth in terms of mass transport ($\sim 130 - 140$ Sv) and geographical extent (~ 24000 km) and is often reaching to the bottom and is therefore strongly influenced by bottom topography. The weaker flows in the meridional-vertical plane constitute the southern component of the global MOC, where deep waters ascend southward across the ACC, upwell to the surface at the poleward flank of the ACC and then either travel equatorward and transform to intermediate and mode water or move closer to Antarctica, transform to dense bottom water and propagate near the bottom to the adjacent northern ocean basins. The upwelling, associated with strongly

[3] The nonlinearity in carbon chemistry reduces the CO_2 uptake capacity of water as its CO_2 concentration increases. Moreover, the ocean is able to take up more CO_2 at lower temperatures.

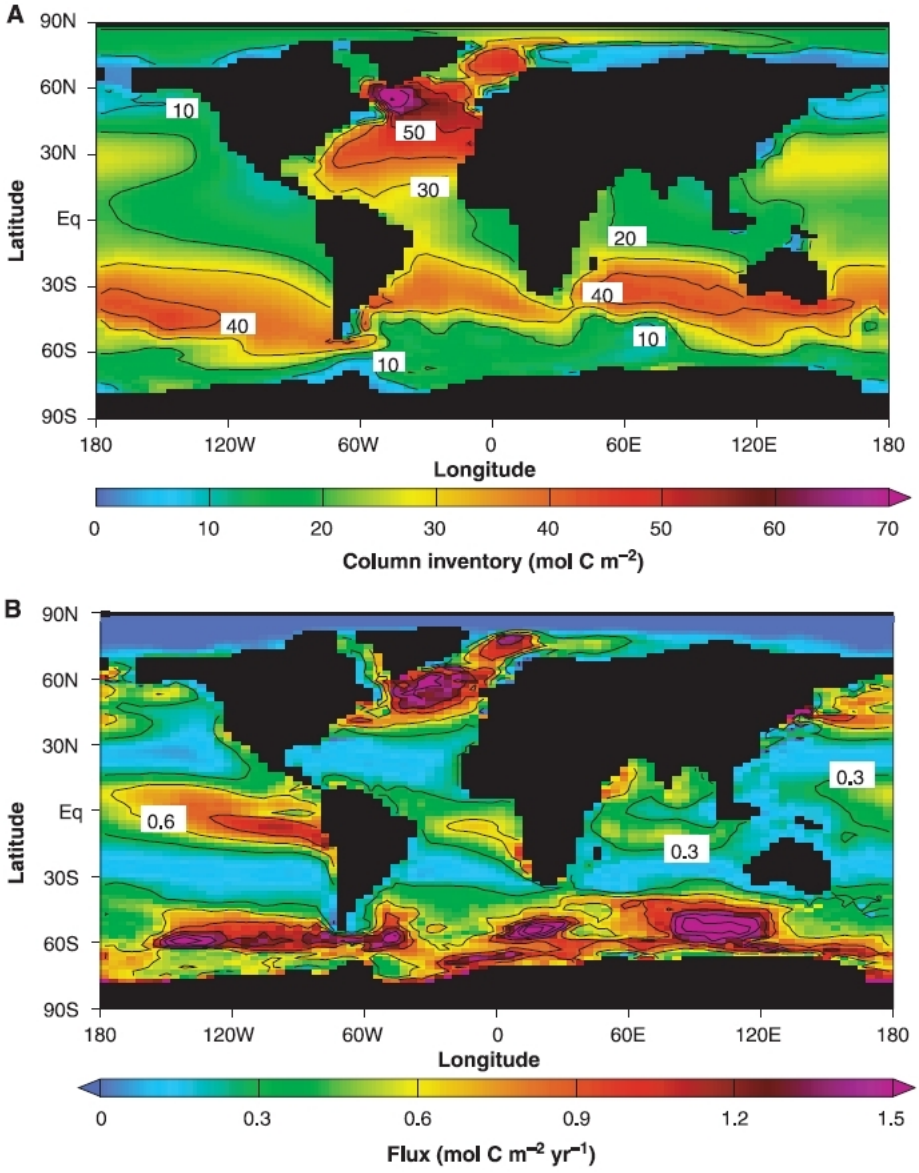

Figure 1.3: (A) Column inventories and (B) air-sea fluxes of anthropogenic carbon simulated in an ocean-climate model by Caldeira and Duffy (2000). Maximum air-sea fluxes of anthropogenic carbon into the Southern Ocean occur farther south than maximum column inventories. Note that the column inventories are in good agreement with empirical estimates e.g. by Sabine et al. (2004).

tilted surfaces of constant density in the meridional direction, connects the deep watermasses of the world ocean to the surface and, hence, the southern MOC is of fundamental importance for the meridional-vertical heat, freshwater and tracer transports and thus

the corresponding large-scale budgets in the SO. In particular, the understanding of the strength and variability of the MOC in the SO is mandatory to quantify the role of the SO in the global carbon budgets and to predict future anthropogenic carbon uptake by the ocean (Orr et al., 2001).

The ACC system is forced by both strong westerly winds and surface buoyancy fluxes over the SO. Moreover, the absence of land barriers in the latitude band of Drake Passage leads to dynamics which are distinct from those of the rest of the world ocean and with eddies capturing a central role. In the SO, eddy-driven transports can be as large as mean transports. Meso-scale eddies play an important role in determining the transport of the ACC (Olbers et al., 2004) by transferring the stress exerted by the furious winds over the SO into the deep ocean and finally to the solid earth (Munk and Palmén, 1951; Gille, 1997a; Stevens and Ivchenko, 1997). Additionally, the central role of eddies in vertical momentum transport implies that they are also important for shaping the southern MOC, i.e. the mass and tracer transport across the ACC in the SO, as discussed by e.g. Karsten and Marshall (2002); Marshall and Radko (2003); Olbers and Visbeck (2005). Meso-scale eddy activity affects or even controls the meridional transports in the SO across the ACC and, hence, eddy-driven meridional tracer transports set the role of the SO as an oceanic sink in the global carbon cycle. Consequently, the impact of meso-scale eddies has to be adequately accounted for in ocean climate models.

1.4 Climate models and parameterisations

In ocean climate models, the meso-scale variability has to be adequately resolved or parameterised. The meso-scale eddy parameterisation by Gent and McWilliams (1990) (GM), in which the so-called thickness diffusivity K has to be specified, is used to account for such eddy-driven transports and is currently applied in almost any state-of-the-art ocean climate model which does not resolve the vigorous eddy activity in the ocean[4]. Gent and McWilliams (1990) and Gent et al. (1995) interpreted the GM parameterisation as diffusion in the isopycnal layer thickness budget[5], for which an effective (turbulent) diffusivity has to be set. It is clear that the meridional mass and tracer transports are strongly affected by

[4] See e.g. http://www-pcmdi.llnl.gov/ipcc/model_documentation/ipcc_model_documentation.php.

[5] More precisely, the GM scheme is founded by the maintenance of two properties: First, the moments of the tracer should be preserved; in particular, the amount of fluid between two isopycnal surfaces should be preserved. Hence, it is an adiabatic scheme. Second, the amount of available potential energy in the flow should be reduced in order to mimic the effects of baroclinic instability.

the choice of this thickness diffusivity, particularly in the SO where eddy-driven transports are as large as mean transports. Consequently, pathways of the ACC, watermass structures and ventilation rates in the SO are indeed rather different using different values of thickness diffusivities (England and Rahmstorf, 1998). It is therefore of crucial importance for the quantification of the role of the SO in the climate system and the global carbon cycle.

However, the value of thickness diffusivity in the SO, its magnitude, horizontal and vertical variation, is poorly known so far. Because of the sparseness of observations of interior meso-scale activity it appears to be difficult to estimate thickness diffusivity directly from available observations, although there have been attempts in the SO (Phillips and Rintoul, 2000; Marshall et al., 2006). Currently, constant values of approx. $1000\,\mathrm{m}^2/\mathrm{s}$ are typically chosen, sometimes higher in the upper ocean and lower below the thermocline, but it is clear that the thickness diffusivity should also have manifold spatial dependency (Visbeck et al., 1997; Ferreira et al., 2005). A better empirical estimate of thickness diffusivity is still needed in order to consistently model the SO with a non-eddy-resolving ocean model using the GM parameterisation.

Furthermore, a consistent eddy closure is needed for coarse resolution ocean models coupled to a climate model. Instead of prescribing fixed values of thickness diffusivity, such a closure should be based on mean quantities predicted by the ocean model itself. Such a closure is necessary in coupled climate models, since they are meant to be used under different climates (including long term climate changes and shorter term climate variability studies) and for which estimates of present thickness diffusivities are insufficient, since the values of thickness diffusivity change under different climates.

Recently, a new flow-interactive meso-scale eddy closure for K was developed by Eden and Greatbatch (2008) (EG). The closure consists of a prognostic equation for eddy kinetic energy (EKE) that is integrated as an additional model variable of the non-eddy-resolving model, and in which production, radiation and dissipation terms of the EKE budget are parameterised based on the variables of the non-eddy-resolving model. The EKE and a diagnostic eddy length scale are combined in a standard mixing length assumption for the thickness diffusivity of the GM parameterisation, following Green (1970) who first proposed the application of a mixing length approach for the eddy effect in geostrophic turbulence. Based on an empirical analysis of eddy length scales from altimeter data and as estimated from the simulation of an realistic eddy-permitting model, Eden (2007) found that the minimum of the Rossby radius and Rhines scale yields the best choice.

The EG closure was tested by Eden and Greatbatch (2008) by comparing the results of a parameterised non-eddy-permitting model version of the SO with the results of the corresponding eddy-permitting model version (Eden, 2006) and good agreement was found in terms of magnitude and horizontal and vertical structure. Moreover, the EG closure was compared to other closures by Eden et al. (2009a) and was shown to be superior with respect to its performance in the SO. However, it is at present unclear if and how the EG closure applies under changing climate conditions. Therefore, in the first research paper of this PhD thesis the validity and the performance of the EG closure is assessed for decadal-scale trends in the SO which are described in the following section.

1.5 The SO carbon sink and a possible Southern Hemisphere feedback mechanism

Recent studies indicate that the SO is the largest sink of anthropogenic CO_2, together with mid- to high-latitude regions in the North Atlantic (Gloor et al., 2003; Mikaloff Fletcher et al., 2006). But only half of the anthropogenic CO_2 absorbed by the SO is stored there, due to strong northward transport (Sabine et al., 2004; Mikaloff Fletcher et al., 2006) (see Fig. 1.3). Hence, the understanding of the strength and variability of the MOC in the SO is mandatory to quantify the role of the SO in the global carbon budgets and to predict future anthropogenic carbon uptake by the ocean. In fact, the response of the ACC system and the carbon sink in the SO to changes in wind stress and surface buoyancy fluxes is under debate: Coming along with an observed decadal-scale warming of the surface and also deep SO (Gille, 2002, 2008), a strong decadal scale trend of weakening anthropogenic CO_2 uptake by the SO was recently estimated from ocean model simulations and atmospheric inversions by Le Quéré et al. (2007) and Lovenduski et al. (2007) with considerable effects on global warming. Le Quéré et al. (2007) and other authors relate the trend in the CO_2 sink in the SO to positive trends in the strength of the westerly winds over the SO, the prevailing winds between the latitudes of 30° S and 60° S, during recent decades (Thompson and Solomon, 2002), which are in turn related to an upward trend in a large-scale atmospheric pattern known as the Southern Annular Mode (SAM[6])

[6] Climate variability in the high-latitude SH is strongly related to the SAM, the dominant mode of large-scale atmospheric variability in the SH extratropics. The structure and variability of the SAM results mainly from the internal dynamics of the atmosphere and it is associated with synchronous pressure anomalies of opposite sign in mid- and high-latitudes, and therefore reflects changes in the main belt of subpolar westerly winds. The imprint of SAM variability on the SO system is observed as a coherent

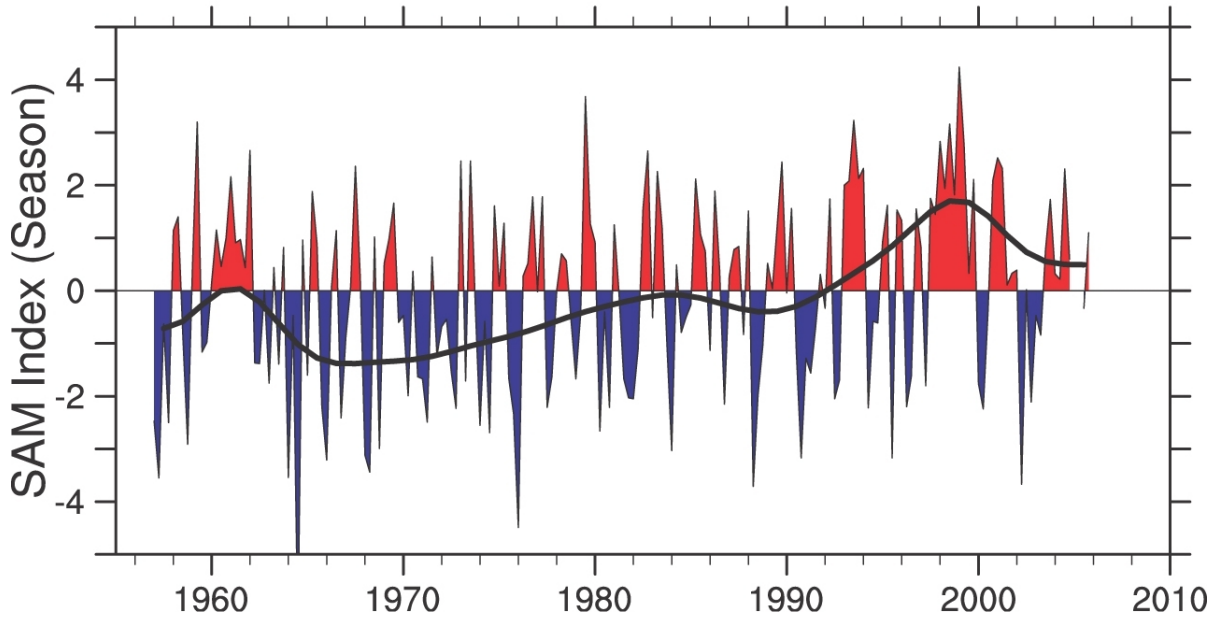

Figure 1.4: Seasonal values of the SAM index calculated from station data (updated by the IPCC (2007) from Marshall (2003)). The smooth black curve shows decadal variations. Enhanced SO westerlies occur in the positive phase of the SAM.

(see Fig. 1.4). The decadal-scale increase in wind stress drives more equatorward Ekman transport and thus more upwelling of carbon-rich deep watermasses which in turn leads to a decreased uptake of CO_2. It is clear that the ocean CO_2 sink will persist as long as atmospheric CO_2 increases, but the fraction of the CO_2 emissions that the ocean is able to absorb may decrease if the observed intensification of the SO winds continues in the future and consequently the level at which atmospheric CO_2 will stabilise may be higher. Since the observed shifting of the SAM index toward a higher index state has been related to (anthropogenic) greenhouse gas increases (Marshall et al., 2004; Saenko et al., 2005; Fyfe et al., 2007; IPCC, 2007), with stratospheric ozone depletion being another possible cause (Thompson and Solomon, 2002), the overall scenario may represent in part a positive feedback mechanism towards larger atmospheric CO_2 concentrations.

On the other hand, the meridional, cross frontal transports in the SO are strongly affected or even controlled by meso-scale eddy activity which opposes the impact of the Ekman transport. Hence, a key question for the possible future carbon source in the SO

sea level response around Antarctica and by its regulation of ACC flow through the Drake Passage. Corresponding changes in oceanic circulation may explain recent patterns of observed temperature change at SH high latitudes described by Gille (2002, 2008) (IPCC, 2007).

is the response of the meso-scale eddy field to the changes in wind stress. In the coarse resolution models of Le Quéré et al. (2007) and Lovenduski et al. (2007), the thickness diffusivity of the GM parameterisation is fixed, i.e. not flow-interactive such that the response of the parameterised eddy-field in those models is in question. In fact, it was demonstrated by Hallberg and Gnanadesikan (2006) that eddy-permitting models, and in particular the MOC in those models, do respond rather differently to changes in surface wind stress compared to non-eddy-permitting models in which the eddy-driven MOC is parameterised by GM. It is possible that the wind-driven increase in the MOC is completely counterbalanced by a similar increase in the eddy-driven MOC (Hallberg and Gnanadesikan, 2001, 2006), such that the carbon sink of the SO would stay more or less constant. It is clear that the model based estimates of the future fate of the carbon sink in the SO by Le Quéré et al. (2007) and Lovenduski et al. (2007) are strongly controlled (and biased) by the choice of the fixed thickness diffusivity.

Consequently, the aims of the first research paper of the PhD thesis are the following: To obtain a better understanding of the future changes of the MOC, and in particular the future fate of the CO2 sink of the SO,

- we assess the response of the (eddy-driven) MOC in the SO to decadal-scale trends in wind stress forcing in an idealised eddy-resolving model of the SO and

- we explore the ability of the recently developed parameterisation of Eden and Greatbatch (2008) to represent the corresponding changes in the eddy field in climate models, by simulating the same decadal-scale trends in the SO in a corresponding parameterised non-eddy-permitting ocean model of the SO.

While the first research paper addresses crucial issues of the present climate change debate, namely the possible role of the MOC in the SO in a changing climate, the second and third research papers take a step back and are guided by a more conceptual perspective: One of the most common diagnostics of the MOC is the concept of the MOC streamfunction. The second and third research papers want to further clarify certain difficulties and possible optimisations of the most prominent definitions of the MOC streamfunction, as sketched in the following final section of the introduction.

1.6 MOC streamfunctions

The overall MOC is given by a three-dimensional flow field (varying in time) which is generally not zonally uniform but consists of many kinds of flows and counterflows of various watermasses at different longitudes. In order to produce a compact picture (enabling an efficient diagnosis) of the MOC, one mostly considers a zonal-mean streamfunction[7], i.e. a two-dimensional projection of the underlying complex three-dimensional flow field onto the meridional-vertical plane. The zonal average is typically defined in the geometrically simplest manner via zonal integration along latitude circles. However, the interpretation of the resulting meridional-vertical circulation must be treated with care and not taken to be typical of the flows found near any particular longitude: Each resulting circulation cell may be a superposition of several different circulation cells and this may lead to an over- or underestimation or even to the emergence of unphysical pictures of the overall watermass movement. Nevertheless, the ultimate aim of the zonal-mean streamfunction approach is, of course, to extract the essential physical aspects of the overall MOC. Depending on the different possible physical foci, several streamfunction definitions (i.e. an ensemble of different streamfunctions) may be necessary in order to provide an appropriate diagnosis of the structure of the overall MOC. This fundamentally requires a precise understanding of the effects of different zonal averaging procedures, i.e. how different types of zonal integration extract different physical aspects of the overall three-dimensional fluid motion, which therefore has been the subject of several studies (Döös and Webb, 1994; McIntosh and McDougall, 1996; McDougall and McIntosh, 1996, 2001; Karoly et al., 1997; Nurser and Lee, 2004a,b; Eden et al., 2007; Nycander et al., 2007; Döös et al., 2008).

1.6.1 Standing-eddy-free streamfunctions

In general, in a time-zonal-mean framework the overall eddy field consists of two parts: The transient eddy component of a quantity represents the deviation from the time-mean of that quantity. Furthermore, any time-mean or steady quantity may be decomposed into a zonal-mean part and a corresponding deviation, where the latter is the so-called standing eddy component. For example, the typical zonal-mean streamfunctions may be decomposed into a time-zonal-mean component, a standing eddy component and a transient component

[7] In general, a streamfunction is defined for two-dimensional non-divergent flows such that its isolines represent streamlines, i.e. its isolines are instantaneously tangential to the velocity vector of the flow at each point. Consequently, the spatial derivatives of a zonal-mean streamfunction give the zonal-mean "meridional" and "vertical" velocities.

(Karoly et al., 1997; Olbers and Ivchenko, 2001; Lee and Coward, 2003). However, only the transient component has the character of a turbulent (time dependent) eddy field while the standing component must be considered as part of the time-mean flow and it attributes to the eddying motion a non-local character because it includes the deviation from the zonal mean.

In the SO, topographic features force the ACC system to carry out permanent meridional excursions on its circumpolar path. This induces a major contribution of the standing eddy component in the typical zonal-mean streamfunctions which is found to dominate over the transient eddy component (Karoly et al., 1997; Olbers and Ivchenko, 2001; Lee and Coward, 2003). The dominance of the large-scale time-mean eddies over the transient eddies in the SO is also found in the analysis of the momentum and potential vorticity budgets (Marshall et al., 1993; Ivchenko et al., 1996; Gille, 1997b,a; Olbers and Ivchenko, 2001). Moreover, in the zonally averaged picture many details (e.g. the correct zonal transport) of the eastward ACC are lost (Olbers et al., 2004). Consequently, the zonal average along latitude circles does not separate the time-mean and the eddy motion in a simple way. One has to deal with an eddy component which dynamically belongs to the time-mean flow but which overrides the transient component. Moreover, in non-eddy-permitting or analytical models of the ocean circulation (regarding the SO, see e.g. Marshall and Radko (2003); Olbers and Visbeck (2005)) the standing eddy terms have to be adequately parameterised by zonally averaged quantities. Unfortunately, the standing eddy fluxes are only poorly known so that they are usually simply ignored, despite there overwhelming importance (Olbers et al., 2011).

To avoid this complication, the zonal integration paths are often redefined by attaching the coordinate system to the specific flow in order to account for the permanent meridional excursions of the flow field. The resulting convoluted averages aim to obtain a drastically reduced standing eddy component such that a much clearer separation of the flow into time-mean and transient components is produced. Analysing balances or setting up models is then conceptually simpler because standing eddies can be neglected, however, the fields (velocities, fluxes etc.) are oriented at the convoluted coordinates (Olbers et al., 2004).

Typically, an average oriented along "time-mean streamlines" is introduced, but the various studies differ in the concrete specification of the zonal integration paths. While Ivchenko et al. (1996) and Treguier et al. (2007) integrate along contours of the barotropic streamfunction, Marshall et al. (1993) use contours of the Montgomery streamfunction, Karsten and Marshall (2002) use surface geostrophic streamlines (using mean sea surface

height) and Polton and Marshall (2007) integrate along Bernoulli potential contours. In every study a single set of horizontal paths (surface contours) is used for each depth, although Lee and Coward (2003) notice that there "are problems in using surface streamlines throughout the water columns since flows below the surface do not exactly follow the surface streamlines".

Hence:

- The aim of the second research paper of this PhD thesis is to clarify the idea of neutralising the effect of the permanent meanders of the ACC (standing eddies) on the MOC of the SO by a redefinition of the zonal integration paths, in order to provide a consistent concept.

- It turns out that the construction of a MOC streamfunction with an exactly vanishing standing eddy part has to be performed by zonal integration along depth-dependent horizontal isolines of time-mean density. In contrast, zonal integration along time-mean streamlines may lead to a MOC streamfunction with a merely reduced standing eddy part.

1.6.2 Streamfunctions directly computed in Eulerian space

The two mostly considered MOC streamfunctions are the residual streamfunction (Andrews and McIntyre, 1976; Eden et al., 2007) and the isopycnal streamfunction (Townsend and Johnson, 1985; Nurser and Lee, 2004a).

The residual streamfunction is directly computed in Eulerian space via zonally averaging the buoyancy budget, i.e. the residual streamfunction advects the zonal-mean buoyancy. Physically, it is desired that, if there is no instantaneous diabatic buoyancy forcing, there should be also no diabatic effects in the zonal-mean buoyancy budget, i.e. the eddy-induced diabatic forcing should vanish too. Eden et al. (2007) (extending ideas of McDougall and McIntosh (1996); Medvedev and Greatbatch (2004)) demonstrate that this physical criterion uniquely sets the residual streamfunction, especially the associated residual-mean eddy streamfunction. However, the residual-mean eddy streamfunction is then given by a series involving fluxes of eddy buoyancy moments.

The isopycnal streamfunction is calculated by zonally integrating the meridional transports along surfaces of constant potential density (isopycnals). This is motivated by the common view of the MOC in the SO, where the movement of the watermasses in steady state is predominantly adiabatic, i.e. along mean isopycnals and not across them (Wüst,

1935; Webb and Suginohara, 2001). Consequently, the isopycnal streamfunction is originally given in latitude and buoyancy coordinates, but it may be transformed to depth coordinates by identifying each zonal-mean buoyancy value with the corresponding isopycnal's zonal-mean height (McDougall and McIntosh, 2001; Nurser and Lee, 2004b). However, in order to express the isopycnal streamfunction directly by Eulerian-mean quantities, McDougall and McIntosh (2001) and Nurser and Lee (2004b) apply a Taylor series analysis centerd around the mean height of isopycnals. Therefore, the isopycnal streamfunction may be given in two ways: On the one hand, it may be computed in an isopycnal averaging framework. On the other hand, it may be given directly in Eulerian space and is then expressed by a series expansion. Of course, this series expansion is different to the one of the residual-mean eddy streamfunction; however, both are intimately connected.

Hence, if physically meaningful streamfunctions of the MOC are sought directly in the Eulerian framework, which represents the most familiar framework, it seems that the appearance of series expansions generally represents a necessary and severe complication. Most problematic is, practically, that it is inevitable to cut off the series expansions at a certain order and hence one is left with approximate formulas. Typically, in a zonal-mean framework the first order terms of both series expansions are considered as good approximations in the nearly adiabatic ocean interior, but near horizontal boundaries (surface, bottom) the approximate formulas are found to break down, i.e. unphysical nonzero (and relatively large) values appear at the horizontal boundaries (Killworth, 2001; McDougall and McIntosh, 2001; Nurser and Lee, 2004b).

The subjects of the third research paper of this PhD thesis are the following:

- The first three orders of the series expansions of the residual-mean eddy streamfunction and the quasi-Stokes streamfunction are formally compared in order to specify essential differences between these two intimately linked streamfunctions at low orders.

- Furthermore, all terms up to the third order of both series expansions are considered in different idealised models of the SO in order to investigate the behaviour of both series expansions in different concrete model setups.

- Finally, a measure to diagnose regions in the ocean where approximations of the series expansions break down is proposed.

2 Towards the impact of eddies on the response of the Southern Ocean to climate change

This chapter is a reprint of the paper "Towards the impact of eddies on the response of the Southern Ocean to climate change" published in Ocean Modelling. Author's rights without the need to obtain specific permission from Elsevier include the right to include the journal article, in full or in part, in a thesis or dissertation[1].

Citation: Viebahn, J. and C. Eden, 2010: Towards the impact of eddies on the response of the Southern Ocean to climate change, Ocean Modell., 34, 150-165, doi:10.1016/j.ocemod.2010.05.005.

2.1 Abstract

The sensitivity of the meridional overturning circulation (MOC) of the Southern Ocean (SO) to wind stress changes is discussed. Using an idealised SO model in both non- and eddy-permitting configurations, we assess the effects of both, coarsening the horizontal resolution and implementing different parameterisations for the lateral eddy diffusivity appropriate to the Gent and McWilliams (1990) parameterisation, K. We find that the MOC is characterised by an eddy-driven part ψ^* which generally opposes the wind-driven part and that the increase of the MOC diminishes with amplifying winds, with the possibility that the MOC in the SO may become completely insensitive to wind stress changes. However, for moderate wind stress, the MOC is still significantly increasing in our configuration.

The diagnosed lateral eddy diffusivity K in the eddy-permitting version shows strong spatial variability and is increasing with increasing wind stress. Similar to the MOC (but

[1] http://www.elsevier.com/wps/find/authorsview.authors/rights as of 25.10.2011

in contrast to ψ^*) the increase of K diminishes with amplifying winds. It turns out that a small increase in the isopycnal slopes is also relevant in order to capture the correct sensitivity of ψ^* on wind stress. This relation also holds in model configurations with coarser but still eddy-permitting horizontal resolution: decreasing the horizontal resolution decreases K, but increases the isopycnal slopes such that the strength of the MOC including its sensitivity to wind stress is almost unchanged. The parameterisations are able to reproduce the MOC for certain wind stresses, but all parameterisations underestimate the sensitivity of K and thus overestimate the sensitivity of the MOC on wind stress. Our results show that it is indispensable to incorporate the correct sensitivity of K into climate models in order to reproduce the correct sensitivity of the MOC to wind stress and that up-to-date parameterisations for K are only partially successful.

2.2 Introduction

The meridional overturning circulation (MOC) of the Southern Ocean (SO) is a key component of the global overturning circulation: since the SO features an inter-basin connection it permits a global overturning, and its MOC dominates the global transport of climate-sensitive properties like heat, fresh water and dissolved gases such as carbon dioxide (Rintoul et al., 2001). Current schematic understanding of the MOC of the SO begins with the decomposition of the southward flowing Circumpolar Deep Water into Upper Circumpolar Deep Water (UCDW) and Lower Circumpolar Deep Water (LCDW) to constitute two limbs of the deep overturning circulation (see Fig. 2.1): in the upper limb UCDW flows poleward and upward across the eastward flowing Antarctic Circumpolar Current (ACC) and upwells to the surface at the poleward flank of the ACC. It then travels equatorward in the surface Ekman layer beneath the strong westerly winds and is exposed to air-sea buoyancy fluxes. This contact with the atmosphere transforms UCDW into less dense Antarctic Intermediate Water (AAIW) or Subantarctic Mode Water (SAMW) which subducts in turn downward and equatorward at the equatorward flank of the ACC into the main thermocline near the Subantarctic Front.

In the lower limb, LCDW upwells closer to Antarctica and then transforms due to convective and diabatic processes occurring in narrow regions near the continental shelves around Antarctica into denser Antarctic Bottom Water (AABW) which then flows equatorward near the bottom. The interior circulation of the UCDW is likely to be nearly adiabatic and oriented along density surfaces (Webb and Suginohara, 2001) and therefore reflects

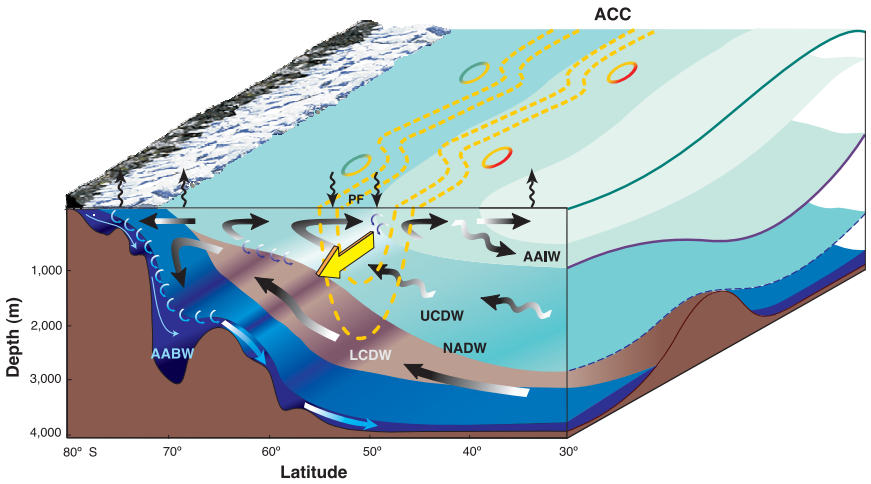

Figure 2.1: Schematic representation of the MOC of the SO. Further details are given in the text. Redrawn from Olbers and Visbeck (2005).

the shape of the isopycnals. Associated with the MOC of the SO is a density field characterised by an poleward increase of the surface density and strongly tilted isopycnals across the ACC, which almost all outcrop around Antarctica such that density surfaces connect the deep ocean to the north of the ACC with the surface areas to the south (Gouretski and Jancke, 1998).

The wind, buoyancy and eddy forcing (and a possible contribution by diapycnal mixing) controls the magnitude and direction of the MOC and the stratification in the SO. The strong westerly winds over the SO drive a large equatorward surface Ekman transport across mean streamlines of the ACC and produce divergent transports associated with upwelling south of the ACC and convergent transports associated with downwelling north of the ACC. In addition, air-sea buoyancy fluxes provide the necessary diabatic forcing for watermass transformation (Speer et al., 2000). The potential energy stored in the sloping isopycnals of the ACC due to wind and buoyancy forcing is released through baroclinic instability such that the meso-scale eddies generated by this process act to flatten the isopycnals. Since Reynolds stresses appear too small, it is believed that meso-scale eddies (as interfacial form stresses) provide the balancing of horizontal fluxes of heat and vertical fluxes of momentum (Munk and Palmén, 1951; Olbers and Ivchenko, 2001), and therefore accomplish a major task in shaping the MOC of the SO.

The upwelled deep watermasses are exposed to air-sea fluxes and, after crossing the ACC, descend into the ocean interior again, ventilating the intermediate and abyssal depths of the southern hemisphere oceans. This process is a key component of the physical part of

the marine carbon cycle in the SO. Considerable outgassing of CO_2 is found in observational estimates of natural air-sea CO_2 fluxes at high southern latitudes ($> 44°$S), such that the SO becomes a CO_2 source in pre-industrial climate (Mikaloff Fletcher et al., 2007). This outgassing is likely driven by the upwelling of waters with high concentrations of remineralised dissolved inorganic carbon (DIC), from which a substantial fraction can escape into the atmosphere since the carbon uptake by biology at the surface (and drawdown to depth) in the SO is slow and inefficient because of limitation of light and micro nutrients. Another process contributing to the outgassing is the surface warming poleward of the ACC which raises the partial pressure of carbon dioxide. In contrast, the SO is currently a region of large uptake of anthropogenic CO_2 (Caldeira and Duffy, 2000; Sabine et al., 2004; Mikaloff Fletcher et al., 2006) since the deep upwelled watermasses have low anthropogenic CO_2 content, and cold surface waters and strong winds enhance the air-sea gas transfer. The near cancellation between substantial outgassing of natural CO_2 and strong uptake of anthropogenic CO_2 results in a small contemporary CO_2 sink in the SO (Gloor et al., 2003; McNeil et al., 2007; Gruber et al., 2009). Column inventories of anthropogenic CO_2 suggest that the formation and transport of mode and intermediate waters is the primary mechanism for transporting anthropogenic CO_2 to intermediate depths in the SO while deep water formation, that is deep convection activity near the Antarctic continental shelf plays a minor role (Caldeira and Duffy, 2000).

The response of the SO carbon sink to recent climate change is under debate. Several recent studies (Le Quéré et al., 2007; Lovenduski et al., 2008) identify a strong decadal scale trend toward a weakening of the SO CO_2 sink and suggest the following scenario: the ability of the SO to take up anthropogenic CO_2 have decreased in the last two decades due to a climate-change induced poleward shift and intensification of westerly winds over the SO (Thompson and Solomon, 2002) enhancing the MOC of the SO and therefore the upwelling of deep waters rich in DIC. This process elevates the oceanic partial pressure of CO_2 in the surface waters which leads to a decreased uptake of CO_2 by the SO.

Since many coupled climate models consistently find a continuation of the trend toward stronger, poleward shifted winds over the SO for the next decades (Meehl et al., 2007; Fyfe and Saenko, 2006), a detailed understanding of the MOC of the SO and its response to wind changes is necessary to quantify the role of the SO in the global CO_2 budgets and to project future anthropogenic CO_2 uptake by the ocean. Climate, i.e. coarse-resolution ocean models indeed reproduce the suggested scenario: an increase in the slopes of density surfaces across the ACC as a dynamic adjustment to a poleward shift and

intensification of the Southern Hemisphere westerlies (a positive trend in the Southern Annular Mode index), related to an increase in ACC transport and an southward shift of its mean position (Fyfe and Saenko, 2006; Saenko et al., 2005). The MOC of the SO in these models is increased, governed by the effect of enhanced northward Ekman transport, with an enhanced downwelling of surface waters north of the ACC, and upwelling of deep water rich in DIC south of the ACC (Oke and England, 2004; Zickfeld et al., 2007; Lovenduski et al., 2007, 2008).

However, this behaviour is under debate since none of these models used to study the response of the SO carbon sink to changes in wind forcing resolve meso-scale eddies. Instead, the meso-scale eddy parameterisation by Gent and McWilliams (1990) is implemented where a fixed lateral eddy diffusivity K is used to account for the meso-scale variability and its effect on the MOC of the SO. High-resolution models permitting meso-scale eddies demonstrate that the MOC in these models does respond rather differently to changes in surface wind stress compared to non eddy-permitting models in which the eddy-driven MOC is parameterised (Hallberg and Gnanadesikan, 2006). They suggest that the increase in northward Ekman transport caused by stronger westerly winds might be (partly) compensated by the meso-scale eddy effect, which may result in only a small change in mean transport and overturning (Hallberg and Gnanadesikan, 2006; Hogg et al., 2008). Furthermore, observational studies find that stronger westerly winds induce an increase in eddy activity (Meredith and Hogg, 2006) and that upwelling, isopycnal slopes and ACC transport appear to be insensitive (on timescales longer than a few years) to changes in wind forcing (Böning et al., 2008) suggesting a strong effect of wind-induced increases in eddy activity. Thus, projecting the behaviour of the SO and its carbon sink in greenhouse scenarios will require models that capture realistically the response of the meso-scale eddy field of the ACC to the changes in wind stress.

The aims of this study are: (i) to simulate and to understand the response of the eddy-driven MOC of the SO to decadal-scale trends in wind stress and (ii) to explore the representation of these changes in the context of meso-scale eddy parameterisation of Gent and McWilliams (1990) using a fixed lateral eddy diffusivity K versus a flow-interactive parameterisation of K proposed by Eden and Greatbatch (2008), in order to clarify the representation of the effect of eddies on the simulated circulation and watermass characteristics of coarse resolution (climate) models. Therefore, we simulate the response of the meso-scale eddy field and the eddy-driven MOC of the SO to the changes in wind stress using both, eddy-permitting and parameterised non-eddy-permitting models.

This study is structured as follows: in the next section, we discuss the theoretical framework assessing the MOC, that is, the residual-mean theory by Andrews and McIntyre (1976) and the diagnostic model of the MOC of the SO by Marshall and Radko (2003) as well as the eddy parameterisations given by Gent and McWilliams (1990) and Eden and Greatbatch (2008). In the following section we describe the numerical models and the design of the numerical experiments. In the fourth section, we present the results. The last section provides a summary and conclusions.

2.3 Theoretical framework

2.3.1 Residual-mean theory

In the common view of the MOC of the SO, the movement of the watermasses in the ocean interior in steady state is along mean isopycnals (Wüst, 1935; Webb and Suginohara, 2001). Watermasses are transported advectively along isopycnals where meso-scale eddies may provide an additional transport via a bolus velocity (Gent et al., 1995). In order to obtain a physically meaningful overturning cell in a zonal average the use of density coordinates instead of depth coordinates would thus be necessary. As an alternative, McIntosh and McDougall (1996) show that to second order in a perturbation expansion, the circulation averaged in density coordinates is equal to the so-called residual circulation in depth coordinates, given by the residual mean streamfunction

$$\psi_{res} = \overline{\psi} + \psi^* \ , \tag{2.1}$$

where $\overline{\psi}$ represents the overturning streamfunction in depth coordinates, the so-called Eulerian streamfunction, and ψ^* represents the eddy streamfunction (Andrews and McIntyre, 1978b)

$$\psi^* = \frac{\overline{v^*b^*}\partial_z\overline{b} - \overline{w^*b^*}\partial_y\overline{b}}{(\partial_y\overline{b})^2 + (\partial_z\overline{b})^2} \ . \tag{2.2}$$

Here, v and w are the meridional and vertical velocities, b is the buoyancy, the overbar represents an average (zonally and in time) and the star represents the deviation from the zonal average. The corresponding meridional and vertical residual velocities are given by

$$v_{res} = -\partial_z\psi_{res} \ , \qquad w_{res} = \partial_y\psi_{res} \ , \tag{2.3}$$

and accordingly for $\overline{v}, \overline{w}$ and v^*, w^*, given by their streamfunctions $\overline{\psi}$ and ψ^*, respectively. In the residual-mean formulation ψ_{res} advects the mean tracer, $\overline{b}$. The steady-state buoyancy residual-mean equation reads

$$J(\psi_{res}, \overline{b}) = \nabla \cdot (\kappa \nabla \overline{b}) + q_b \ , \tag{2.4}$$

where $J(A, B) = \partial_y A \partial_z B - \partial_z A \partial_y B$; q_b represents buoyancy forcing due to air-sea fluxes and small-scale mixing, which might be expressed by a divergence of a vertical buoyancy flux B, with $q_b = \partial_z B$, and

$$\kappa = -\frac{\overline{v^* b^*} \partial_y \overline{b} + \overline{w^* b^*} \partial_z \overline{b}}{(\partial_y \overline{b})^2 + (\partial_z \overline{b})^2} \ . \tag{2.5}$$

Equation (2.4) can be interpreted as a reformulation of the steady and zonally averaged buoyancy equation by separating the eddy buoyancy flux $(\overline{v^* b^*}, \overline{w^* b^*})$ into a diapycnal component $-\kappa \nabla \overline{b}$ of diffusive nature and an isopycnal part $-\psi^*(-\partial_z \overline{b}, \partial_y \overline{b})$ of advective nature. In the ocean interior $\kappa \approx 0$ is expected and it follows for the eddy streamfunction

$$\psi^*|_{\kappa=0} = \frac{\overline{v^* b^*}}{\partial_z \overline{b}} = -\frac{\overline{w^* b^*}}{\partial_y \overline{b}} \quad \text{for } \kappa = 0. \tag{2.6}$$

The vertically integrated (from depth z to the surface) steady and zonally averaged zonal momentum equation is given by

$$-f\overline{\psi} = \tau - \tau_s - \mathcal{F} - \mathcal{R} \ , \tag{2.7}$$

where f is the Coriolis parameter, τ is the zonally averaged zonal wind stress and τ_s is an unspecified subgrid-scale stress. $\mathcal{F}$ is the bottom form stress which accounts for zonal pressure differences at topographic obstacles, and $\mathcal{R}$ represents the Reynolds-stress and momentum advection. For the case that $\mathcal{R}$ and τ_s are small and since $\mathcal{F}$ is only relevant near the bottom topography, the zonal momentum balance simplifies to $\overline{\psi} \approx -\tau/f$ above bottom topography.

The meridional, cross frontal transports in the SO are strongly affected or even controlled by meso-scale eddy activity (Olbers and Ivchenko, 2001): considering only the impact of the Eulerian circulation $\overline{\psi}$, that is the Ekman transport, the deep watermasses would upwell from the bottom to the surface in a more or less vertical pathway. This circulation is sometimes called the Deacon Cell of the SO (Döös and Webb, 1994). It appears rather

unphysical since the flow would cross isopycnals in the interior. This conflict can be resolved by including the effect of the meso-scale eddy circulation ψ^* which acts to redirect the wind-driven MOC such that the residual flow, i.e. the sum of the mean, wind-driven and the eddy-driven circulation, is along the mean isopycnals. In fact, it was found that the residual MOC is much weaker than the wind-driven part only, i.e. the eddy-driven MOC is partly compensating the wind-driven one (Olbers and Ivchenko, 2001; Karsten and Marshall, 2002; Treguier et al., 2007). Thus, in a highly eddying region such as the ACC, it is the residual flow rather than the Eulerian flow that should be considered.

2.3.2 Eddy-flux closure

In coarse-resolution models, the effect of the meso-scale eddy field has to be adequately parameterised. It is current practise to use the meso-scale eddy parameterisation by Gent and McWilliams (1990) in non-eddy-permitting ocean models. The Gent and McWilliams (1990) parameterisation assumes that the meridional eddy buoyancy flux $\overline{v^*b^*}$ is directed down the meridional gradient of mean buoyancy

$$\overline{v^*b^*} = -K\partial_y\bar{b} \; . \tag{2.8}$$

Note that Eq. (2.2) (with $\kappa = 0$) ensures that the total parameterised eddy flux is directed along mean isopycnals using Eq. (2.8). The so-called eddy diffusivity K has to be specified; it accounts for the advective effects of turbulent lateral mixing by meso-scale eddies. The choice of K strongly affects the meridional and zonal transports of mass and tracers, in particular in the SO (England and Rahmstorf, 1998), and is therefore of crucial importance in order to quantify the role of the SO in the climate system. Typically constant values of $\mathrm{O}(1000m^2/s)$ are chosen in ocean climate models. However, it was demonstrated that K shows strong horizontal and vertical variations, and, in addition, that K should really be a tensor (Ferreira et al., 2005; Eden, 2006). Using a fixed eddy diffusivity K in non-eddy-permitting ocean models, as e.g. in Le Quéré et al. (2007); Lovenduski et al. (2007), the eddy-driven MOC may not respond realistically to changes in surface forcing.

A new flow-interactive meso-scale eddy closure for a scalar eddy diffusivity K was recently developed and evaluated by Eden and Greatbatch (2008). The simple closure for the horizontal eddy buoyancy fluxes in the ocean is given by adopting the downgradient

parameterisation (2.8) and assuming

$$K = LU \ , \tag{2.9}$$

where L denotes a characteristic eddy length scale and U denotes a characteristic eddy velocity. U is related to the mean eddy kinetic energy $\overline{E} = \frac{\overline{(u^*)^2+(v^*)^2}}{2}$ (EKE) via $U = \sqrt{\overline{E}}$. This standard mixing length assumption for the eddy diffusivity K of the Gent and McWilliams (1990) parameterisation is motivated by Green (1970) who first proposed the application of a mixing length approach for the eddy effect in geostrophic turbulence. The eddy length scale L is determined as the minimum of the local first baroclinic Rossby radius $L_r = \int_{-h}^{0}(\partial_z \bar{b})^{1/2} dz/(|f|\pi)$ and the Rhines scale $L_{Rhi} = \sqrt{U/\beta}$, that is, $L = min(L_r, L_{Rhi})$. The closure also includes a prognostic equation for the EKE that is integrated as an additional model variable of the non-eddy-resolving model. Terms of production, radiation and dissipation of EKE are parameterised based on variables of the non-eddy-resolving model. More precisely, the EKE budget is given by

$$\partial_t \overline{E} + \overline{v}\ \partial_y \overline{E} + \overline{w}\ \partial_z \overline{E} = \overline{S} + \overline{b^* w^*} - \epsilon - \nabla \cdot \mathbf{M} \ , \tag{2.10}$$

where $\overline{S} = -(\overline{v^* u^*}\partial_y \overline{u} + \overline{w^* u^*}\partial_z \overline{u} + \overline{v^* v^*}\partial_y \overline{v} + \overline{w^* v^*}\partial_z \overline{v})$ describes the energy exchange between mean kinetic energy and EKE, $\overline{b^* w^*}$ denotes the energy transfer between eddy potential energy and EKE (related to baroclinic instability), and the dissipation of EKE is denoted by ϵ. The term $\mathbf{M}$, $\nabla \cdot \mathbf{M} = \partial_y \overline{v^* E} + \partial_z \overline{w^* E} + \partial_y \overline{v^* p^*} + \partial_z \overline{w^* p^*}$, contains the effect of advection of EKE by the fluctuating flow and correlations between pressure and velocity fluctuations.

Eden and Greatbatch (2008) propose simple parameterisations for the terms on the right hand side of Eq. (2.10): by assuming $\kappa = 0$ and the downgradient parameterisation (2.8), it follows $\overline{b^* w^*} = K(\partial_y \bar{b})^2/\partial_z \bar{b}$. In analogy to homogeneous three-dimensional turbulence, Eden and Greatbatch (2008) use $\epsilon = c\overline{E}^{3/2} L^{-1}$, where c denotes a dimensionless constant typically of order one, $c = O(1)$. The flux $\mathbf{M}$ is interpreted as radiation of EKE and parameterised as isotropic horizontal diffusion of EKE, that is, $\nabla \cdot \mathbf{M} = -\partial_y(K \partial_y \overline{E})$. For further details we refer to Eden and Greatbatch (2008). Collecting the parameterisations, the EKE budget for the ocean interior ($\kappa = 0$) becomes

$$\partial_t \overline{E} + \overline{v}\ \partial_y \overline{E} + \overline{w}\ \partial_z \overline{E} = \overline{S} + K(\partial_y \bar{b})^2/\partial_z \bar{b} - c\overline{E}^{3/2} L^{-1} + \partial_y(K \partial_y \overline{E}) \ . \tag{2.11}$$

This equation can be prognostically integrated in a coarse resolution model which gives the diffusivity $K = \sqrt{\overline{E}}L$. However, neglecting the diffusive and advective terms and the energy production term $\overline{S}$, and assuming $\partial_t \overline{E} = 0$, we obtain the following simplified expression for the eddy diffusivity K:

$$K = cL^2\sigma \ , \tag{2.12}$$

where the inverse time scale $\sigma = |\partial_y \bar{b}|/N = |f\partial_z \overline{u}|/N$ is related to the vertical shear of the mean flow and is identical to the Eady growth rate. L is given by $L = min(L_r, L_{Rhi})$, with $L_{Rhi} = \sigma/\beta$. In this limit, the closure becomes similar to the parameterisation given by Visbeck et al. (1997), except that the definition of the length scale L differs and Visbeck et al. (1997) use σ averaged over the main thermocline. A comparison between the closures of Visbeck et al. (1997) and Eden and Greatbatch (2008) has been done in Eden et al. (2009a).

In section 2.5.3 we will assess this flow-interactive and spatially varying eddy closure, as given by Eq. (2.12), by using an idealised and eddy-permitting ocean model: first, we will directly compare the eddy diffusivity of the model itself (obtained by directly solving Eq. (2.8) using the model data) with the eddy diffusivity (2.12), that is, we will compare their spatial structures and sensitivities on wind stress; second, we will consider the effects on the MOC of both, the closure (2.12) and a constant eddy diffusivity as assumed in a standard Gent and McWilliams (1990) closure.

2.3.3 Diagnostic model

Marshall and Radko (2003) proposed a simple diagnostic model for the upper limb (above topography) of the MOC of the SO based on zonal mean residual-mean theory. We give a short presentation of the diagnostic model since we will use it in order to interpret our numerical model results. Note that Olbers and Visbeck (2005) proposed a similar but prognostic model of the MOC of the SO. However, in both models the balance between Ekman transport and meso-scale eddies plays a fundamental role in setting the stratification and overturning circulation.

Marshall and Radko (2003) divide the ocean into an upper mixed layer and an ocean interior underneath. The mixed layer is assumed to have a constant depth h_m, a vertically homogeneous mean buoyancy field $\bar{b}_m(y)$ and vanishing vertical sub-grid buoyancy flux at the base of the mixed layer, that is $B(z = -h_m) = 0$. Integrating Eq. (2.4) over the depth

of the mixed layer gives [2]

$$\psi_{res}|_{z=-h_m} = \frac{B|_{z=0} - \int_{-h_m}^{0} \partial_y(\overline{v^* b^*})\, dz}{\partial_y \overline{b}_m} \equiv \frac{\tilde{B}}{\partial_y \overline{b}_m} \ , \tag{2.13}$$

which states that information about ψ_{res} can be obtained by inspection of the surface buoyancy distribution ($\partial_y \overline{b}_m$), the surface air-sea buoyancy flux ($B|_{z=0}$) and the mixed layer lateral (diapycnal) eddy buoyancy fluxes ($\int_{-h_m}^{0} \partial_y(\overline{v^* b^*})$). In other words, the residual-mean overturning is given by the watermass conversion rate $\tilde{B}$ in steady state (Walin, 1982) divided by the meridional gradient of the zonal mean surface buoyancy distribution. Note that in the SO $\partial_y \overline{b}_m > 0$ holds. The relative importance of the two terms $B|_{z=0}$ and $\partial_y(\overline{v^* b^*})$ to the watermass conversion rate $\tilde{B}$ is currently not clear (Marshall and Radko, 2003). For surface water to move equatorward $\tilde{B} > 0$ has to hold, corresponding to local buoyancy gain by the mixed layer. If the mixed-layer buoyancy gradient is constant the strength and sense of the residual circulation are directly proportional to $\tilde{B}$.

The ocean interior is assumed to be adiabatic, that is, eddies transport and mix only along isopycnals, $\kappa = 0$, and diapycnal mixing by small-scale turbulence is neglected, $q_b = 0$. Hence, all mixing and watermass formation processes take place in the mixed layer. From Eq. (2.4) it follows

$$J(\psi_{res}, \overline{b}) = 0 \ , \tag{2.14}$$

which states that mean isopycnals and streamlines of the residual circulation coincide in the interior. These curves can be found as follows: applying Eq. (2.8) in Eq. (2.6) we find

$$\psi^*|_{interior} = Ks \ , \tag{2.15}$$

where $s \equiv dy/dz|_{b=const} = -\partial_y \overline{b}/\partial_z \overline{b}$ represents the slopes of the mean isopycnals. Using Eq. (2.7) we obtain the following equation for the slopes (above topography)

$$s = \frac{\tau_0}{fK} + \frac{\psi_{res}}{K} \ . \tag{2.16}$$

For given τ_0, K, $\overline{b}_m$ and buoyancy forcing $\tilde{B}$ this equation can be integrated along characteristics (see Marshall and Radko (2003); Olbers and Visbeck (2005)) since ψ_{res} can be evaluated at the base of the mixed layer via Eq. (2.13) and it is constant along character-

[2] $\psi_{res} = 0$ at the surface, because $\overline{w} = w^* = 0$ holds there.

istics due to Eq. (2.14). The values of buoyancy $\overline{b}$ and ψ_{res} on the characteristics are then determined by $\overline{b}_m$ and $\psi_{res}|_{z=-h_m}$, that is, in the mixed layer. It is the interplay of Ekman transport, meso-scale eddies and surface conditions that determine the upper limb (above topography) of the MOC of the SO. In particular, the dependence of the thermocline on wind stress is determined by Eq. (2.16).

In this simple diagnostic model a prescribed surface buoyancy distribution is mapped down from the base of the mixed layer into the interior for a given pattern of wind and buoyancy forcing and under the assumption of adiabatic interior dynamics. Sense and strength of the (residual) overturning circulation are determined by surface conditions at the same time. The effect of eddies also plays an essential role, but their impact remains problematic since K still has to be specified, that is, K has to be adequately parameterised. Different parameterisations can fundamentally alter the functional dependencies of all quantities, as demonstrated below.

In the following study we consult the interior part of this diagnostic model, that is Eq. (2.16), in order to discuss our numerical model results; we rewrite Eq. (2.16) as

$$\psi_{res}|_{interior} = -\frac{\tau_0}{f} + Ks \ . \tag{2.17}$$

Eq. (2.17) states that the mutual compensation of wind-driven Ekman transport and subsequent eddy circulation, given by the product of eddy diffusivity K and isopycnal slopes s, essentially constitutes the interior overturning circulation. The buoyancy forcing is implicitly present, first of all in s.

Furthermore, in section 2.5.4 we will demonstrate the crucial dependence of Eq. (2.17) on the eddy diffusivity K by determining K in different ways and comparing the resulting interior overturning circulations with numerical model results. In other words, we will assess under which conditions Eq. (2.17) represents an adequate conceptual understanding of the upper limb of the MOC of the SO regarding our idealised numerical model setup.

2.4 Numerical model and experiments

2.4.1 Idealised numerical ACC model

To assess the response of the meso-scale eddy field to different strengths of the zonal wind stress and its effect on the MOC of the SO we consider eddy-permitting simulations. In this study we use the idealised ACC configuration of CPFLAME *(http://www.ifm-*

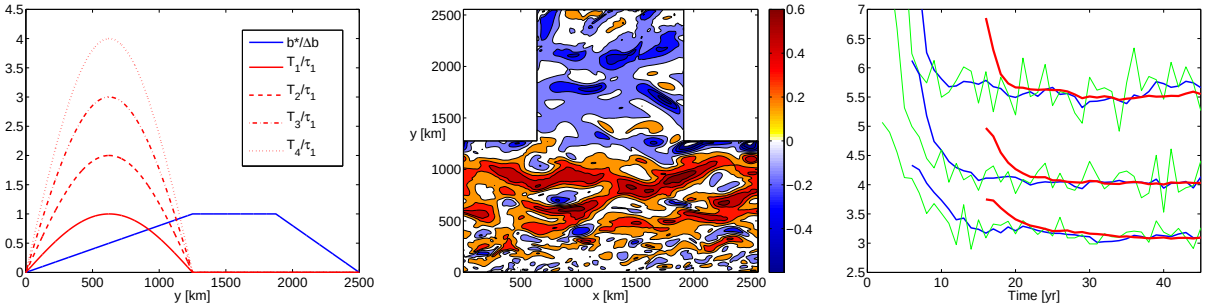

Figure 2.2: Left: target buoyancy $b^*/\Delta b$ for the surface restoring boundary condition and different wind forcings T_i/τ_1 imposed in the idealised ACC model. Middle: zonal velocity at the surface from the idealised ACC model for $\tau_1 = 0.5 \times 10^{-4} m^2 s^{-2}$ (contour interval is $0.15 ms^{-1}$). Right: maxima of the residual streamfunction ψ_{res} [Sv] at $200m$ depth in the ACC part for a 1-year-mean (green), 5-year-mean (blue), and a 15-year mean (thick red) for increasing wind stresses $\tau_2 = 1 \times 10^{-4} m^2 s^{-2}$, $\tau_3 = 1.5 \times 10^{-4} m^2 s^{-2}$, and $\tau_5 = 2.5 \times 10^{-4} m^2 s^{-2}$.

geomar.de/∼cpflame), an eddy-permitting primitive equation model consisting of a zonally reentrant channel (the "ACC part") which is connected to a northern ocean basin enclosed by land (the "Atlantic part"). The equations are formulated in Cartesian coordinates and the beta-plane approximation is used. The domain of the idealised ACC model extends over $L = 2500km$ in zonal and meridional direction with $\Delta R_1 = 5km$ horizontal resolution and 20 vertical levels with $50m$ thickness. We simulate only buoyancy in the model, which might be thought as proportional to temperature. The circulation in the model is driven by a sinusoidal eastward wind stress T_i over the ACC part, i.e.

$$T_i = \tau_i \sin(2\pi y/L) \qquad \text{for} \quad y < L/2 \tag{2.18}$$

$$T_i = 0 \qquad \text{else} , \tag{2.19}$$

and a surface restoring boundary condition for buoyancy b with a restoring time scale of 30 days and target buoyancy b^* as given in Figure 2.2 (left). A list of numerical constants used in the model runs is given in Table 2.1. The boundary conditions on the northern and southern edges of the domain are simply given by no-flux conditions. Hence, the watermass distribution is solely determined by the surface boundary conditions.

We impose a flat bottom and a land mass distribution as indicated in Figure 2.2 (middle) where the zonal velocity at the surface for $\tau_1 = 0.5 \times 10^{-4} m^2 s^{-2}$ is shown. In the ACC part the zonal flow is predominantly eastward with a strong jet slightly northward of the wind

Buoyancy change across ACC	Δb	$30 \times 10^{-3} m\ s^{-2}$
Restoring time scale	T_b	$30\ days$
Coriolis parameter	f_0	$-6 \times 10^{-5} s^{-1}$
Planetary vorticity gradient	β	$2 \times 10^{-11} m^{-1} s^{-1}$
Density of water	ρ_0	$1024\ kg\ m^{-3}$
Vertical viscosity	A_v	$10^{-3} m^2 s^{-1}$
Vertical diffusivity	K_v	$10^{-4} m^2 s^{-1}$
Biharmonic viscosity	A_{hbi}	$1.56 \times 10^{10} m^4 s^{-1}$
Bottom friction parameter	r	$10^{-5} s^{-1}$

Table 2.1: Numerical constants used in the idealised numerical model in the standard configuration.

stress maximum. The eddying structure of the jet is clearly visible. In the zonal mean, both EKE and eastward flow (not shown) in the ACC part of the model have a maximum at the surface slightly northward of the wind stress maximum (at around $800km$) and monotonically decrease north- and southward and with depth. Note, however, that the zonal flow extends over the whole water depth.

We also performed a series of additional experiments with conditions closer to the real ACC, i.e. a deeper basin ($5000\,m$ depth) and/or a topographic sill in the ACC part. However, the results concerning the MOC of the SO intermediate waters and the meso-scale eddy field are qualitatively similar to the more idealised flat bottom and $1000\,m$ deep basin[3]. In each case, the meso-scale eddy field in the whole water column remains essential in shaping and closing the MOC. However, in order to keep the discussion as clear as possible we focus on the simplest setting in this paper.

Figure 2.3 shows the residual (ψ_{res}), eddy (ψ^*) and Eulerian MOC ($\overline{\psi}$) of the idealised ACC model for $\tau_1 = 0.5 \times 10^{-4} m^2 s^{-2}$. As expected, the Eulerian streamfunction $\overline{\psi}$ in the ACC part is essentially given by the Ekman transport, that is $\overline{\psi} \approx -\tau/f$ (see (2.7)). The maxima of $\overline{\psi}$ are slightly shifted northward with respect to the wind stress maximum (they are located at $y \approx 800km$ instead of $y \approx 700km$ for $-\tau/f$) and are around 10% larger than for $-\tau/f$ at $150m$ depth (this also holds when using larger wind stresses, see Figure 2.5 below). The eddy driven streamfunction ψ^* is large in the ACC part and of opposite sign (and direction) of $\overline{\psi}$ but much smaller and of fluctuating sign in the Atlantic part of the domain. Differences between the eddy streamfunction ψ^* calculated from (2.2) and Ks (see

[3] These additional model runs were done with a coarser horizontal resolution of $20km$. However, as documented in section 2.5.2, the MOC and the meso-scale eddy field of our model qualitatively show the same behaviour also at $20km$ horizontal resolution.

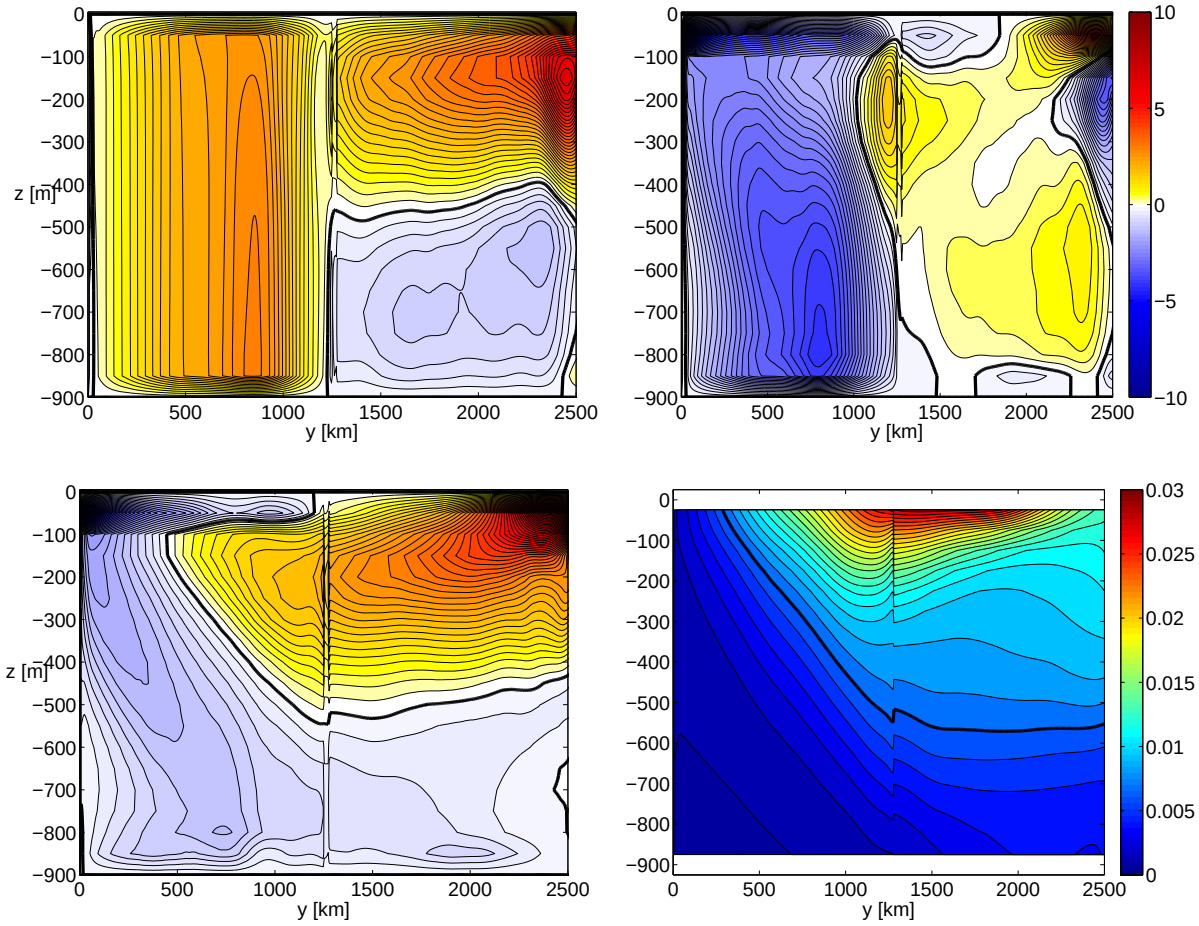

Figure 2.3: Zonal and time mean (upper left) Eulerian ($\overline{\psi}$), (upper right) eddy (ψ^*) and (lower left) residual streamfunction (ψ_{res}) from the idealised ACC model for $\tau_1 = 0.5 \times 10^{-4} m^2 s^{-2}$. Contour interval is 0.2 Sv in each case and zero lines are thick. Also shown is the zonal and time mean buoyancy distribution with a contour interval of $0.001 m/s^2$ and a thick $0.007 m/s^2$ line.

(2.15)) are very small (also when using larger wind stresses). The large Ekman pumping on the northern flank of the ACC is indeed almost balanced by eddy driven upwelling such that the sum of both, the residual streamfunction ψ_{res}, is consistent with the common view of the MOC of the SO and its role in the global large-scale meridional overturning: deep watermasses formed in the northern convective regions of the Atlantic part upwell across the ACC part, connecting both regions, and then return as subducted intermediate or mode water in order to close the circulation. There is even an indication of a reversed cell related to bottom water. The residual flow in the interior is nearly oriented along isopycnals as can be seen by comparison with the mean buoyancy distribution also shown

in Figure 2.3. The residual streamlines intersect the isopycnals mainly in the convective region at the northern end of the domain, and in the surface waters of the ACC part, where watermass transformation takes place. In the ACC part the isopycnal slopes are largest at the southern boundary and then decrease towards the northern end of the ACC part. Note that the peaks and recirculation cells in the center of the domain are due to standing eddy contributions related to the sharp edge in the land mass distribution[4].

Of course, this idealised eddy-permitting model can not be considered as a perfect representation of reality. However, we believe that the model setup includes the essential dynamical ingredients to describe the circulation of the SO and the global MOC. In particular, $\Delta R_1 = 5km$ horizontal resolution appears adequate in order to resolve meso-scale eddy-like features: the Rossby radius in our model is smallest near the southern boundary with values of about $2km$ but increases rapidly towards the north, with about $20km$ in the middle of the ACC part. Assuming that meso-scale eddies form on a scale about three times the Rossby radius, our model represents the generation of meso-scale eddy-like features well over wide ranges of the model domain. That is, we expect that our model simulates well the impact of the eddy field on the response of the residual MOC of the SO to changing winds in our idealised setting, although we cannot completely rule out possible changes by further refinements of the computational grid. Further, we consider the small northern basin, which is allowing the effective formation of a model NADW to close the circulation, as a sufficient addition to the SO to study the MOC of the SO in our idealised context without prescribing additional vertical boundary conditions at the northern end of the SO. We note, that the strength of the northern sinking and thus the global MOC depends on the northern as well as the southern buoyancy gradient and also on the wind stress. Since our main objective is on the sensitivity of SO to changes in wind stress, the following discussions and figures focus on the ACC part and on the impact of wind stress for the rest of this study.

2.4.2 Experiments

In order to mimic the response of the MOC of the SO to wind changes, we discuss several experiments with different, but in each case fixed strengths of wind stress, while the surface buoyancy restoring stays the same. The wind stress amplitude τ is increased in steps of $0.5 \times 10^{-4} m^2 s^{-2}$ from $\tau_0 = 0 m^2 s^{-2}$ up to $\tau_6 = 3 \times 10^{-4} m^2 s^{-2}$ (as indicated in Fig. 2.2 for

[4] Moreover we note, that for large wind stresses irregularities of the residual MOC appear at depth. These features can be related to rotational eddy fluxes which we aim to discuss in a further study.

the first four wind stresses (left)). The model needs some time to equilibrate. The time scale depends on the amplitude of the Ekman pumping but already after a few decades a steady state is reached in all experiments (see Fig. 2.2 (right)). In the following, we consider each quantity in a zonal and time mean for the years $30 - 45$. The results are presented in section 2.5.1.

In order to consider more complex and realistic model setups it may be necessary to use coarser resolutions. We document the effects of such coarsening in section 2.5.2. We use horizontal resolutions $\Delta R_2 = 10km$ and $\Delta R_3 = 20km$ respectively, to obtain two additional eddy-permitting model setups. For both cases we perform the same series of experiments as for ΔR_1, except that we increase the wind stress amplitude in case of ΔR_2 in steps of $1 \times 10^{-4} m^2 s^{-2}$. The biharmonic viscosity A_{hbi} is $A_{hbi} = 1.25 \times 10^{11} m^4 s^{-1}$ in case of ΔR_2 and $A_{hbi} = 1 \times 10^{12} m^4 s^{-1}$ in case of ΔR_3.

In section 2.5.3 we assess the effects of parameterising the meso-scale eddy field, necessary in climate models, on the simulated circulation. Therefore we implemented the Gent and McWilliams (1990) parameterisation, given by Eq. (2.8) for $\overline{v^* b^*}$ and similar for $\overline{u^* b^*}$, in our numerical model at resolution ΔR_3, specifying the eddy diffusivity K in two different ways, with five different parameter choices in each case. On the one hand, we specified K to be constant with $K_{1000} = 1000 m^2/s$, $K_{2000} = 2000 m^2/s$, $K_{3000} = 3000 m^2/s$, $K_{4000} = 4000 m^2/s$, and $K_{5000} = 5000 m^2/s$. On the other hand, in order to include spatial variations of the eddy diffusivity K, we implemented the flow-interactive meso-scale eddy closure by Eden and Greatbatch (2008), given by Eq. (2.12), using five different values for the dimensionless constant c: $c_1 = 1$, $c_2 = 2$, $c_3 = 3$, $c_4 = 4$, and $c_5 = 5$. The corresponding eddy diffusivities are denoted by $K_{EG1}, ..., K_{EG5}$. In order to implement the Gent and McWilliams (1990) parameterisation in our numerical model we used the residual-mean formalism according to Ferreira and Marshall (2006), that is, the eddy forcing in the momentum equation is represented as a vertical viscosity as first discussed by Greatbatch and Lamb (1990). We simply added a term $\partial_z (K f^2 / N^2 \partial_z \mathbf{u})$ to the momentum budget in the model, where $N = (\partial_z \bar{b})^{1/2}$ denotes the stability frequency. In regions where N goes to zero we have replaced f^2/N^2 with $\min(f^2/N^2, 0.01)$. Note that the additional vertical friction acts in the model very similar to the standard approach by adding an additional advection (bolus) velocity in the buoyancy budget. For each of our ten different choices for K we performed the same series of experiments as for the eddying models. We also included harmonic viscosity A_h in certain parameterised model versions, in order to completely suppress eddy activity (which tend to be present for strong Ekman pumping

and small eddy diffusivity): for the cases K_{1000} and K_{EG1} we included harmonic viscosity of $A_h = 15000m^2s^{-1}$ for all wind stresses, except for $\tau_6 = 3 \times 10^{-4}m^2s^{-2}$ where we used $A_h = 25000m^2s^{-1}$ in case of K_{1000}. Furthermore, in the case K_{2000} we included $A_h = 5000m^2s^{-1}$ for τ_0 up to τ_3 and $A_h = 15000m^2s^{-1}$ for higher wind stresses, while in case K_{3000} we included $A_h = 5000m^2s^{-1}$ for τ_3 and $A_h = 15000m^2s^{-1}$ for higher wind stresses. Finally, in case K_{4000} we included $A_h = 15000m^2s^{-1}$ for τ_5 and τ_6. Note that the actual MOC is insensitive to this model parameter in the parameterised models. However, we tried to use lowest possible values of A_h in all experiments.

We further focus our discussion on the nearly adiabatic interior dynamics of the ACC part. This part of the idealised numerical model is bounded by a surface, a bottom and a southern coastal boundary layer. In all of these regions mixing is dominating and watermass transformations take place. With increasing wind stress the surface boundary layer base increases from $-100m$ to $-150m$ and the bottom boundary layer surface increases from $-800m$ to $-750m$. The limits of the southern coastal boundary layer and a recirculation region are located around $100km$ and $1000km$ respectively. In the following we will focus on the interior region delimited by these bounds.

2.5 Results

2.5.1 Eddy compensation effect

Figure 2.4 shows the residual streamfunction (2.1) in the SO of the eddy-permitting idealised numerical model for three different wind stress amplitudes $\tau_1 = 0.5 \times 10^{-4}m^2s^{-2}$, $\tau_2 = 1 \times 10^{-4}m^2s^{-2}$ and $\tau_3 = 1.5 \times 10^{-4}m^2s^{-2}$. With increasing wind stress the residual circulation is strengthened and the depth of the positive residual circulation cell is increased. That is, magnitude and depth of the residual MOC are correlated. Both components, the wind-driven ($\overline{\psi}$, not shown) and the eddy-driven MOC (ψ^*, not shown), are significantly increasing with increasing wind stress such that the essential structure of the residual MOC remains the same: the large Ekman pumping on the northern flank of the ACC part is almost balanced by eddy driven upwelling such that a large-scale meridional residual overturning connects the upwelling regions of the ACC part with the convective regions of the Atlantic part. The Eulerian streamfunction $\overline{\psi}$ in the interior ACC part (not shown) is increasing nearly linearly in accordance to our expectation, that is $\overline{\psi}$ is essentially given by the Ekman transport, $\overline{\psi} \approx -\tau/f$ (differences between the Ekman transport $-\tau/f$ and $\overline{\psi}$ are due Reynolds-stresses which increase the maxima of the Eulerian streamfunction $\overline{\psi}$).

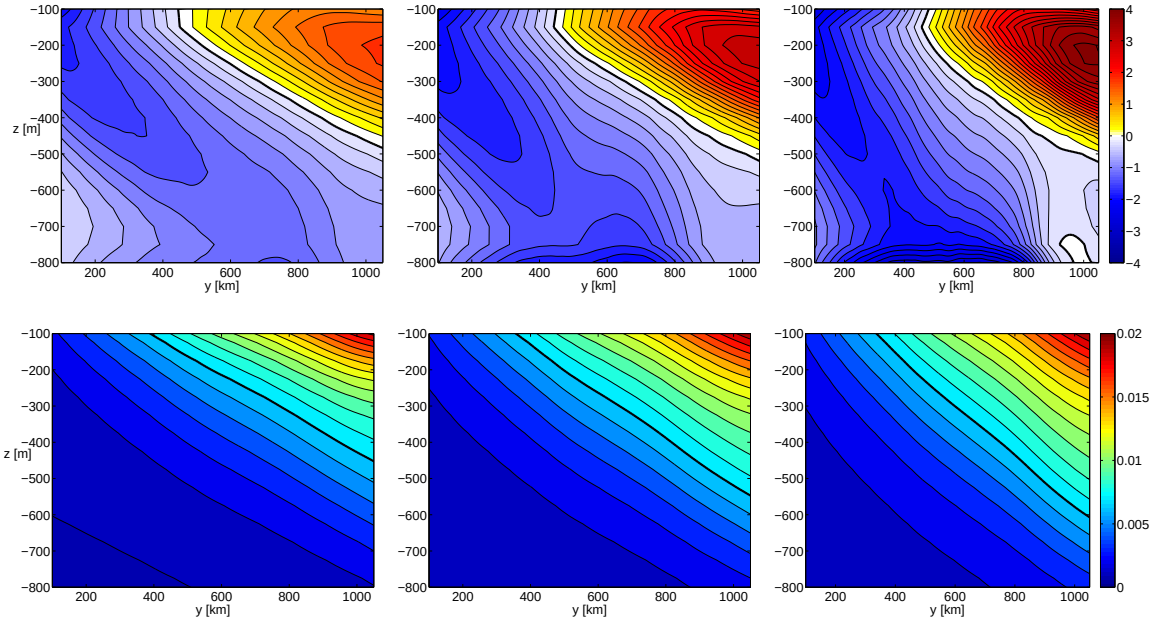

Figure 2.4: Zonal and time mean (upper) residual streamfunctions (ψ_{res}) and (lower) buoyancy distributions ($\overline{b}$) from the eddy-permitting idealised ACC model for wind stress amplitudes (from left to right) $\tau_1 = 0.5 \times 10^{-4} m^2 s^{-2}$, $\tau_2 = 1 \times 10^{-4} m^2 s^{-2}$ and $\tau_3 = 1.5 \times 10^{-4} m^2 s^{-2}$. The contour intervals are (upper) $0.2Sv$ and (lower) $0.001\ m/s^2$. Thick lines are (upper) zero lines and (lower) $0.007\ m/s^2$ lines.

We emphasise that the response of the eddy driven circulation is essential in shaping the response of the residual overturning circulation to changing wind stress: the eddies reduce the SO Ekman overturning and establish the connection to the Atlantic part, that is, the global overturning. The general behaviour (i.e. for any wind stress) of the eddy-driven MOC ψ^* to oppose the Eulerian MOC $\overline{\psi}$ in the SO (see again the representative Figure 2.3) is expressed in more precise terms by the following condition:

($ec1$): $\max(\psi_{res})(\tau) < \max(\overline{\psi})(\tau)$ for all wind stresses $\tau > 0$ in the SO.

Figure 2.5 shows the maximal transport values of the residual streamfunction, $\max(\psi_{res})(\tau)$, and the maximal transport values of the Eulerian streamfunction, $\max(\overline{\psi})(\tau)$, in the SO (left, thick and thin solid red lines). Note that $\max(\overline{\psi})(\tau)$ increases with a slightly larger slope than $\max(-\tau/f)$ (thin black line) due to the impact of Reynolds stresses. Additionally to ($ec1$) we find that the relation between $\max(\psi_{res})$ and $\max(\overline{\psi})$ can be characterised by a second condition:

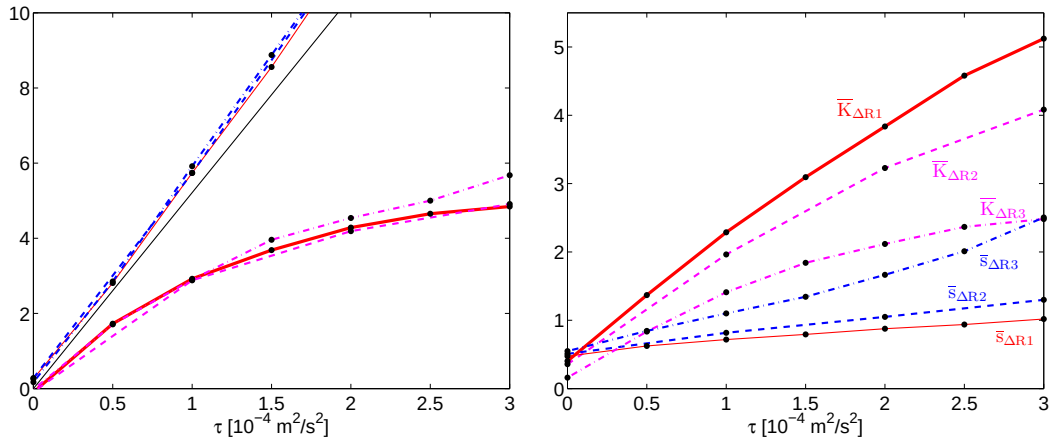

Figure 2.5: Left: maximal transport values [Sv] of the residual streamfunction ψ_{res}, the Eulerian streamfunction $\overline{\psi}$ and $-\tau/f$ at $-150m$ depth between the southern boundary and $y|_{\psi^*=0}$ (around $y = 1100km$) for the eddy-permitting ACC model configuration with different horizontal resolutions. Thick red: ψ_{res} for ΔR_1, magenta dashed: ψ_{res} for ΔR_2, magenta dash-dot: ψ_{res} for ΔR_3, thin red: $\overline{\psi}$ for ΔR_1, blue dashed: $\overline{\psi}$ for ΔR_2, blue dash-dot: $\overline{\psi}$ for ΔR_3, thin black: $-\tau/f$. Black dots denote data points. Right: the corresponding mean eddy diffusivities $\overline{K}$ $[10^3 m^2/s]$ and isopycnal slopes $\overline{s}$ $[-10^{-3}]$. Averages are taken at $-200m$ depth and between $110km$ and $910km$.

$(ec2)$: $\partial_\tau(\max(\psi_{res})) < \partial_\tau(\max(\overline{\psi}))$ for all wind stresses $\tau > 0$ in the SO.

That is, not only the absolute value but also the increase of $\max(\psi_{res})$ is generally smaller than that of $\max(\overline{\psi})$. Moreover, focusing on $\max(\psi_{res})$ in relation to itself, a tendency (i.e. a gradual and not an abrupt transition) towards a state of relatively little change in transport of the residual MOC for higher wind stresses becomes obvious: in contrast to the linear increase of the Eulerian MOC $\overline{\psi}$, the increase of the residual MOC ψ_{res} reduces with increasing wind stress. This is expressed in more precise terms by the following condition:

$(ec3)$: $\partial_\tau^2(\max(\psi_{res})) \leq 0$ for all wind stresses $\tau > 0$ in the SO.

In other words, the ability of the eddy field to compensate the increase of the Eulerian streamfunction $\overline{\psi}$ rises with increasing wind stress and may lead to mutual neutralisation and therewith to a complete wind stress insensitivity of the residual MOC. However we note, that for our wind stress range a state of total compensation between Euler and eddy

MOC is not reached but the residual MOC is still significantly increasing for increasing wind stress.

The behaviour of the residual MOC regarding different wind stresses, characterised by the conditions ($ec1$), ($ec2$) and ($ec3$), is what we call the *eddy compensation effect*[5]. Condition ($ec1$), namely a leading order balance between eddy-driven and wind-driven circulation, was described first by Johnson and Bryden (1989) in its extreme form of vanishing residual circulation (see also Karsten et al. (2002)). Conditions ($ec2$) and ($ec3$), that actually describe the response of the residual MOC to changing winds, are less well considered. Hallberg and Gnanadesikan (2006) qualitatively noted an asymmetry in the response of the residual MOC to whether the wind stress was increased or decreased by 20% relative to a reference state. Here we give a more quantitative description of the eddy compensation effect for a broad range of realistic wind stresses.

In the adiabatic interior, the eddy-driven circulation is given by equation (2.15), $\psi^* = Ks$. That is, ψ^* and therewith the eddy compensation effect is determined by two factors: the eddy diffusivity K and the isopycnal slopes s, which we will consider now. Figure 2.6 (upper row) shows the eddy diffusivity K, diagnosed from the flux-gradient relationship (2.8), for three different wind stress amplitudes $\tau_1 = 0.5 \times 10^{-4} m^2 s^{-2}$, $\tau_2 = 1 \times 10^{-4} m^2 s^{-2}$ and $\tau_3 = 1.5 \times 10^{-4} m^2 s^{-2}$ in the SO of our eddy-permitting idealised numerical model. K is generally positive but shows clearly strong spatial variations. Meridionally, K is smallest at the southern boundary[6]. It then increases northward; in the latitude band between the wind stress maximum and maximal EKE, K reaches its maxima. Towards the northern boundary K decreases again. In contrast to the EKE, K is maximal near the bottom boundary layer and decreases upwards (and again increases strongly in the mixed layer, not shown). With increasing wind stress, K also increases while the spatial structure of K is maintained. The maxima of K increase from about $3500 m^2/s$ to about $7500 m^2/s$.

Figure 2.5 also shows K averaged meridionally at $-200m$, $\overline{K}$ (right, thick solid red line).

[5] We note, that the term *eddy compensation* has to be distinguished from the term *eddy saturation*. While the former is related to the residual MOC as described in this study following Hallberg and Gnanadesikan (2006), the latter is related to the circumpolar ACC transport as used in Hallberg and Gnanadesikan (2001). *Eddy saturation* refers to a dynamical state of the SO in which increases in wind stress do not alter the zonal transport as suggested by Marshall et al. (1993); Straub (1993). Nevertheless, also the residual MOC may reach a state of complete wind stress insensitivity. However, note that while saturation regarding different wind stresses may apply to zonal transport, it does not necessarily follow that the residual MOC is in a state of complete wind stress insensitivity and vice versa.

[6] Note that this stands in strong contrast to the structure of the isopycnal slopes s (which are largest at the southern boundary, see below) and therefore rejects a parameterisation of K proportional to s as proposed by Marshall and Radko (2003).

$\overline{K}$ increases with increasing wind stress and, similar to the residual MOC, the increase of $\overline{K}$ diminishes monotonically with increasing wind stress for the wind stress range under consideration, that is $\partial_\tau^2 \overline{K} \leq 0$. The maxima of K (not shown) show qualitatively the same behaviour. We further note, that also the EKE averaged at $200m$ depth ($\overline{EKE}$, not shown) has a similar dependency on τ as $\overline{K}$. Both, $\partial_\tau \overline{K}(\tau)$ and $\partial_\tau \overline{EKE}(\tau)$, are monotonically decreasing functions, similar[7] to the residual MOC. Therefore, the dependency of K (and EKE) on τ has to be clearly distinguished from the corresponding response of the eddy streamfunction ψ^* (measured via $\max(\overline{\psi}) - \max(\psi_{res})$), which shows monotonically *increasing* increases, $\partial_\tau^2 \left[\max(\overline{\psi}) - \max(\psi_{res})\right] \approx -\partial_\tau^2 \max(\psi_{res}) \geq 0$ (as demonstrated in Figure 2.5, left). It becomes clear that the sensitivity of the isopycnal slopes s has to be considered too in order to understand ψ^* (see (2.15)), as we will see now.

Figure 2.4 also shows the zonal and time mean buoyancy distribution for three different wind stress amplitudes $\tau_1 = 0.5 \times 10^{-4} m^2 s^{-2}$, $\tau_2 = 1 \times 10^{-4} m^2 s^{-2}$ and $\tau_3 = 1.5 \times 10^{-4} m^2 s^{-2}$ in the SO of our eddy-permitting idealised numerical model. The slopes of the isopycnals are (absolutely) increasing with increasing wind stress throughout the whole interior of the SO while the spatial structure remains. Figure 2.5 also shows the isopycnal slopes s averaged meridionally at $-200m$, $\overline{s}$ (right, thin solid red line). The increase of the isopycnal slopes $\overline{s}$ for different wind stresses is nearly constant, $\partial_\tau \overline{s} \approx const.$ There is no tendency towards a fixation of the isopycnal slopes $\overline{s}$ for the wind stress range under consideration. This behaviour is consistent with equation $\psi^* = Ks$, as given by (2.15), and our previous results for ψ^* and K, by interpreting $\max(\overline{\psi}) - \max(\psi_{res})$ via[8] $\overline{K}\overline{s}$: while $\partial_\tau \overline{K}$ is monotonically decreasing and $\partial_\tau \overline{s} \approx const.$, the absolute value of $\partial_\tau(\overline{K}\overline{s})$ (not shown) is monotonically increasing[9]. Hence, both K and s are relevant in order to obtain the correct sensitivity of the eddy streamfunction ψ^* towards changing wind stress.

Nevertheless, although the response towards changing wind stress of the eddy streamfunction ψ^* is qualitatively different from the corresponding response of K, it is the eddy diffusivity K that quantitatively dominates the sensitivity of $\psi^* \approx Ks$ towards increasing

[7] Note that also an eddy length scale $L_{ed} \equiv \overline{K}(\overline{EKE})^{-0.5}$ (not shown), defined via the mixing length approach (2.9), shows the same behaviour: L_{ed} is increasing with increasing wind stress from around $10km$ (for τ_0) to around $20km$ (for τ_6) with monotonically diminishing increases, that is $\partial_\tau^2 L_{ed} \leq 0$ for $\tau > 0$.

[8] Note that the equivalence between the values of Figure 2.5 (left) and Figure 2.5 (right) is quantitatively not exact since the values of the former are taken at fixed points while the values of the latter denote averages. Nevertheless, $\overline{K}\overline{s}$ shows qualitatively the same behaviour as $\max(\overline{\psi}) - \max(\psi_{res})$.

[9] Mathematically we have: $\partial_\tau \overline{K} > 0$, $\partial_\tau^2 \overline{K} \leq 0$, $\overline{s} < 0$ and $\partial_\tau \overline{s} \approx const < 0$, hence $\partial_\tau^2(\overline{K}\overline{s}) \approx 2(\partial_\tau \overline{K})(\partial_\tau \overline{s}) + \overline{s}\partial_\tau^2 \overline{K}$. It follows that $\overline{s}\partial_\tau^2 \overline{K} \leq |2(\partial_\tau \overline{K})(\partial_\tau \overline{s})|$ has to hold, which is not trivially the case.

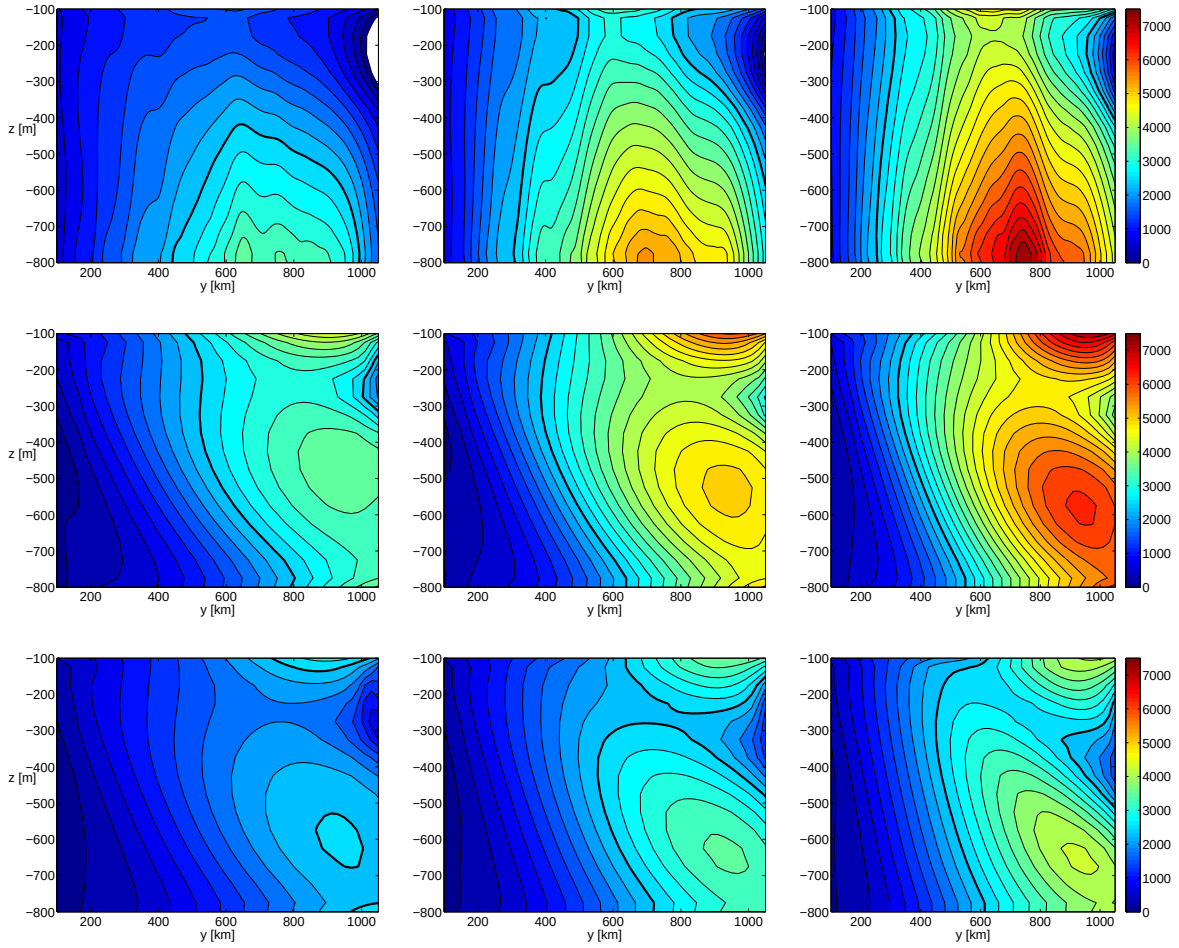

Figure 2.6: Zonal and time mean eddy diffusivity K $[m^2/s]$ for three different wind stress amplitudes (from left to right) $\tau_1 = 0.5 \times 10^{-4} m^2 s^{-2}$, $\tau_2 = 1 \times 10^{-4} m^2 s^{-2}$ and $\tau_3 = 1.5 \times 10^{-4} m^2 s^{-2}$ from (upper) the eddy-permitting idealised model and the parameterised idealised ACC model using the closure of Eden and Greatbatch (2008), given by (2.12), with (middle) $c = 4$ and (lower) $c = 2$. The contour intervals are $250 m^2/s$ and the $2500 m^2/s$ line is thick.

wind stress in our experiments. The relative increases of the eddy diffusivity $\overline{K}$ are much larger than that of the isopycnal slopes $\overline{s}$ for the wind stress range under consideration. Therefore, presuming small linear increases of the isopycnal slopes, the eddy diffusivity K seems to be the important quantity in order to understand the sensitivity of ψ^* and ψ_{res} to changing winds.

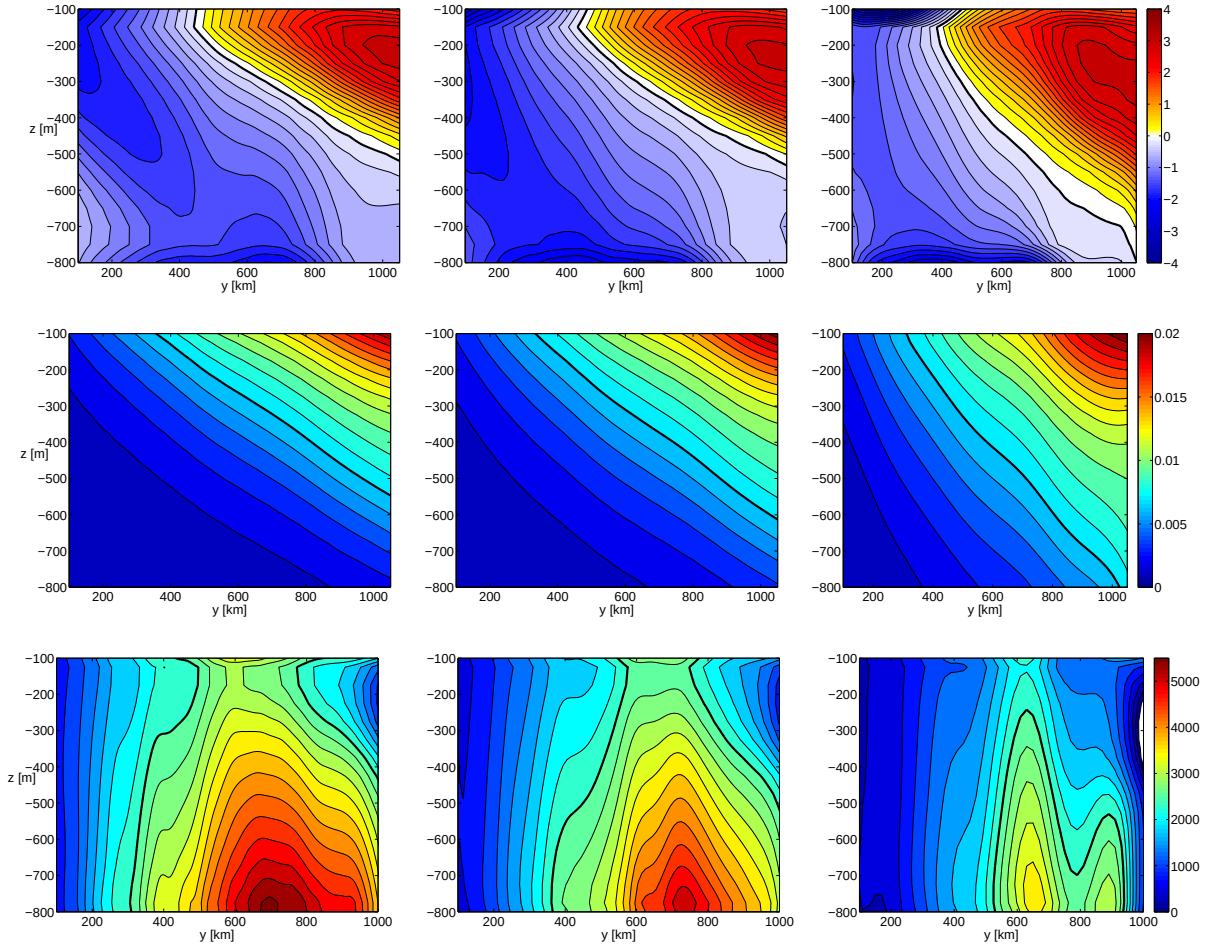

Figure 2.7: Zonal and time mean (upper) residual streamfunctions (ψ_{res}), (middle) buoyancy distributions ($\bar{b}$) and (lower) eddy diffusivities (K) from the idealised ACC model for $\tau_2 = 1 \times 10^{-4} m^2 s^{-2}$ with different horizontal resolutions (from left to right): $\Delta R_1 = 5km$, $\Delta R_2 = 10km$, $\Delta R_1 = 20km$. The contour intervals are (upper) $0.2Sv$, (middle) $0.001\ m/s^2$ and (lower) $250 m^2/s$. Thick lines are (upper) zero lines, (middle) $0.007\ m/s^2$ lines and (lower) $2500 m^2/s$ lines.

2.5.2 Impact of horizontal resolution

Ocean model setups may have to represent larger spatial domains than our idealised model configuration. In such a case it may be necessary to use coarser resolutions. This section documents the effects of such coarsening. Figure 2.7 shows ψ_{res} in the SO of the eddying models with $\tau_2 = 1 \times 10^{-4} m^2 s^{-2}$ for $\Delta R_1 = 5km$, $\Delta R_2 = 10km$, and $\Delta R_3 = 20km$. The circulation pattern of the residual MOC, with a negative circulation cell spanning the southern and deep regions of the ACC part and a positive circulation cell extending

over the upper, northern part, is qualitatively the same in all three cases. The spatial structure of both components, the wind-driven ($\overline{\psi} \approx -\tau/f$, not shown) and t he eddy-driven MOC ($\psi^* \approx Ks$, not shown), is also almost unchanged. However, with decreasing horizontal resolution the depth of the positive residual circulation cell is increased. The positions of $\max(\psi_{res})$ and $\psi_{res} = 0$ move towards the south (for $\tau \leq \tau_3$) and also the position of $\max(\overline{\psi})$ moves southward, closer to the position of $\max(-\tau/f)$, reflecting the decreasing impact of Reynolds stresses. In contrast, the strength of the residual circulation is almost unchanged for coarser horizontal resolutions. This almost complete insensitivity of the magnitude of the residual MOC to our range of coarser horizontal resolutions is also documented in Figure 2.5. Both, $\max(\psi_{res})$ (left, magenta lines) and $\max(\overline{\psi})$ (left, blue lines) for ΔR_2 (dashed) and ΔR_3 (dash-dot), are very close to $\max(\psi_{res})$ and $\max(\overline{\psi})$ for ΔR_1. In case of ΔR_2 the differences to $\max(\psi_{res})$ for ΔR_1 are under 2%, while in case of ΔR_3 the differences increase to about $6-8\%$ for high wind stresses ($\tau \geq \tau_3$). Consequently, also the respective effective compensation due to the eddy field is nearly the same for all three cases. Only for higher wind stresses the case ΔR_3 tends to slightly overestimate the residual MOC due to both, a slight underestimation of the Eulerian MOC $\overline{\psi}$ and a slightly stronger underestimation of the eddy-driven MOC ψ^* (in the region of the positive residual MOC).

The almost complete insensitivity of $\overline{\psi}$ to coarser horizontal resolutions may be expected, since the Eulerian MOC is largely given by $\overline{\psi} \approx -\tau/f$, that is by resolution-independent prescribed quantities. In contrast, the representation of the meso-scale eddy field strongly depends on the resolution of the meso-scale in the model: the EKE (not shown) decreases with decreasing horizontal resolution[10]. Similarly, the eddy diffusivity K decreases with decreasing horizontal resolution, as shown in Figure 2.7 for $\tau_2 = 1 \times 10^{-4} m^2 s^{-2}$. The maxima of K are decreasing from about $5500 m^2/s$ to about $5000 m^2/s$ for ΔR_2 and to about $3500 m^2/s$ for ΔR_3. Also visible is that the maxima of K are shifted slightly northward with decreasing horizontal resolution and split into two local maxima for ΔR_3. However, the spatial pattern of K remains the same for all horizontal resolutions under consideration. Figure 2.5 also shows $\overline{K}$ at $-200m$ for the cases ΔR_2 and ΔR_3 (right, dashed and dash-dotted magenta lines). Like $\overline{EKE}$[11] (not shown), $\overline{K}$ decreases with decreasing horizontal

[10] Note that this behaviour is superimposed by the effect of an increased biharmonic viscosity A_{hbi}, necessary for numerical reasons in case of lower horizontal resolutions, which acts to damp EKE.

[11] Also the eddy length scale $L_{ed} \equiv \overline{K}(\overline{EKE})^{-0.5}$ (not shown) shows an analogue behaviour: L_{ed} decreases with decreasing horizontal resolution, while still $\partial_\tau^2 L_{ed} \leq 0$ holds and in case ΔR_3 the eddy length scale L_{ed} appears to be nearly in a state of complete wind stress insensitivity for high wind stresses ($\tau > \tau_5$).

resolution, while still $\partial_\tau^2 \overline{K} \leq 0$ holds. In case ΔR_3 the eddy diffusivity $\overline{K}$ even appears to be nearly in a state of complete wind stress insensitivity, tending towards a maximum of $\overline{K}$ between $2500m^2/s$ and $3000m^2/s$ for high wind stresses ($\tau > \tau_5$).

In contrast to $\overline{K}$ (and $\overline{EKE}$), the effective compensation due to the eddy field appears to be nearly insensitive to the coarsening of the horizontal resolution[12]. Again, this difference may be understood by interpreting $\max(\overline{\psi}) - \max(\psi_{res})$ via $\overline{K}\overline{s}$ (see (2.15)), that is the corresponding behaviour of the isopycnal slopes. Figure 2.7 also shows the zonal and time mean buoyancy distribution for $\tau_2 = 1 \times 10^{-4} m^2 s^{-2}$. The slopes of the isopycnals are (absolutely) increasing with decreasing horizontal resolution throughout the whole interior of the SO, while the spatial structure remains the same. Figure 2.5 also shows $\overline{s}$ at $-200m$ for the cases ΔR_2 and ΔR_3 (right, dashed and dash-dotted blue lines). The isopycnal slopes $\overline{s}$ increase with decreasing horizontal resolution such that the product $\overline{K}\overline{s}$ remains nearly constant. In case ΔR_3 the isopycnal slopes $\overline{s}$ even behave qualitatively different to the cases ΔR_1 and ΔR_2: for ΔR_3 the isopycnal slopes s dominate the increase of the eddy streamfunction $\psi^* \approx Ks$ for higher wind stresses ($\tau > \tau_3$), as K is nearly in a state of complete wind stress insensitivity.

To conclude, the eddy compensation effect ((ec1)-(ec3)) is at work in all horizontal resolutions under consideration and quantitatively nearly insensitive to the coarsening of the horizontal resolution. However, the dependencies of the eddy diffusivity K (and EKE) and the isopycnal slopes s on wind stress do depend on horizontal resolution and have to be distinguished from the corresponding sensitivity of the eddy streamfunction ψ^*.

2.5.3 Effects of different eddy diffusivity parameterisations

It is common practise in climate models to use the Gent and McWilliams (1990) meso-scale eddy parameterisation (2.8) with a constant eddy diffusivity K. In order to assess the effect of parameterising the meso-scale eddy field on the MOC of the SO we implement the Gent and McWilliams (1990) parameterisation (2.8) in our numerical model with five different constant values for K: $K_{1000} = 1000m^2/s$, $K_{2000} = 2000m^2/s$, $K_{3000} = 3000m^2/s$, $K_{4000} = 4000m^2/s$, and $K_{5000} = 5000m^2/s$. However, since K shows strong spatial variations and is sensitive to wind stress changes as shown in section 2.5.1, we also implemented the flow-interactive meso-scale eddy closure developed by Eden and Greatbatch (2008), given

[12] Note that our model with lowest resolution is still an eddy-permitting configuration. Of course, in case the coarsening is proceeded until the meso-scale is unresolved, the eddy circulation ψ^* will tend to vanish and the residual MOC ψ_{res} will drastically change (ending up as the Eulerian MOC $\overline{\psi}$).

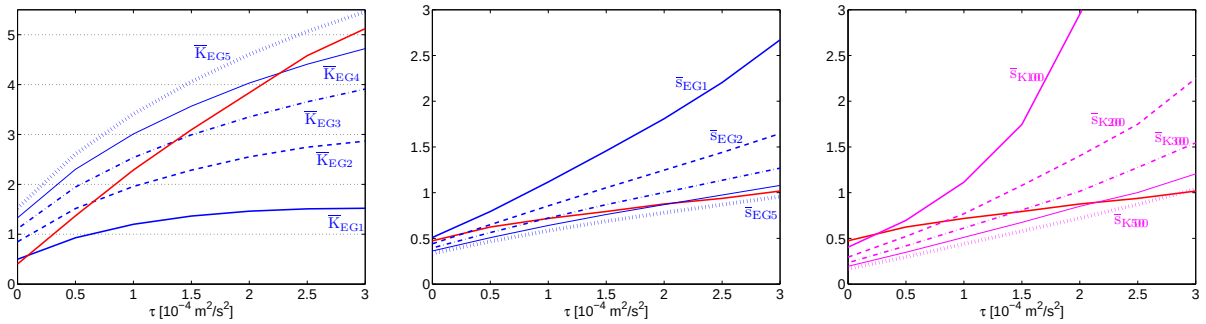

Figure 2.8: Mean (left) eddy diffusivities $\overline{K}$ $[10^3 m^2/s]$ and (middle, right) isopycnal slopes $\overline{s}$ $[-10^{-3}]$ for the different idealised ACC model configurations. Averages are taken at $-200m$ depth and between $110km$ and $910km$. Red: eddy-permitting reference case ΔR_1, blue thick: K_{EG1}, blue dashed: K_{EG2}, blue dash-dot: K_{EG3}, blue thin: K_{EG4}, blue dotted: K_{EG5}, black thick: K_{1000}, black dashed: K_{2000}, black dash-dot: K_{3000}, black thin: K_{4000}, black dotted: K_{5000}. Left black dotted lines denote the corresponding constant eddy diffusivities.

by (2.12), in order to demonstrate and offer a parameterisation which produces an eddy diffusivity closer to the K from the eddying model than a constant eddy diffusivity. We used five different values for the dimensionless constant c: $c_1 = 1$, $c_2 = 2$, $c_3 = 3$, $c_4 = 4$, and $c_5 = 5$. The corresponding eddy diffusivities are denoted by $K_{EG1}, ..., K_{EG5}$.

Figure 2.6 shows the eddy diffusivity K of the eddy-permitting model and the eddy diffusivities K_{EG4} and K_{EG2}, given by (2.12), for three different wind stress amplitudes $\tau_1 = 0.5 \times 10^{-4} m^2 s^{-2}$, $\tau_2 = 1 \times 10^{-4} m^2 s^{-2}$ and $\tau_4 = 1.5 \times 10^{-4} m^2 s^{-2}$. Both, K_{EG4} and K_{EG2}, capture the spatial variations qualitatively quite well: smallest values at the southern boundary with a tendency towards vertical homogeneity are obviously reproduced. In the region of large EKE close to the center of the SO maxima near the bottom boundary layer can be found, with decreasing values upwards and with a secondary maximum in the mixed layer. In contrast to K from the eddying model the maxima of K are slightly moved towards the northern boundary and to shallower depths (which becomes more pronounced for larger c and smaller wind stress); furthermore, the secondary maximum in K extends to deeper depths. The deep maxima of K are generally underestimated by K_{EG2}, while K_{EG2} changes from a slight overestimation for small wind stress ($\tau \leq \tau_1$) to an underestimation for large wind stress ($\tau \geq \tau_2$) regarding the upper maxima. K_{EG4} overestimates the upper maxima for $\tau \leq \tau_4$ and changes from a slight overestimation for small wind stress ($\tau \leq \tau_1$) to an underestimation for large wind stress ($\tau \geq \tau_2$) regarding the lower maxima. This is also documented in Figure 2.8 (left, blue lines) showing $K_{EG1}, ..., K_{EG5}$ averaged at

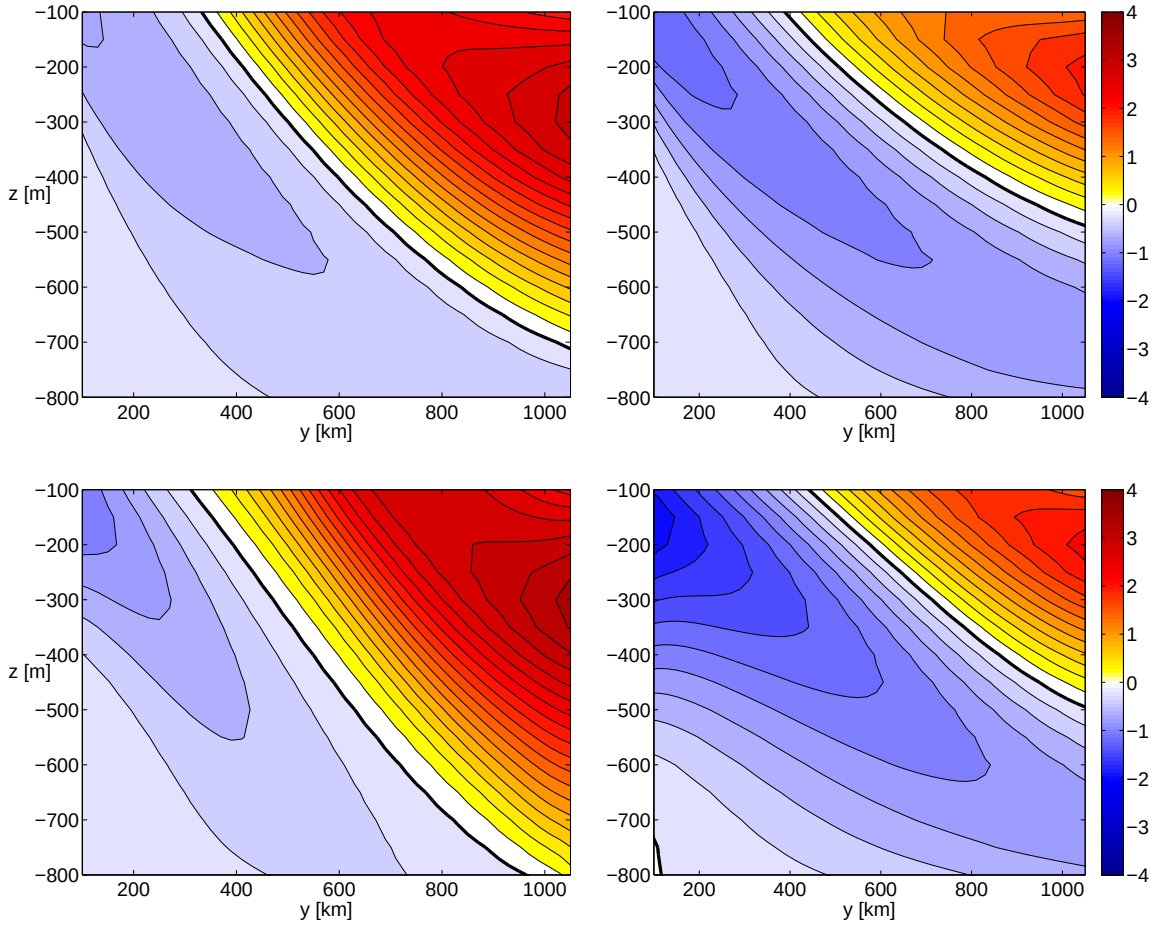

Figure 2.9: Zonal and time mean residual streamfunctions (ψ_{res}) from the idealised ACC model for $\tau_2 = 1 \times 10^{-4} m^2 s^{-2}$ and different model configurations: K_{EG1} (upper left), K_{EG3} (upper right), K_{1000} (lower left), K_{3000} (lower right). The contour intervals are $0.2Sv$ and zero lines are thick.

$-200m$. $\overline{K}_{EG1}, ..., \overline{K}_{EG5}$ capture the response of K in the eddying model towards changing wind stress qualitatively well: each $\overline{K}_{EG1}, ..., \overline{K}_{EG5}$ increases with increasing wind stress, that is $\partial_\tau \overline{K} > 0$, and further we find $\partial_\tau^2 \overline{K} \leq 0$ in each case. But the parameterisation (2.12) generally underestimates the quantitative sensitivity of K on wind stress (that is the magnitudes of $\partial_\tau \overline{K}$). For this reason $\overline{K}_{EG1}$, which is close to the $\overline{K}$ from the eddying model for small wind stress ($\tau < \tau_1$), is nearly insensitive to changes in wind stress for higher wind stress, while $\overline{K}$ from the eddying model is still significantly increasing. The relative increases of $\overline{K}_{EG1}, ..., \overline{K}_{EG5}$ (not shown) are nearly identical, as expected from (2.12). Therefore the eddy diffusivity parameterisation (2.12) in general, i.e. independent of the

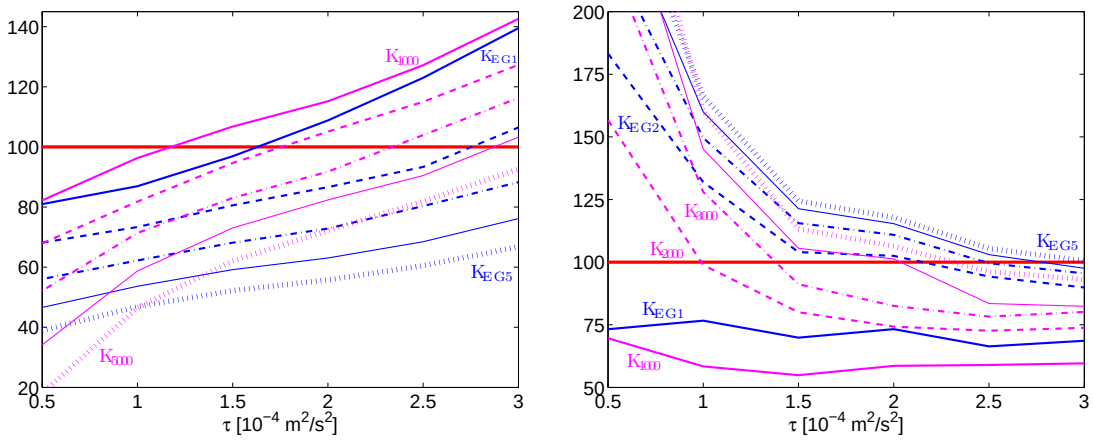

Figure 2.10: Percentages of the transport values of (left) the residual streamfunction ψ_{res} and (right) the eddy streamfunction $\psi^*_{para} \equiv Ks$ at $150m$ depth and $y = 970km$, from the parameterised idealised ACC model using (blue) the closure of Eden and Greatbatch (2008), given by (2.12), and (magenta) using constant eddy diffusivities. Values are taken relative to the eddy-permitting reference setup ΔR_1 (red line). Blue thick: K_{EG1}, blue dashed: K_{EG2}, blue dash-dot: K_{EG3}, blue thin: K_{EG4}, blue dotted: K_{EG5}, magenta thick: K_{1000}, magenta dashed: K_{2000}, magenta dash-dot: K_{3000}, magenta thin: K_{4000}, magenta dotted: K_{5000}.

choice of c, underestimates the sensitivity of K to wind stress. Hence, the parameterisation (2.12) represents well the spatial structure of K and its qualitative response to increasing wind stress which is, however, quantitatively underestimated.

Figure 2.9 shows the residual streamfunctions (ψ_{res}) for the cases K_{EG1}, K_{EG3}, K_{1000}, K_{3000} and fixed wind stress $\tau_2 = 1 \times 10^{-4} m^2 s^{-2}$ (the corresponding eddy-permitting result is given in Fig. 2.4). All parameterisations reproduce qualitatively well the positive overturning cell (yellow-red): narrow streamlines reach from the deep northern boundary to the southward surface. Quantitatively, the cases K_{EG1} and K_{1000} have appropriate magnitudes of the MOC but overestimate its depth, while the cases K_{EG3} and K_{3000} underestimate the magnitudes of the MOC and show appropriate depths of the positive overturning cell. Depth and magnitude of the residual MOC are anti-correlated with the constant K (or c in (2.12)): larger K (or c) reduce both, the magnitude and the depth, of the positive overturning cell; that is, we can anticipate that the isopycnal slopes s are decreased (shallower MOC), while the parameterised eddy compensation is absolutely increased (reduced magnitude of the MOC) for larger K (or c). Concerning the negative overturning cell (blue), which is not in the focus of this paper, we note that all parameterisations underestimate

the magnitudes of the MOC at depth as well as the slopes of the streamlines. That is, the ability of a parameterisation to reproduce the negative overturning cell has to be evaluated on its own. Moreover we note, that all parameterisations show a different boundary layer behaviour than the eddy-permitting model. This is related to the fact that we use adiabatic parameterisations which suppress meso-scale diapycnal mixing. Hence, from the outset diabatic effects are smaller in the parameterised model configurations than in the eddy-permitting model configuration.

In order to understand the sensitivity of the residual MOC of the parameterised models on wind stress, we consider the percentages of the residual MOC taken at a fixed (representative) position in the SO, relative to the values of the eddy-permitting setup (Figure 2.10 (left)). Note that ψ_{res} is increasing for all parameterisations. Further, condition (ec3), in this context $\partial_\tau^2 \psi_{res} \leq 0$, is also at work in all parameterised models. However, it is obvious in Figure 2.10 (left) that the response of the residual MOC towards increasing winds is overestimated by each parameterisation. In general, the parameterised model using the closure (2.12) shows a more appropriate response than using a constant K, which is, however, still far from perfect: on the one hand, large values of c in closure (2.12) produce the most adequate relative sensitivity of ψ_{res} to τ, but the most incorrect magnitudes of ψ_{res} due to the excessively large K. On the other hand, for smaller values of c the sensitivity of ψ_{res} to τ is similar to using K_{1000}, while the magnitude of ψ_{res} is over- (under-) estimated for larger (smaller) wind stress.

The parameterised models simulate the residual MOC only, which, however, can also be conceptually decomposed into two parts: the Eulerian MOC $\overline{\psi}_{para}$ and an eddy-driven MOC ψ^*_{para}. We define them here intrinsically via $\psi^*_{para} \equiv Ks$ and $\overline{\psi}_{para} \equiv \psi_{res} - \psi^*_{para}$, where all quantities refer to the parameterised model. The Eulerian MOC $\overline{\psi}_{para}$ (not shown) is again given by the Ekman transport, that is $\overline{\psi}_{para} \approx -\tau/f$, although all parameterised models underestimate the Eulerian MOC $\overline{\psi}$ of the reference case ΔR_1 by $5\% - 20\%$. On the other hand, all parameterised models tend to overestimate the response of the Eulerian MOC towards increasing wind stress.

Figure 2.10 (right) shows ψ^*_{para} for each parameterisation taken at a fixed (representative) position in the SO, relative to the values of the eddy-permitting setup ΔR_1. We find that with increasing values of c or K the eddy MOC ψ^*_{para} absolutely increases, which corresponds to the decrease of the residual MOC with increasing values of c or K (Figure 2.10 (left)). For all parameterisations, we find $\partial_\tau^2 |\psi^*_{para}| \geq 0$. However, the response of the eddy MOC ψ^*_{para} is generally underestimated, so that for smaller wind stresses ($\tau \leq \tau_2$) the

magnitudes of the eddy MOC of the reference case ΔR_1 tend to be overestimated (by over 200%), while for higher wind stresses ($\tau \geq \tau_5$) the magnitudes of the eddy MOC of the reference case ΔR_1 tend to be underestimated. The underestimation of the response of the eddy MOC towards increasing winds reduces with decreasing values of c or K: K_{EG1} and K_{1000} show nearly correct responses of the eddy MOC, but permanently underestimate the magnitudes of the eddy MOC by $25\% - 45\%$, with the constant eddy diffusivity case being worse.

The eddy MOC ψ^*_{para} is constituted by two factors, the eddy diffusivity K and the isopycnal slopes s. The averages of both at $-200m$ are shown in Figure 2.8 for each parameterisation. In lieu of the underestimation of the sensitivity of K to τ, the response of the isopycnal slopes towards increasing wind stress is overestimated. For both parameterisations, the intimate relation between eddy diffusivity and isopycnal slopes, as already discussed in section 2.5.2, is demonstrated again: the underestimated response of $\overline{K}$ corresponds an overestimated response of $\overline{s}$, such that $\partial_\tau |\overline{K}\overline{s}| \geq 0$. Hence, increasing the constant values of K or c, that is the eddy diffusivity, (absolutely) decreases the magnitude of the isopycnal slopes, that is $\partial_K |\overline{s}| < 0$ or $\partial_c |\overline{s}| < 0$, as it is obvious in Figure 2.8. And, similar to the eddy diffusivity, the closure (2.12) represents the response of the isopycnal slopes more adequately (smaller slopes) than the corresponding constant eddy diffusivity case: for a constant eddy diffusivity it is only the isopycnal slope which captures the response of the eddy MOC towards increasing winds. We also note that, in the case that a parameterisation captures the correct eddy diffusivity K at fixed point, the isopycnal slopes are nearly correct, but never exactly correct, since the eddy diffusivity values in the environment of the point are related to the isopycnal slopes. Therefore, also the eddy MOC $\psi^* = Ks$ is never exactly (but nearly) correct at a location of correct eddy diffusivity K.

2.5.4 Sensitivity of the diagnostic model

In order to demonstrate that our conceptual framework of the interior residual MOC of the SO above topography, given by the diagnostic model of Marshall and Radko (2003) (and Olbers and Visbeck (2005)) we presented in section 2.3.3, is appropriate as long as the correct eddy diffusivity is taken into account, we compare the application of Eq. (2.16) with our numerical model results. Figure 2.11 shows the residual streamfunction ψ_{res} in the SO for three different wind stress amplitudes $\tau_1 = 0.5 \times 10^{-4} m^2 s^{-2}$ (left), $\tau_2 = 1 \times 10^{-4} m^2 s^{-2}$ (right) and in between $\tau = 0.75 \times 10^{-4} m^2 s^{-2}$. On the one hand, ψ_{res} is given by the results

of the eddy-permitting numerical model for case ΔR_3 (upper). On the other hand, ψ_{res} is given by prescribing $\psi_{res}(z = -150m)$ via the results of the eddy-permitting numerical model (case ΔR_3) and applying equation (2.16) with K given by the eddy-permitting numerical model for case ΔR_3 (middle) and by $K = 1000m^2/s$ (lower).

The diagnostic model (2.16) in conjunction with the diagnosed eddy diffusivity K reproduces the extent of the positive and negative overturning cells and the slopes of the streamlines very well for each wind stress. In particular, the slight deepening of the zero line (thick) is captured almost perfectly. Small deviations from the eddy-permitting numerical model results represent diabatic effects not included in the adiabatic diagnostic model (2.16). Therefore, using the correct eddy diffusivity in the diagnostic model (2.16) it is able to reproduce the essential residual MOC of the SO and its sensitivity to changing winds.

In contrast, using $K = 1000m^2/s$ in the diagnostic model (2.16) the reproduction of the residual MOC of the SO and its response to changing winds is inadequate. The streamlines are much too steep. Therefore the positive overturning cell reaches much deeper and has a bigger extent than in the eddy-permitting numerical model results. Furthermore, the steepening and deepening of the streamlines due to increasing winds are overestimated. That is, the response to increasing winds of the diagnostic model (2.16) using $K = 1000m^2/s$ suggests that much deeper water upwells than in the case with the correct eddy diffusivity. We also note that in case of a constant eddy diffusivity, the diagnostic model (2.16) misrepresents the negative overturning cell: the negative overturning cell is shifted towards the north and does not reach the southern boundary anymore. This is due to the sign of the curvature of the streamlines of the diagnostic model (2.16) with $K = 1000m^2/s$ which is different for the streamlines of the eddy-permitting numerical model and the diagnostic model (2.16) with the correct eddy diffusivity.

2.6 Summary and conclusions

We have described the sensitivity of the residual MOC ψ_{res} in the SO and the corresponding eddy diffusivity K towards changing wind stress by using the results of an eddy-permitting idealised numerical ACC model (at $\Delta R_1 = 5km$ horizontal resolution). The residual circulation strengthens with increasing wind stress. The wind-driven component $\overline{\psi}$ is increasing nearly linearly according to $\overline{\psi} \approx -\tau/f$, whereas the (absolute) increase of the eddy-driven component $\psi^* \approx Ks$ amplifies with increasing wind stress, such that we could describe

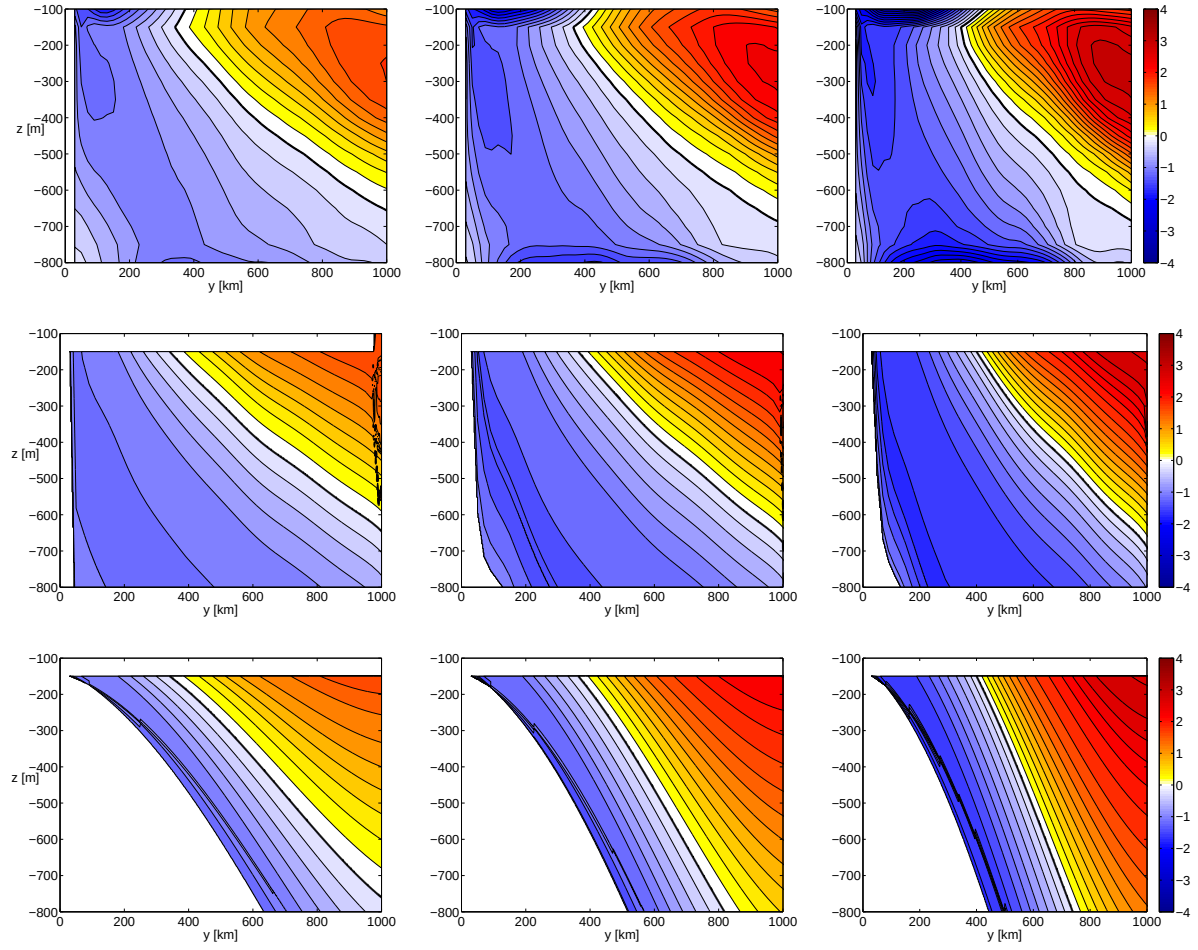

Figure 2.11: Zonal and time mean residual streamfunctions (ψ_{res}) from (upper) the eddy-permitting idealised ACC model for case ΔR_3 and from the application of equation (2.16) with (middle) an eddy diffusivity diagnosed from the eddy-permitting model and (lower) prescribing a fixed eddy diffusivity of $1000 m^2/s$. The wind stress amplitudes are (left) $\tau_1 = 0.5 \times 10^{-4} m^2 s^{-2}$, (right) $\tau_2 = 1 \times 10^{-4} m^2 s^{-2}$ and in between $\tau = 0.75 \times 10^{-4} m^2 s^{-2}$. The contour intervals are $0.2 Sv$ and zero lines are thick.

the sensitivity of the residual MOC on wind stress by three aspects, termed as *eddy compensation effect*: namely, the general behaviour of ψ^* to oppose $\overline{\psi}$ such that ($ec1$) the absolute value and ($ec2$) the increase of the residual MOC are generally smaller compared to $\overline{\psi}$ and ($ec3$) the increase of the residual MOC ψ_{res} reduces with amplifying winds (i.e. $\partial_\tau^2 \max(\psi_{res}) \leq 0$). Furthermore, magnitude and depth of the residual MOC are correlated. ($ec3$) opens the possibility, that the residual MOC may become completely insensitive to wind stress. However we note, that for our wind stress range a state of total compensation

between Euler and eddy MOC is not reached but the residual MOC is still significantly increasing for increasing wind stress. We thus have not demonstrated with our model experiments a complete insensitivity of the MOC towards winds.

The corresponding eddy diffusivity K is characterised by a manifold spatial structure and by a strong sensitivity towards changing winds: K (and EKE) increases with increasing wind stress and, similar to the residual MOC, the increase of K (and EKE) averaged at $200m$ depth diminishes monotonically with increasing wind stress, i.e. $\partial_\tau^2 \overline{K} \leq 0$, for the wind stress range under consideration. Consequently, the sensitivity of the eddy diffusivity K (and EKE) to wind stress has to be distinguished from the corresponding response of the eddy streamfunction $\psi^* \approx Ks$. It turns out that a nearly constant increase of the isopycnal slopes s, though quantitatively much smaller than the increase of the eddy diffusivity K, is relevant in order to capture the correct sensitivity to wind stress of the product Ks.

We also document the effects of coarsening the horizontal resolution by considering our eddy-permitting model setup at $\Delta R_2 = 10km$ and $\Delta R_3 = 20km$ horizontal resolution. While the depth of the positive residual circulation cell increases with decreasing horizontal resolution, the strength of the residual MOC ψ_{res}, the Eulerian MOC $\overline{\psi}$ and hence the effective eddy compensation are almost unchanged for our coarser horizontal resolutions. Hence, the eddy compensation effect ((ec1)-(ec3)) is at work in all horizontal resolutions under consideration. While the almost complete insensitivity of $\overline{\psi}$ to coarser horizontal resolutions may be expected (from $\overline{\psi} \approx -\tau/f$), the almost unchanged eddy compensation is not so obvious, since the representation of the meso-scale eddy field in general strongly depends on the resolution of the meso-scale in the model; it is due to the intimate relation between eddy diffusivity K and isopycnal slopes s which both strongly depend on horizontal resolution. We indeed find that the eddy diffusivity K (and EKE) decreases with decreasing horizontal resolution, while the slopes of the isopycnals are (absolutely) increasing with decreasing horizontal resolution, such that the product $\overline{K}\overline{s}$ remains nearly constant. Consequently, the dependency of K (and EKE) on horizontal resolution has to be distinguished from the corresponding (in)sensitivity of the eddy compensation. It follows that eddy-permitting ocean models with relatively low resolution may simulate an adequate eddy compensation effect, but misrepresent the changes in eddy diffusivity K, the isopycnal slopes s, ACC transport and isopycnal diffusivities (relevant e.g. for CO_2).

In climate models it is necessary to parameterise the meso-scale eddy field, that is the eddy diffusivity K, due to too coarse resolution. In order to assess the effect of param-

eterising the meso-scale eddy field on the residual MOC of the SO, we implemented the Gent and McWilliams (1990) parameterisation, as given by Eq. (2.8) and widely used in state-of-the-art climate models, in our numerical model. On the one hand, we specified the eddy diffusivity K by different constant values; on the other hand, we implemented the flow-interactive meso-scale eddy closure by Eden and Greatbatch (2008), given by Eq. (2.12). We find that the parameterisation (2.12) represents well the spatial structure of K and its qualitative response to increasing wind stress which is, however, quantitatively underestimated. The latter effect becomes even more clear for constant eddy diffusivity parameterisations, since they lack any sensitivity by definition. Consequently, for both, the closure (2.12) and any constant K, there will be wind stress ranges of over- or underestimation of the eddy diffusivity K. In the parameterised models, eddy diffusivity and isopycnal slopes are intimately linked as well: the underestimated response of $\overline{K}$ corresponds an overestimated response of $\overline{s}$, such that $\partial_\tau|\overline{K}\overline{s}| \geq 0$, with the closure (2.12) being more adequate than a constant K parameterisation. However, for all parameterisations the response of the eddy MOC of the eddying model (ΔR_1) tends to be underestimated by the parameterised eddy MOC $\psi^*_{para} \equiv Ks$.

The residual MOC behaves accordingly in the parameterised models. We find that all parameterisations reproduce the positive overturning cell for a fixed wind stress qualitatively well. However, the response of the residual MOC towards increasing winds is overestimated by each parameterisation, with the closure (2.12) being slightly more adequate than a constant K. Consequently, each parameterisation will always under- or overestimate the residual MOC in a certain wind stress range. Hence, our results clearly demonstrate that the sensitivity of the residual MOC towards changing winds crucially depends on the corresponding sensitivity of the eddy diffusivity K. It is indispensable to incorporate the correct sensitivity of the eddy diffusivity in order to reproduce the sensitivity of the residual MOC towards changing winds.

In order to demonstrate that our conceptual framework of the interior residual MOC of the SO above topography, given by the diagnostic model of Marshall and Radko (2003) (and Olbers and Visbeck (2005)), is appropriate as long as the correct eddy diffusivity is taken into account, we compared the application of equation (2.16) with our numerical model results for case ΔR_3. We found that using the eddy diffusivity (and $\psi_{res}(z = -150m)$) of the numerical model in the diagnostic model (2.16), it is able to reproduce the essential residual MOC of the SO and its sensitivity to wind stress. In contrast, using $K = 1000m^2/s$ in the diagnostic model (2.16) the reproduction of the residual MOC of the SO and its

response to changing winds is inadequate: steepening and deepening of the streamlines due to increasing winds are overestimated.

We have demonstrated that the correct behaviour of the eddy diffusivity in coarse-resolution climate models is essential for a correct simulation of changes in the SO and thus a thorough assessment of climate change. In particular, the simulation of the residual MOC and the related CO_2 content in the SO and its response to changing winds, as e.g. done in Le Quéré et al. (2007) and Lovenduski et al. (2008), depends crucially on the subgrid-scale parameterisation. Up-to-date eddy diffusivity parameterisations, as demonstrated in this study, lead to under- or overestimations of the residual MOC and the related CO_2 content in the SO for different wind stresses. Our results strengthen the necessity of further improvements of meso-scale eddy diffusivity parameterisations.

Acknowledgements

This study was supported by the Deutsche Forschungsgemeinschaft within the SPP 1158. The authors wish to thank Richard Greatbatch for valuable comments and discussions and two anonymous reviewers for helpful criticism and suggestions.

3 Standing eddies in the meridional overturning circulation

This chapter is an earlier draft of the paper "Standing eddies in the meridional overturning circulation" accepted and in production by the Journal of Physical Oceanography.

Citation: Viebahn, J. and C. Eden, 2012: Standing eddies in the meridional overturning circulation, J. Phys. Oceanogr., doi: 10.1175/JPO-D-11-087.1. (c) American Meteorological Society. Reprinted with permission.

3.1 Abstract

The role of standing eddies for the meridional overturning circulation (MOC) is discussed. The time-mean isopycnal meridional streamfunction is decomposed into a time- and zonal-mean part, a standing eddy part and a transient eddy part. It turns out that the construction of an isopycnal MOC with an exactly vanishing standing eddy part has to be performed by zonal integration along depth-dependent horizontal isolines of time-mean density. In contrast, zonal integration along time-mean geostrophic streamlines generally only leads to an isopycnal MOC with a reduced standing eddy part.

Using the results of an idealised Southern Ocean model, it is also demonstrated that applying density contours or geostrophic streamlines of a certain depth ("contour-depth") at each depth, may represent an acceptable practical simplification ("orthogonal approximation"): On the one hand, the standing eddy part vanishes exactly only at the contour-depth (except using the ageostrophic surface layer and geostrophic streamlines), but on the other hand, for adequate contour-depths the overall standing eddy part is significantly reduced (but not vanishing).

Furthermore, it is found that the effect of changing the zonal integration path from latitude circles to curvilinear paths on the zonally averaged density is of the same order as changing from Eulerian to isopycnal averaging.

3.2 Introduction

The meridional overturning circulation (MOC) of the Southern Ocean (SO) appears to be an important part of the global overturning circulation system (Kuhlbrodt et al., 2007): On the one hand, the inter-basin connection featured by the SO is a necessary condition for a global circulation to be possible. On the other hand, the watermass transformations, driven by wind and buoyancy forcing in the SO, establish connections between deep and surface waters in the SO and hence close the global meridional circulation cells (Rintoul et al., 2001).

A compact description of the MOC of the SO is conventionally given by a zonal-mean meridional streamfunction. However, it is well known that different integration procedures lead to different pictures of the MOC, since they extract different physical aspects of the overall circulation. In order to construct a zonal-mean meridional streamfunction two decisions have to be made: *First*, a transport integration criterion has to be specified. *Second*, the zonal integration paths have to be specified, which determine the meridional transport velocity as the meridional cross-path component of the overall velocity field.

Latitude circles represent the simplest type of zonal integration path. The *Eulerian streamfunction* $\Lambda(y, z_a)$ is then the zonally integrated meridional transport of fluid across a given latitude y and below the constant height surface z_a. However, Döös and Webb (1994) demonstrated that the overturning pattern of the Eulerian streamfunction Λ gives rise to spurious diapycnal flow in the SO (the "Deacon cell") and hence fails to give an adequate picture of the MOC of the SO.

Changing the transport integration criterion 'below a constant height surface' to 'denser than a certain instantaneous density' leads to isopycnal averaging (McDougall and McIntosh, 2001; Nurser and Lee, 2004a). The *isopycnal streamfunction* $\psi_I(y, b_a)$ gives then the zonally integrated meridional transport of fluid denser than a given density b_a across a given latitude y. The isopycnal streamfunction ψ_I appears to capture the essential behaviour of the MOC of the SO, since the ocean is largely stable stratified and watermasses mainly remain in a fixed density class while travelling in the ocean interior (Webb and Suginohara, 2001).

In the SO, topographic features force the circumpolar flow (the Antarctic Circumpolar Current (ACC)) to carry out permanent meridional excursions on its circumpolar path. Therefore, it has been argued that calculating the transport across time-mean streamlines rather than latitude circles more effectively reveals the physical nature of the meridional overturning (Marshall et al., 1993; Treguier et al., 2007). For example, in the realistic high

resolution modelling study of Treguier et al. (2007) (see also Hallberg and Gnanadesikan (2006); Lee et al. (2007)) in the upper 500 m poleward surface flow shows up in the SO in case the zonal integration is performed along latitude circles, apparently against the wind-driven equatorward Ekman transport. Indeed, Treguier et al. (2007) show that in the meridional circulation averaged along contours of the barotropic streamfunction, the surface flow becomes equatorward in the SO. Hence, they suggest that in the zonal integration one has to follow time-mean streamlines such that the correlations resulting from the permanent meanders of the ACC ("standing eddies") vanish.

In addition, further reasons to minimise standing eddies in the MOC have been put forward: It was suggested that a standing-eddy-free framework could give more lucidity in the consideration of physical budgets (e.g. momentum, potential vorticity, tracer) (Marshall et al., 1993). Moreover, in non-eddy-permitting models (e.g. Marshall and Radko (2003) and Olbers and Visbeck (2005)) eddies have to be adequately parameterised (Viebahn and Eden, 2010). Of course, the corresponding approaches try to parameterise transient eddies and not a part of the time-mean circulation.

Various studies agree in using the term "time-mean streamlines", but they differ in the specification of the zonal integration paths. While Ivchenko et al. (1996) and Treguier et al. (2007) integrate along contours of the barotropic streamfunction, Marshall et al. (1993) use contours of the Montgomery streamfunction, Karsten and Marshall (2002) use surface geostrophic streamlines (using mean sea surface height) and Polton and Marshall (2007) integrate along Bernoulli potential contours. In every study a single set of horizontal paths (surface contours) is used for each depth, although Lee and Coward (2003) notice that there "are problems in using surface streamlines throughout the water columns since flows below the surface do not exactly follow the surface streamlines."

In this study, we want to clarify the idea of neutralising the effect of the permanent meanders of the ACC ("standing eddies") on the MOC of the SO by a redefinition of the zonal integration paths, in order to provide a consistent concept. In section 3.3 we describe an idealised model of the SO and our set of experiments, which we will use for illustrative purposes. After the presentation of the standard zonal-mean meridional streamfunctions, we introduce the isopycnal standing eddy streamfunction $\hat{\psi}_I^*$ in section 3.5.1. Finally, in section 3.5.2 we discuss both, different approaches to minimise $\hat{\psi}_I^*$ via different zonal integration paths and the corresponding effects on the overall MOC. Section 3.6 provides a summary and section 3.7 conclusions.

3.3 Idealised numerical SO model and experiments

In this study we use the idealised SO configuration of CPFLAME[1], an eddy-permitting primitive equation model consisting of a zonally reentrant channel, which is connected to a northern ocean basin enclosed by land (see e.g. Fig. 3.6 a)). The equations are formulated in Cartesian coordinates and the beta-plane approximation is used. The domain of the idealised SO model extends over $L = 2520$km in the zonal and meridional direction, with $\Delta R = 20$km horizontal resolution and 40 vertical levels with 50m thickness (1900m maximal water depth). We simulate only buoyancy in the model, which might be thought as proportional to temperature. On the one hand, the circulation in the model is driven by a sinusoidal eastward wind stress over the channel with a magnitude of $\tau = 1 \times 10^{-4} m^2 s^{-2}$. On the other hand, a surface restoring boundary condition for buoyancy b is applied. The corresponding target buoyancy increases northward over the channel, remains constant over the southern half of the northern ocean basin and decreases while approaching the northern end of the domain. Boundary conditions on the northern and southern edges of the domain are simply given by no-flux conditions. Hence, the watermass distribution is solely determined by the surface boundary conditions. Viebahn and Eden (2010) showed that our setup with $\Delta R = 20$km horizontal resolution captures a qualitatively adequately resolved meso-scale eddy field (compared to model results with higher horizontal resolution). Further details of our numerical model setup may be found in Viebahn and Eden (2010).

We consider two different experiments. In the first experiment, we impose a simple hill-like topographic feature in the channel: The top of the hill is located at $z = -950$m and $x = 0$ (and $x = 2520$km respectively). According to an exponential map the height of the hill decreases eastward (westward), such that at the longitudes of the northern ocean basin (from $x = 850$km to $x = 1690$km) the channel has a flat bottom. We refer to this setup as the *hill case*. The hill case is of primary interest in this study. In order to illustrate the impact of topography, we contrast the hill case by an experiment with a completely flat bottomed channel. This is the so-called *flat case*. In both cases, the model has been run for about 240 years in order to reach a statistically steady state. In the following, each time-mean is performed over the last ten years (that is, the years $231 - 240$).

[1] *http://www.ifm.zmaw.de/∼cpflame*

3.4 Eulerian streamfunction and mean buoyancy

A simple way to produce a zonal-mean meridional streamfunction is based upon Eulerian averaging along latitude circles, that is, integration over the zonal coordinate x is performed at constant depth z and constant latitude y. The Eulerian zonal-mean of the buoyancy field $b(x, y, z, t)$ is given by (Nurser and Lee, 2004a)

$$[b](y, z, t) = \frac{1}{L_x} \int_{west}^{east} b \, dx \ , \tag{3.1}$$

where $L_x(y, z)$ denotes the zonal length and squared brackets denote the zonal-mean. The Eulerian meridional streamfunction Λ is the zonally integrated southward transport of fluid across a given latitude and below the constant height surface z_a,

$$\Lambda(y, z_a, t) \equiv - \int \int_{(x,z):z \le z_a} v \, dx \, dz = - \int_{z \le z_a} L_x[v] \, dz \ . \tag{3.2}$$

In the following, we will also discuss the time-mean denoted by an overbar. Since the conditions of integration are not time-dependent, Eulerian zonal-mean and time-mean commute, that is,

$$\overline{[b]}(y, z) = \left[\overline{b}\right](y, z) = \frac{1}{L_x} \int_{west}^{east} \overline{b} \, dx \ . \tag{3.3}$$

The time-mean Eulerian streamfunction $\overline{\Lambda}$ is thus related to the time-mean meridional velocity $\overline{v}$,

$$\overline{\Lambda}(y, z_a) \ = \ - \int \int_{(x,z):z \le z_a} \overline{v} \, dx \, dz = - \int_{z \le z_a} L_x[\overline{v}] \, dz \ . \tag{3.4}$$

More precisely, it is only the Eulerian zonal-mean and time-mean meridional velocity $[\overline{v}]$ which determines the time-mean Eulerian streamfunction $\overline{\Lambda}$, so that all deviations of the zonal and temporal means are neglected in the calculation of $\overline{\Lambda}$. This is the essential difference between the Eulerian streamfunction $\overline{\Lambda}$ and the isopycnal streamfunction $\overline{\psi_I}$, which we discuss in section 3.5. In case of zonal integration along latitude circles, Λ and $\overline{\Lambda}$ in general are streamfunctions, since it holds[2] $\partial_z \Lambda = -L_x[v]$ and $\partial_y \Lambda = L_x[w]$.

[2] Zonal integration along latitude circles of the continuity equation ($\nabla \cdot \mathbf{v} = 0$) above topography in a zonally reentrant channel immediately gives $\partial_y(L_x[v]) + \partial_z(L_x[w]) = 0$. In case of topographic or continental barriers, given by $x_{\mathcal{B}}(y, z)$, the cross-barrier velocity vanishes due to the no-normal-flow

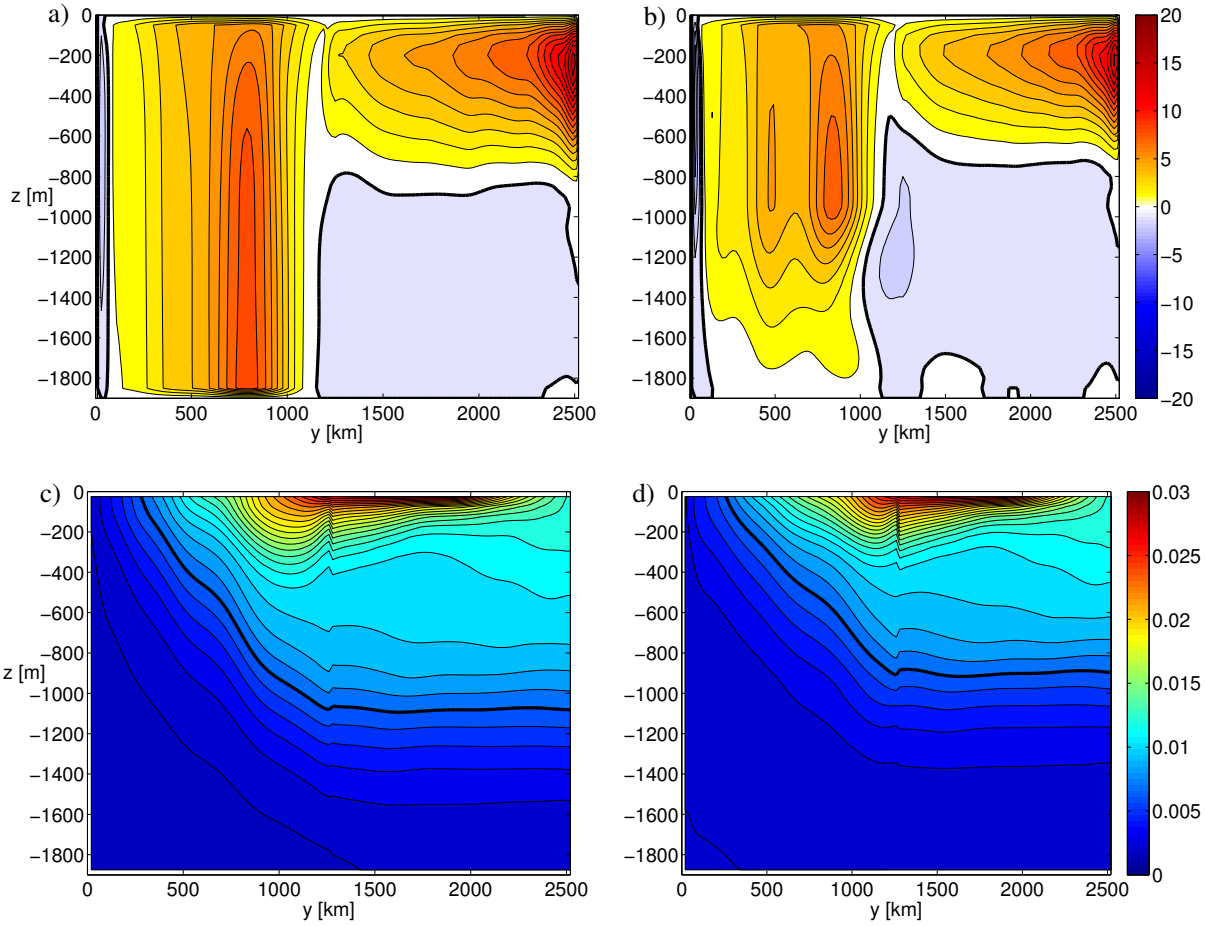

Figure 3.1: Top: Time-mean Eulerian meridional streamfunction ($\overline{\Lambda}$) with a contour interval of 1 Sv and thick zero lines for the flat (a) and the hill (b) case. Bottom: Eulerian zonal- and time-mean buoyancy distribution ($[\overline{b}]$) with a contour interval of $0.001 m/s^2$ and a thick $0.007 m/s^2$ line for the flat (c) and the hill (d) case.

Figure 3.1 shows the time-mean Eulerian streamfunction $\overline{\Lambda}$ for both the flat case and the hill case. In the flat case, the meridional time-mean flow primarily takes place in the surface and bottom Ekman layers, while in between the flow in the latitude-depth plane is mainly vertical. As can be seen from the zonally integrated zonal momentum balance (Olbers and Ivchenko, 2001; Viebahn and Eden, 2010), in the zonally unblocked region only ageostrophic meridional transports remain (which are small because the Reynolds stress divergence is small), while at blocked depths geostrophically balanced transports

boundary condition. That is, $(u - v\partial_y x_{\mathcal{B}} - w\partial_z x_{\mathcal{B}})|_{(x_{\mathcal{B}},y,z)} = 0$ holds and by using the Leibniz integral rule one obtains the same result for the zonally integrated continuity equation.

are supported by east-west pressure differences. Accordingly, in the hill case an Ekman bottom boundary layer is absent, but the meridional surface Ekman transport is balanced by a geostrophic meridional return flow below the hill depth in the SO. Above the top of topography, the Eulerian streamfunction $\overline{\Lambda}$ of the hill case becomes similar to $\overline{\Lambda}$ in the flat case. Notice that a second local transport maximum in Fig. 3.1 b) (around $y = 400$km and $z = -800$m) indicates the meridional meanders in the time-mean flow field (see Fig. 3.5 discussed in section 3.5.2), and hence the impact of topography on the circulation above topography.

The MOC in the SO of Fig. 3.1 a,b) has been typified as the Deacon cell (Döös and Webb, 1994), which fails to give a correct picture of the net transport of watermasses in the SO. This becomes obvious by comparing $\overline{\Lambda}$ with the buoyancy field $[\overline{b}]$ (Fig. 3.1 c,d)). In both the flat case and the hill case isopycnals are strongly tilted across the SO and outcrop in the SO. For the hill case, watermasses below the top of the hill are slightly warmer and less stratified than in the flat case, but in contrast to $\overline{\Lambda}$, there is no qualitative difference between the buoyancy distributions $[\overline{b}]$ of the hill case and the flat case. However, since the interior ocean circulation (except in convective regions) is likely to be nearly adiabatic (Webb and Suginohara, 2001), the flow should mainly be oriented along mean isopycnals. Obviously, the $\overline{\Lambda}$ does not advect $[\overline{b}]$, since $\overline{\Lambda}$ suggests unrealistically strong diapycnal flow in the interior. Nevertheless, the Eulerian streamfunction $\overline{\Lambda}$ may be considered as a constitutive part of the overall MOC of the SO (given by $\overline{\psi_I}$), namely as the time- and zonal-mean part, as we discuss in section 3.5.1.

3.5 Isopycnal streamfunctions

The isopycnal meridional streamfunction ψ_I (for zonal integration along latitude circles) is the southward volume transport with buoyancy b smaller than a given value b_a across a given latitude y (Nurser and Lee, 2004a),

$$\psi_I(y, b_a, t) \equiv -\int \int_{(x,z):b(x,y,z,t)\leq b_a} v \; dx \; dz \; . \tag{3.5}$$

In appendix 3.8.3 we outline the definition of the isopycnal streamfunction via the continuity equation in isopycnal coordinates. For the time-mean of ψ_I it holds

$$\overline{\psi_I}(y, b_a) \;\; = \;\; -\int_{west}^{east} \overline{\int_{z:b(x,y,z,t)\leq b_a} v \; dz} \; dx = -\int_{bottom}^{top} \overline{\int_{x:b(x,y,z,t)\leq b_a} v \; dx} \; dz \; . \tag{3.6}$$

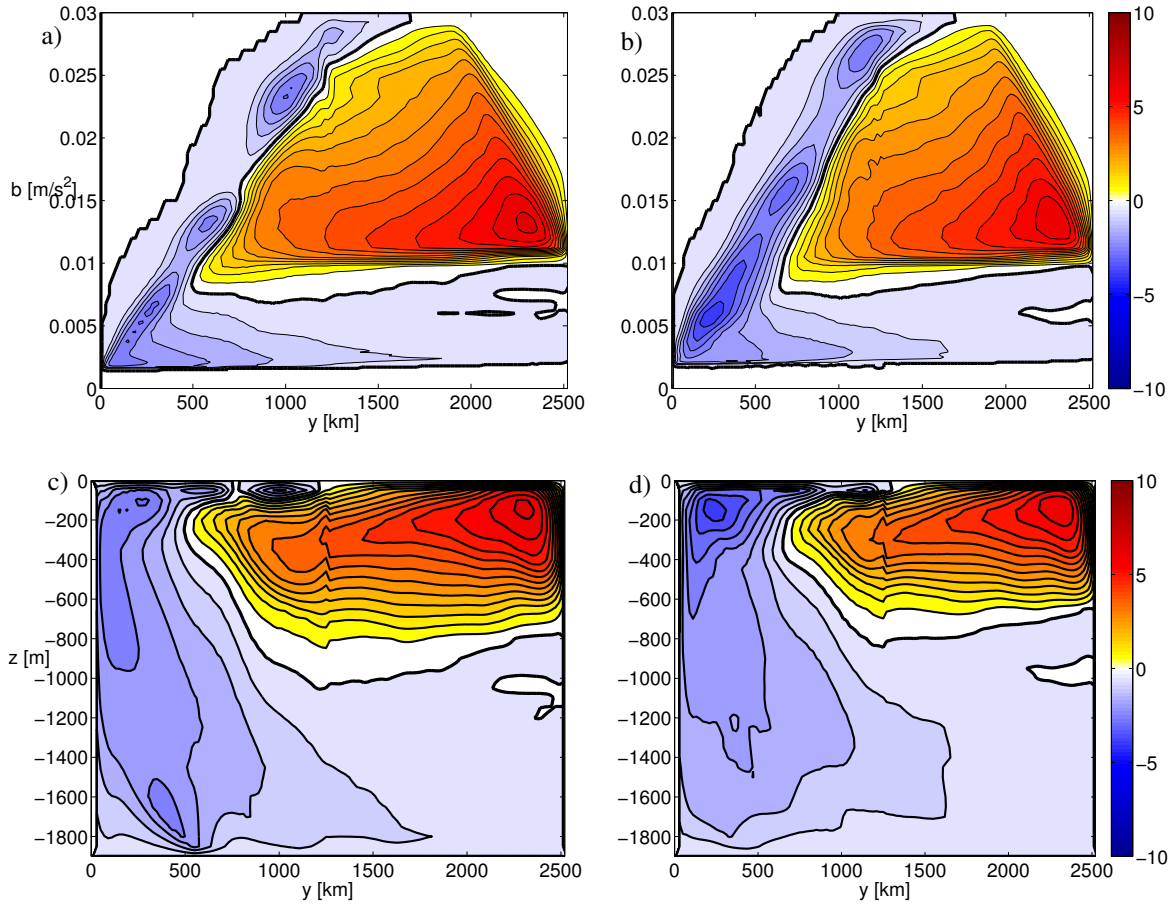

Figure 3.2: The isopycnal streamfunction ($\overline{\psi_I}$) in (top) isopycnal coordinates and (bottom) transformed to depth coordinates via the mean height of isopycnals (Nurser and Lee, 2004a) for the flat (a,c) and the hill (b,c) case. The contour interval is 0.5 Sv and zero lines are thick.

In contrast to $\overline{\Lambda}$ of Eq. (3.4), the integration condition of ψ_I shows zonal and temporal dependencies and hence the calculation of $\overline{\psi_I}$ cannot be reduced to an integral of $[\overline{v}]$. The calculation of $\overline{\psi_I}$ includes deviations from the zonal and temporal means, which we discuss in detail in section 3.5.1. As outlined by McDougall and McIntosh (2001) and Nurser and Lee (2004a), $\overline{\psi_I}$ is a streamfunction and advects the isopycnally averaged buoyancy when transformed to depth coordinates via the mean height of isopycnals (see the discussion of Fig. 3.3 below in this section).

Figure 3.2 shows $\overline{\psi_I}$ for both the flat case and the hill case in both isopycnal coordinates and depth coordinates. Similar to the buoyancy distributions, the circulation patterns implied by $\overline{\psi_I}$ are qualitatively identical for the flat case and the hill case: Two circulation

cells with opposite signs appear. In the positive cell, watermasses move adiabatically and at fairly constant mid-depth from the northern end of the domain to the south. After entering the channel at $y = 1260$km, this model NADW[3] moves nearly adiabatically further south and upward, but is slightly cooled during its ascent. At around 200m depth these watermasses turn northward and remain between 100m and 200m depth (below the negative cell) in the channel region, while in the Atlantic part the surface is reached. The northward flowing surface layer watermasses are strongly warmed until $y = 2000$km is reached. Further north, the surface watermass is strongly cooled and sinks down to mid-depth, that is, transforms to model NADW again and closes the loop. While the positive cell connects the Atlantic and SO parts, the negative cell is mainly restricted to the SO part: At the southern boundary the densest watermass of the whole domain (model AABW) sinks and moves northward near the bottom, and then, under moderate interior warming, turns back to the surface layer. After entering the surface layer this watermass flows northward under strong warming until it upwells (before it enters the Atlantic part), and then moves southward at the surface under strong cooling towards the southern boundary and the highest density values are reached again. Embedded into this surface flow are smaller-scale recirculation cells. While in the flat case the positive cell is slightly stronger (in transport) and reaches deeper and further south, in the hill case, the circulation of the negative cell is amplified in the surface layer. Altogether, watermass transformations primarily take place in the surface layer, except for some moderate diapycnal flux in the upward flow around $y = 900$km. Moreover, in both cases the surface waters of the SO part are flowing southward.

Similar isopycnal meridional streamfunctions as in Fig. 3.2 have been diagnosed in several realistic model studies (Hallberg and Gnanadesikan, 2006; Lee et al., 2007; Treguier et al., 2007). However, an entirely southward flow in the SO conflicts with northward wind-driven Ekman transport. Treguier et al. (2007) conclude that this southward surface flow is largely a contribution due to the permanent meanders ("standing eddies") of the time-mean flow. Therefore, they suggest that it is essential to turn to a framework in which standing eddies vanish or are reduced, in order to understand the MOC in the SO and its relationship to surface forcing. In section 3.5.1 we consider the contribution of standing eddies to the streamfunctions in Fig. 3.2, while in section 3.5.2 we discuss different possibilities of minimising the impact of standing eddies on the isopycnal meridional streamfunction $\overline{\psi_I}$.

$\overline{\psi_I}$, remapped to Eulerian space, advects the isopycnally averaged buoyancy. In case of

[3] In this study we use the following standard abbreviations for oceanic watermasses: North Atlantic Deep Water (NADW) and Antarctic Bottom Water (AABW).

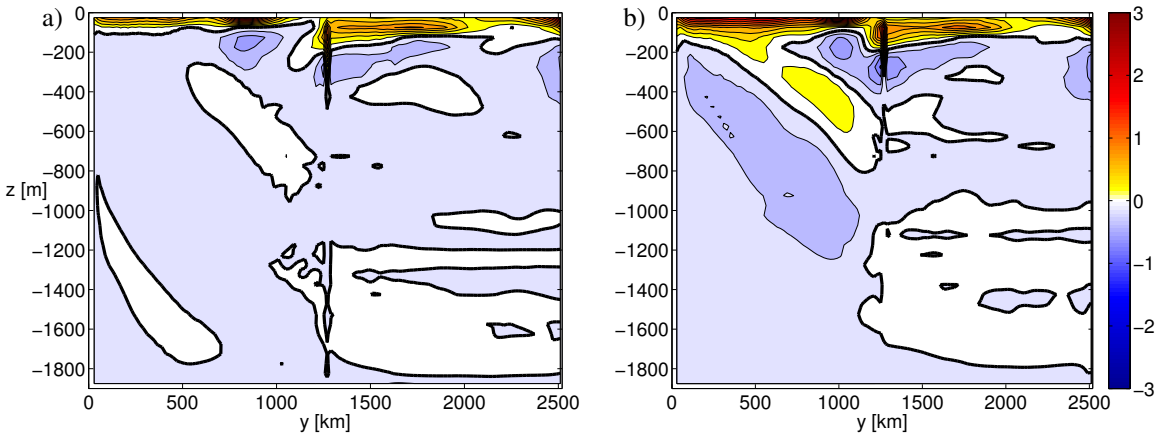

Figure 3.3: The difference (multiplied by 10^3) between the time-mean of the isopycnally averaged buoyancy and $[\overline{b}]$ (shown in Fig. 3.1) for the flat (a) and the hill (b) case. The contour interval is $0.2m/s^2$ and zero lines are thick.

isopycnal averaging at constant latitude, the zonal-mean ("isopycnally" averaged) isopycnals are defined via the mean heights of the isopycnals at constant latitude (McDougall and McIntosh, 2001; Nurser and Lee, 2004a). The mean surface density becomes the lightest water ever found at a given latitude, which may differ substantially from the Eulerian mean surface density. Figure 3.3 shows the difference between the time-mean of the isopycnally averaged buoyancy (not shown) and the Eulerian zonal and time-mean buoyancy distribution (shown in Fig. 3.1) for both the flat case and the hill case. In both cases differences primarily occur in the diabatic surface layer and, as expected, surface waters are more buoyant in case of isopycnal averaging than for Eulerian averaging. Notice that the differences are about one order of magnitude smaller than the buoyancy fields. Hence, the isopycnally averaged buoyancy distributions (not shown) are very similar to the Eulerian mean buoyancy distributions (shown and described in section 3.4), except that near the surface isopycnals are less steep (in accordance with the results of Nurser and Lee (2004a)). In the hill case differences are quantitatively more pronounced than in the flat case. However, as for the buoyancy distributions, the differences are qualitatively similar for both cases.

3.5.1 Transient and standing eddies

For each quantity q, we define its temporal deviation as $q^\circ \equiv q - \overline{q}$ (including all time dependency of q) and its zonal deviation as $q^+ \equiv q - [q]$ (including all zonal dependency

of q). The zonal and temporal deviation, $q' \equiv q - [\overline{q}]$, can then be expressed in two ways[4]: On the one hand, we can separate the temporal deviation q° such that $q' = \overline{q}^+ + q^\circ$, on the other hand, we can separate the zonal deviation q^+ such that $q' = [q^\circ] + q^+$. Obviously, in each case the first term belongs to a mean part, namely either to the time-mean part $\overline{q} = [\overline{q}] + \overline{q}^+$, or to the zonal-mean part $[q] = [\overline{q}] + [q^\circ]$ of the quantity q.

We focus on the first decomposition[5], where the temporal deviation q° is the so-called *transient eddy* term, and the temporal mean of the zonal deviation, $\overline{q}^+$, is the so-called *standing eddy* term. The latter emerges from persistent zonal inhomogeneities and, as mentioned, belongs dynamically to the time-mean circulation $\overline{q}$.

Using the decomposed fields of buoyancy $b = [\overline{b}] + \overline{b^+} + b^\circ$ and meridional velocity $v = [\overline{v}] + \overline{v^+} + v^\circ$, the time-mean isopycnal streamfunction $\overline{\psi_I}(y, b)$ (see Eq. (3.6)) may also be decomposed into a time- and zonal-mean part ($\overline{\Lambda}_I$), a standing eddy part ($\hat{\psi}^*_I$) and a transient eddy part ($\tilde{\psi}^*_I$): The time- and zonal-mean part $\overline{\Lambda}_I$ of the isopycnal streamfunction $\overline{\psi_I}$ is related to the time- and zonal-mean parts of b and v,

$$\overline{\Lambda}_I \equiv - \int_{z:[\overline{b}](y,z) \le b_a} L[\overline{v}] \; dz \; . \tag{3.7}$$

$\overline{\Lambda}_I$ may be considered as the Eulerian streamfunction in isopycnal coordinates: For our model results, $\overline{\Lambda}_I$, transformed to depth coordinates using the mean heights of $[\overline{b}]$ (Nurser and Lee, 2004a), is identical to $\overline{\Lambda}$ given by Eq. (3.4) (Fig. 3.1 a,b)). This is due to the vertically monotonic buoyancy distribution $[\overline{b}]$ (see Fig. 3.1 c,d)).

Following the definition of a standing eddy term, the standing eddy part of $\overline{\psi_I}$ is given by the difference between $\overline{\Lambda}_I$ (constituted by the time- and zonal-mean parts of b and v) and the isopycnal streamfunction which is given by the time-mean parts of b and v,

$$\hat{\psi}^*_I \equiv - \int \int_{(x,z):\overline{b}(x,y,z) \le b_a} \overline{v} \; dx \; dz - \overline{\Lambda}_I \; . \tag{3.8}$$

That is, both $\overline{\Lambda}_I$ and $\hat{\psi}^*_I$ are solely related to time-mean quantities. Finally, the transient eddy part of $\overline{\psi_I}$ is the residuum,

$$\tilde{\psi}^*_I \equiv \overline{\psi}_I + \int \int_{(x,z):\overline{b}(x,y,z) \le b_a} \overline{v} \; dx \; dz = \overline{\psi}_I - \overline{\Lambda}_I - \hat{\psi}^*_I \; , \tag{3.9}$$

[4] Notice that $[\overline{q}] = \overline{[q]}$ implies $[q^\circ] = [q]^\circ$ and $\overline{q}^+ = \overline{q^+}$.

[5] For our model experiments we found that the second decomposition is meaningless. More precisely, we found that the temporal correlations of the zonally averaged temporal deviations, $\overline{[v^\circ][b^\circ]}$, vanish.

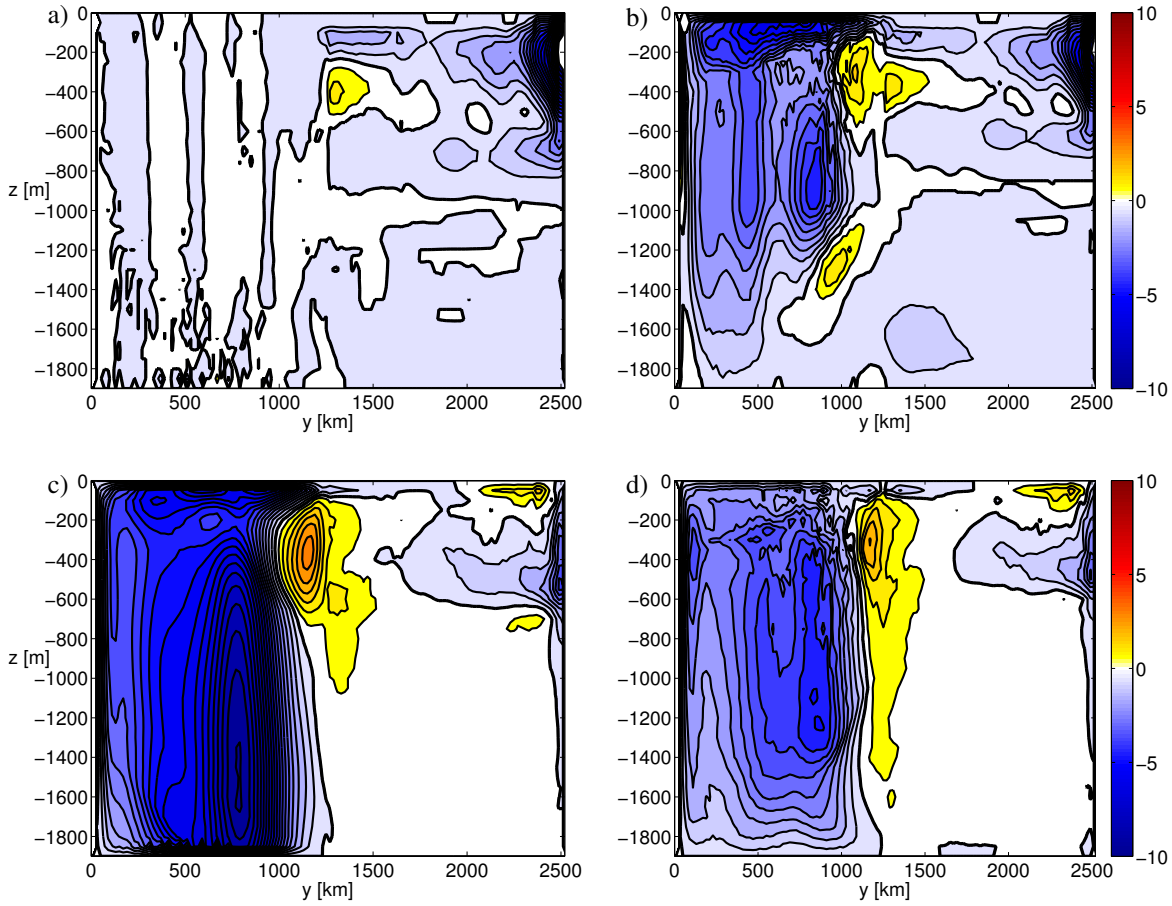

Figure 3.4: Top: The standing eddy streamfunction ($\hat{\psi}_I^*$) for the flat (a) and the hill (b) case. Bottom: The transient eddy streamfunction ($\tilde{\psi}_I^*$) for the flat (c) and the hill (d) case. The contour interval is 0.5 Sv and zero lines are thick. They were transformed to depth coordinates via the mean height of the respective isopycnals (Nurser and Lee, 2004a).

and hence $\tilde{\psi}_I^*$ is implicitly related to the transient eddy parts of b and v. Altogether, we obtain the following decomposition of $\overline{\psi_I}(y, b)$,

$$\overline{\psi_I} = \overline{\Lambda}_I + \hat{\psi}_I^* + \tilde{\psi}_I^* \ . \tag{3.10}$$

Figure 3.4 shows the standing eddy streamfunction $\hat{\psi}_I^*$ and the transient eddy streamfunction $\tilde{\psi}_I^*$ for both the flat case and the hill case. In the flat case, the standing eddy streamfunction $\hat{\psi}_I^*$ vanishes in the channel part of the model. This may be understood as follows: In the flat case, isolines at fixed depth of time-mean buoyancy $\overline{b}$ essentially coincide

with latitude circles in the channel part (as described in detail in section 3.5.2). Therefore, the corresponding standing eddy part of buoyancy vanishes, $\overline{b^+} = 0$. Consequently, the integration conditions in Eq. (3.7) and Eq. (3.8) coincide and hence the standing eddy streamfunction $\hat{\psi}_I^*$ vanishes, which is independent of the integrands in Eq. (3.7) and Eq. (3.8). Notice that time-mean streamlines in the flat case also essentially coincide with latitude circles at each depth, except in the boundary layers, where significant meridional components (Ekman transport) are present (as seen in $\overline{\Lambda}$ in Fig. 3.1 a)).

Turning back to Fig. 3.4, we find that in the Atlantic part the standing eddy streamfunctions $\hat{\psi}_I^*$ of the flat case and the hill case are nearly identical: In the convective region at the northern boundary, a negative circulation cell appears, which reduces the positive circulation cell of $\overline{\Lambda}$ (Fig. 3.1) in the overall MOC $\overline{\psi_I}$ (Fig. 3.2). Outside the convective region, the standing eddy circulation $\hat{\psi}_I^*$ is small in the Atlantic part. In contrast to the flat case, the hill case shows also strong standing eddy circulations in the channel part: At mid-depth and in particular in the surface layer, negative circulation cells counteract the local transport maxima and the Ekman transport of $\overline{\Lambda}$ (Fig. 3.1), while with deeper depths, $\hat{\psi}_I^*$ becomes smaller (just like $\overline{\Lambda}$). As expected, the surface poleward transport in $\overline{\psi_I}$ (Fig. 3.2 d)) of the hill case is due to the standing eddy streamfunction $\hat{\psi}_I^*$, while the transient eddy streamfunction $\tilde{\psi}_I^*$ of the hill case is small in the surface layer. However, besides the surface layer, $\tilde{\psi}_I^*$ is of the same magnitude as $\hat{\psi}_I^*$ in our idealised model (in contrast to the suggestions of Karoly et al. (1997) and in accordance with Lee and Coward (2003)). Just like $\hat{\psi}_I^*$ and $\overline{\Lambda}$, the transient eddy streamfunction $\tilde{\psi}_I^*$ of the hill case contains two local transport maxima at mid-depth, but in contrast to $\hat{\psi}_I^*$ and $\overline{\Lambda}$, the maximal values reach deeper under the top of topography (down to 1400m depth).

In the Atlantic part, $\tilde{\psi}_I^*$ of the flat case and the hill case are also nearly identical: A negative circulation cell appears in the convective region at the northern boundary of the domain (similar to $\hat{\psi}_I^*$ but smaller in magnitude) together with a small positive recirculation cell in the surface layer. However, in the channel part the transient eddy streamfunctions $\tilde{\psi}_I^*$ of the flat case and the hill case show substantial differences: In the flat case, $\tilde{\psi}_I^*$ contains only one local maximum (counteracting the corresponding local maximum of $\overline{\Lambda}$ in Fig. 3.1 a)) outside the surface layer, which occurs at deeper depths (around -1600m) and is stronger in magnitude. Moreover, a second strong negative circulation cell appears in the surface layer that accounts for the poleward transport in the overall MOC $\overline{\psi_I}$ of the flat case (Fig. 3.2 c)).

We conclude, that in the hill case the southward surface transport in the overall MOC $\overline{\psi_I}$

(Fig. 3.2 d)) is due to the standing eddy part $\hat{\psi}_I^*$. We therefore consider zonal integration paths that lead to a reduction (or at best a vanishing) of the standing eddy part $\hat{\psi}_I^*$ in the next section 3.5.2.

3.5.2 MOCs with reduced standing eddy circulation

A zonal-mean meridional transport function should possess the properties of a streamfunction: The respective derivatives have to give the zonal-mean meridional and vertical (or diapycnal) flow. That is, mass balance has to be guaranteed and therefore zonal integration paths and the cross-path transport velocity have to be determined in accordance with the continuity equation. In arbitrary coordinates $(m, n, \tilde{z})$ (see appendix 3.8.1) the continuity equation reads (Aris, 1989)

$$\nabla \cdot \mathbf{v} \equiv \frac{1}{\sqrt{g}} \left[\partial_m \left(\sqrt{g}\ u^m \right) + \partial_n \left(\sqrt{g}\ v^n \right) + \partial_{\tilde{z}} \left(\sqrt{g}\ w^{\tilde{z}} \right) \right] = 0 \ , \tag{3.11}$$

where $g = det(g_{ij})$ and $u^m, v^n, w^{\tilde{z}}$ are the contravariant components of the velocity vector $\mathbf{v}$ in the coordinate system $(m, n, \tilde{z})$ (see appendix 3.8.1). Notice that the form of Eq. (3.11) is completely general such that we could equally well consider a framework of isopycnal coordinates $(\tilde{m}, \tilde{n}, b)$ (see appendix 3.8.3). The continuity equation (3.11) implies that integration paths and cross-path transport velocity have to satisfy the following conditions:

(i) Above topography the zonal integration paths (coordinate lines of m) have to be closed[6].

(ii) At and below topographic heights the sum of boundary terms, resulting from zonal integration and interchanging integration and differentiation, has to vanish.

(iii) The cross-path transport velocity v_c has to be defined via the contravariant meridional velocity v^n of the coordinate system (up to a metrical factor).

While conditions (i) and (iii) have to be discussed in conjunction with the specific zonal integration paths, condition (ii) may be considered subject to the boundary conditions, as outlined in appendix 3.8.2. Cartesian coordinates represent the only familiar coordinate system, where condition (ii) is always exactly satisfied by solely imposing the boundary

[6] In this study *closed* curves are circumpolar horizontal paths which take the same latitude at the western and eastern boundaries of the channel.

condition of no-normal-flow at topographic barriers. Otherwise, further boundary conditions have to be included, e.g. the no-slip boundary condition (which has been implemented in our experiments).

Zonal integration along time-mean horizontal streamlines

Time-mean horizontal streamlines are defined as the integral curves of the horizontal time-mean velocity vector field $\overline{\mathbf{u}} = (\overline{u}, \overline{v}, 0)$: At each point of a streamline the corresponding velocity vector $\overline{\mathbf{u}}$ is tangential to the streamline. Adopting the horizontal time-mean streamlines as the new zonal coordinate lines, we obtain for the unit tangential vector $\mathbf{e}_m = \overline{\mathbf{u}}/|\overline{\mathbf{u}}|$ and consequently for the unit normal vector $\mathbf{e}_n = (-\overline{v}, \overline{u}, 0)/|\overline{\mathbf{u}}|$.

As stated in condition (iii), the cross-path transport velocity (which constitutes the integrand of $\hat{\psi}^*$) is given by the contravariant meridional velocity v^n, $v^n\sqrt{g_{nn}} = \mathbf{v} \cdot \mathbf{e}_n + w(\partial_z n/|\nabla_h n|)$ (see appendix 3.8.1). The first term represents the projection of the overall velocity on the horizontal normal vector of the horizontal integration path, while the second term represents an additional non-orthogonality term. In case of time-mean horizontal streamlines, the first term is given by $\mathbf{v} \cdot \mathbf{e}_n = (v^\circ\overline{u} - u^\circ\overline{v})/|\overline{\mathbf{u}}|$, which is a pure transient eddy velocity (the time-mean vanishes). The time-mean of the non-orthogonality term, $\overline{w}(\partial_z n/|\nabla_h n|)$, does not vanish in general, and hence has to be included in the calculation of both the standing eddy streamfunction $\hat{\psi}^*$ and the Eulerian streamfunction Λ_I. Only if the time-mean horizontal streamlines are depth-independent, the curvilinear coordinates system is orthogonal and the non-orthogonality term can be neglected. Under such conditions we obtain the desired result: The time-mean of the cross-path transport velocity vanishes, and consequently, both the standing eddy streamfunction $\hat{\psi}_I^*$ *and* the Eulerian streamfunction $\overline{\Lambda}_I$ vanish, $\hat{\psi}_I^* \equiv 0$ and $\overline{\Lambda}_I \equiv 0$ (see Eq. (3.7) and (3.8)). Hence, the meridional streamfunction ψ_I is given by the transient eddy streamfunction $\tilde{\psi}_I^*$ only, $\psi_I \equiv \tilde{\psi}_I^*$. Notice that the other basic physical quantities $(u, b, ...)$ in general do not have a vanishing time-mean or standing eddy part.

Time-mean horizontal streamlines in the flat case and the hill case Figure 3.5 shows the time-mean horizontal streamlines, determined by a direct numerical integration of the horizontal time-mean velocity vector field $\overline{\mathbf{u}} = (\overline{u}, \overline{v}, 0)$, in the SO region at selected depths for both the flat case and the hill case. In the flat case, streamlines in the SO region essentially coincide with latitude circles and are directed eastward at almost each depth (e.g. Fig. 3.5 b)). Only near the surface (down to 50m depth) streamlines have a significant

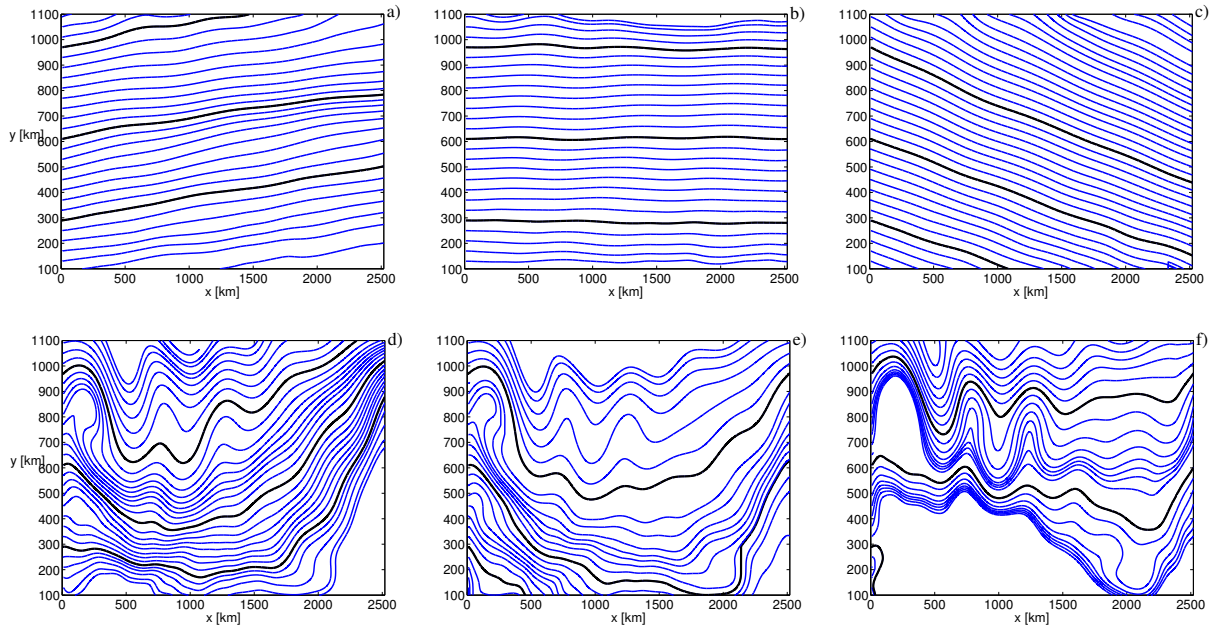

Figure 3.5: Time-mean horizontal streamlines in the SO region for (top) the flat case at $z = -25$m (a), $z = -75$m (b), $z = -1875$m (c) and (bottom) the hill case at $z = -25$m (d), $z = -75$m (e), $z = -825$m (f). In each case streamlines with a starting point at $x = 0$ and $y = 290$km, 610km, 970km are black and thick.

northward component (Fig. 3.5 a)) and near the bottom (in the deepest 50m) streamlines have a corresponding southward component (Fig. 3.5 c)). Hence, time-mean horizontal streamlines are not closed in the Ekman layers. Outside the surface and bottom boundary layers, the eastward flow in the entire SO region is vertically homogeneous[7]. Moreover, in the SO region, horizontal isolines of the time-mean geostrophic streamfunction $\overline{p}/f_0$ (not shown) coincide with latitude circles at each depth and hence essentially coincide with time-mean horizontal streamlines outside the boundary layers. In the boundary layers, the geostrophic streamfunction $\overline{p}/f_0$ is unable to capture the meridional components of the circulation.

In the hill case, the time-mean streamline pattern is more complicated. In the SO region, time-mean streamlines are highly undulated and at larger depth dominantly cyclonic recirculation cells appear[8]. Hence, a nearly vertically homogeneous structure of the flow field is found only in a small region. More precisely, the sector roughly given by

[7] Notice that the time-mean Eulerian streamfunction $\overline{\Lambda}$ (Fig. 3.1 a)) gives a concise picture of the MOC given by the time-mean velocity field in the SO region (in the flat case).

[8] In Fig. 3.5 mainly circumpolar time-mean horizontal streamlines are shown. Recirculation cells are present in the broad plain white regions of Fig. 3.5 f) and are visualised in Fig. 3.6 b, c).

800km $\leq y \leq$ 1100km and $0 \leq x \leq$ 1600km represents the region of undulated streamlines, which change the least with depth. For $x >$ 1600km, the topography overflowing current is less undulated, but turns from a north-eastward flow in the upper 700m (Fig. 3.5 d, e) and Fig. 3.6 a)) into a south-eastward flow for $z \leq -1000$m (Fig. 3.6 c)). The opposite behaviour is found eastward of the top of topography ($0 \leq x \leq$ 850km, $0 \leq y \leq$ 700km): The topography overflowing current turns from a south-eastward flow into a north-eastward flow at larger depth. In between (850km $\leq x \leq$ 1690km), streamlines are mainly zonal in the upper 500m (Fig. 3.5 d, e) and Fig. 3.6 a)). However, at larger depth a cyclonic recirculation pattern emerges at the southern boundary (centerd around $x =$ 1000km), which extends to $y =$ 500km at 900m depth and includes smaller recirculation cells at larger depth (Fig. 3.6 b, c)).

Notice that also in the hill case time-mean horizontal streamlines are not closed in the surface layer (Fig. 3.5 d)), and that the meridional shift is larger in the hill case than in the flat case. Nevertheless, below the surface layer time-mean horizontal streamlines are closed (Fig. 3.5 e, f)). That is, below the surface layer time-mean horizontal streamlines may be represented by horizontal contours of a scalar field, e.g. the time-mean geostrophic streamfunction $\overline{p}/f_0$.

Figure 3.6 shows the time-mean geostrophic streamfunction $\overline{p}/f_0$ at selected depths for the hill case. Horizontal isolines of $\overline{p}/f_0$ essentially coincide with time-mean horizontal streamlines, except in the surface Ekman layer. In contrast to the flat case, a bottom boundary layer is absent in the hill case (see Fig. 3.1 b)), but the deep return flow (balancing the topographically and wind-induced Ekman surface transport) is geostrophically balanced by east-west pressure differences. We note that the topographically induced geostrophic meridional excursions (Fig. 3.6 a)) and the ageostrophic surface meridional shift (Fig. 3.5 d)) are of the same order.

We conclude: In our model results, time-mean horizontal streamlines may be well approximated by horizontal contours of $\overline{p}/f_0$ outside the boundary layers, while in the Ekman layers significant deviations occur. In particular, time-mean horizontal streamlines are not closed in the Ekman layers. Moreover, in the hill case the time-mean flow field of the ocean interior (excluding the boundary layers) shows a significant depth-dependence.

Conclusions from numerical model results The time-mean horizontal streamlines in our two model experiments suggests that zonal integration along those lines may only lead to a reduction of the standing eddy part $\hat{\psi}_I^*$, but not to an exact vanishing: On the one

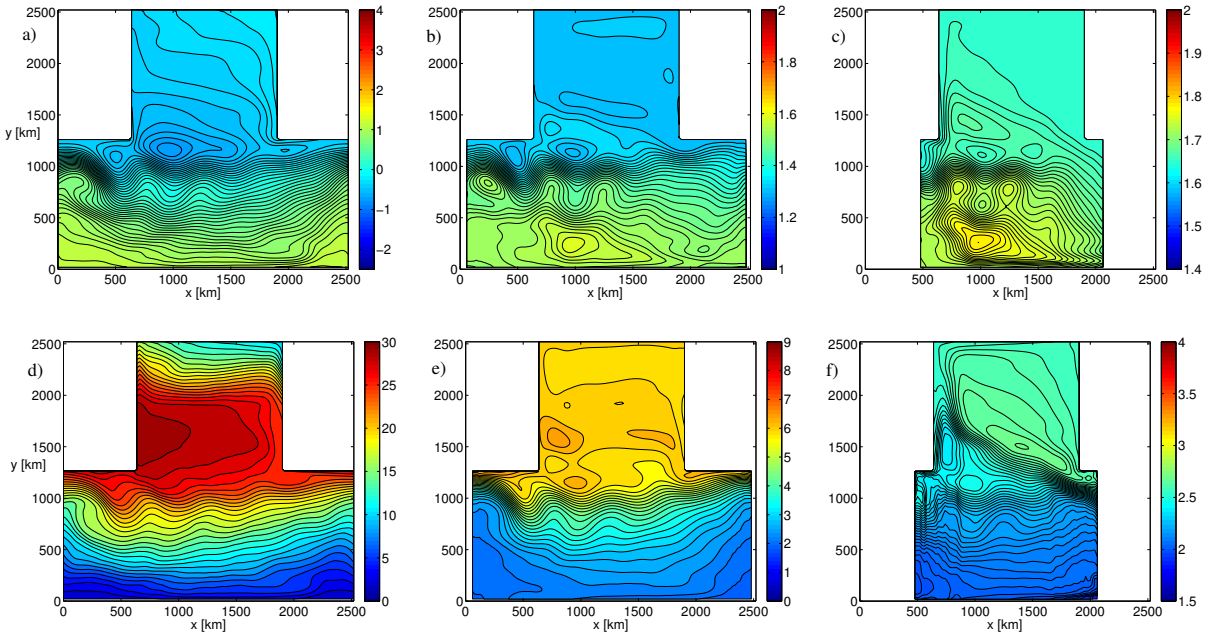

Figure 3.6: Top: Time-mean geostrophic streamfunction $\overline{p}/f_0$ [10^5 m^2/s] of the hill case at $z = -25$m with a contour interval of 5×10^3 m^2/s (a), $z = -975$m with a contour interval of 1×10^3 m^2/s (b) and $z = -1525$m with a contour interval of 5×10^2 m^2/s (c). Bottom: Time-mean buoyancy $\overline{b}$ [10^{-3} m/s^2] of the hill case at $z = -25$m with a contour interval of 1×10^{-3} m/s^2 (d), $z = -975$m with a contour interval of 2×10^{-2} m/s^2 (e) and $z = -1525$m with a contour interval of 2×10^{-1} m/s^2 (f).

hand, time-mean horizontal streamlines are not closed at each depth, that is, condition (i) is in general not satisfied, since in the surface Ekman layer the flow is horizontally divergent. In order to satisfy condition (i), streamlines have to be approximated by e.g. the geostrophic streamfunction $\overline{p}/f_0$. However, the Ekman component is missed in that case and therefore both the standing eddy streamfunction $\hat{\psi}^*$ and $\overline{\Lambda}_I$ generally will not vanish. On the other hand, time-mean horizontal (geostrophic) streamlines significantly change with depth. Therefore, the curvilinear coordinate system induced by this set of horizontal paths has to be considered in general non-orthogonal. Consequently, the non-orthogonality term $w(\partial_z n/|\nabla_h n|)$ can not be considered to be small and hence, has to be included. The time-mean of the cross-path transport velocity for zonal integration along horizontal time-mean geostrophic streamlines (that is, $n \simeq \overline{p}/f_0$), $\overline{v^n} \approx \overline{w}\partial_z\overline{p}$, in general does not vanish, and therefore, one has to expect that both the standing eddy streamfunction $\hat{\psi}^*$ and $\overline{\Lambda}_I$ generally do not vanish.

Finally, we note that the flat case represents a special case in this respect: In the flat case isolines of $\overline{p}/f_0$ coincide with both, latitude circles and isolines of time-mean buoyancy (not shown). It is due to the latter coincidence, as we discuss in the next section, that the standing eddy streamfunction $\hat{\psi}^*$ has to vanish in this case (see Fig. 3.4 a)), but $\overline{\Lambda}_I$ apparently does not vanish (see Fig. 3.1 a)).

Zonal integration along horizontal isolines of time-mean buoyancy $\overline{b}$

Using horizontal isolines of $\overline{b}$ as the zonal coordinate lines, condition (i) is satisfied by definition. The unit normal vector becomes $\mathbf{e}_n = (\nabla_h \overline{b}, 0)/|\nabla_h \overline{b}|$ and therefore, the unit tangential vector reads $\mathbf{e}_m = (\partial_y \overline{b}, -\partial_x \overline{b}, 0)/|\nabla_y \overline{b}|$. Consequently, the time-mean of the first term of the cross-path transport velocity v^n, i.e. the instantaneous horizontal velocity across horizontal time-mean buoyancy contours $\mathbf{v} \cdot \mathbf{e}_n = \mathbf{u} \cdot (\nabla_h \overline{b}, 0)/|\nabla_h \overline{b}|$, generally does not vanish. Hence, even in case horizontal $\overline{b}$ contours are depth-independent, such that the induced curvilinear coordinate system is orthogonal, the cross-path transport velocity v^n generally has both, a non-vanishing time- and zonal-mean component, $[\overline{v^n}]$, and a non-vanishing standing eddy component, $\overline{v^n}^+$. Therefore, the Eulerian streamfunction $\overline{\Lambda}_I$ (see Eq. (3.7)) generally does not vanish too.

However, the standing eddy component of the buoyancy field b vanishes, i.e. $\overline{b}^+ \equiv 0$. Therefore, the time-mean part of $\overline{\psi_I}$ (given by $\hat{\psi}^* + \overline{\Lambda}_I$) and the time- and zonal-mean part of $\overline{\psi_I}$ (given by $\overline{\Lambda}_I$) are identical (see Eq. (3.7) and (3.8)) and hence, the standing eddy streamfunction $\hat{\psi}_I^*$ vanishes. This result is solely constituted by the zonal integration conditions. Therefore, it is *independent of the determination of the cross-path transport velocity*. In other words, in case zonal integration paths are determined by horizontal contours of $\overline{b}$, a vanishing standing eddy streamfunction is not affected by the non-orthogonality of the curvilinear coordinate system, since it relies only on the integration conditions, but not on the integrand of $\hat{\psi}_I^*$ (that is, cross-path transport velocity).

We conclude: Horizontal isolines of $\overline{b}$ may be used without approximation (condition (i) is always satisfied) as zonal integration paths for the construction of a zonal-mean meridional streamfunction, and moreover, the corresponding standing eddy streamfunction $\hat{\psi}_I^*$ exactly vanishes, even in the general non-orthogonal case.

Horizontal isolines of time-mean buoyancy in the flat case and the hill case In the flat case, horizontal isolines of $\overline{b}$ (not shown) coincide with latitude circles and hence also with geostrophic streamlines at each depth in the SO region. In contrast, in the hill case

both coincidences are lost. Figure 3.6 also shows $\overline{b}$ at selected depths for the hill case. In the SO region, horizontal isolines of $\overline{b}$ are roughly analogue to isolines of $\overline{p}/f_0$ in the upper 600m (see Fig. 3.6 a,d)). However, going to deeper depths the structure of contours of $\overline{b}$ changes much less than the structure of isolines of $\overline{p}/f_0$ (or horizontal streamlines) (see Fig. 3.6). In particular, isolines of $\overline{b}$ remain nearly void of recirculation cells in the SO region. The meandering of contours increases with depth, but much more isolines of $\overline{b}$ (than of $\overline{p}/f_0$) extend over the whole zonal extension at deeper depths. In other words, at depth the deviation from latitude circles is much smaller for isolines of $\overline{b}$ than for isolines of $\overline{p}/f_0$ (or horizontal streamlines).

MOCs in case of orthogonal approximations

The construction of a zonal-mean meridional streamfunction with an exactly vanishing standing eddy part $\hat{\psi}_I^*$ should be performed by zonal integration along depth-dependent horizontal isolines of time-mean buoyancy. However, in this case we would have to deal with non-orthogonal coordinates, with considerable technical complications. The following procedure to minimise the standing eddy part $\hat{\psi}_I^*$ may represent a practical compromise: The contours of $\overline{b}$ (or $\overline{p}/f_0$) at a certain depth ("contour-depth" in the following) are used for zonal integration at all depths. Thereby, the applied curvilinear coordinate system is orthogonal. The continuity equation Eq. (3.11) becomes

$$\partial_m \left[\sqrt{g_{nn}} \, (\mathbf{v} \cdot \mathbf{e}_m) \right] + \partial_n \left[\sqrt{g_{mm}} \, (\mathbf{v} \cdot \mathbf{e}_n) \right] + \partial_z \left[\sqrt{g_{mm} g_{nn}} \, w \right] = 0 \ , \tag{3.12}$$

such that the cross-path transport velocity reduces to the projection of the overall velocity on the horizontal normal vector of the horizontal integration path, $\mathbf{v} \cdot \mathbf{e}_n$. However, in case the horizontal contours of time-mean buoyancy $\overline{b}$ (or $\overline{p}/f_0$) significantly change with depth, the standing eddy streamfunction $\hat{\psi}_I^*$ now exactly vanishes at the contour-depth only, where the zonal coordinate lines are identical to the horizontal contours of $\overline{b}$, such that $\overline{b}^+ = 0$ holds (or zonal coordinate lines may be identical to horizontal time-mean streamlines, such that $\overline{\mathbf{v} \cdot \mathbf{e}_n} = 0$ holds). At other depths, the standing eddy streamfunction $\hat{\psi}_I^*$ does not vanish in general. The optimal contour-depth is then defined by the minimal[9], but in general not completely vanishing, standing eddy part $\hat{\psi}_I^*$.

Figure 3.7 shows the standing eddy streamfunctions $\hat{\psi}_I^*$ of the hill case, where zonal

[9] $\hat{\psi}_I^*$ is minimal in comparison with the standing eddy parts related to all other contour-depths.

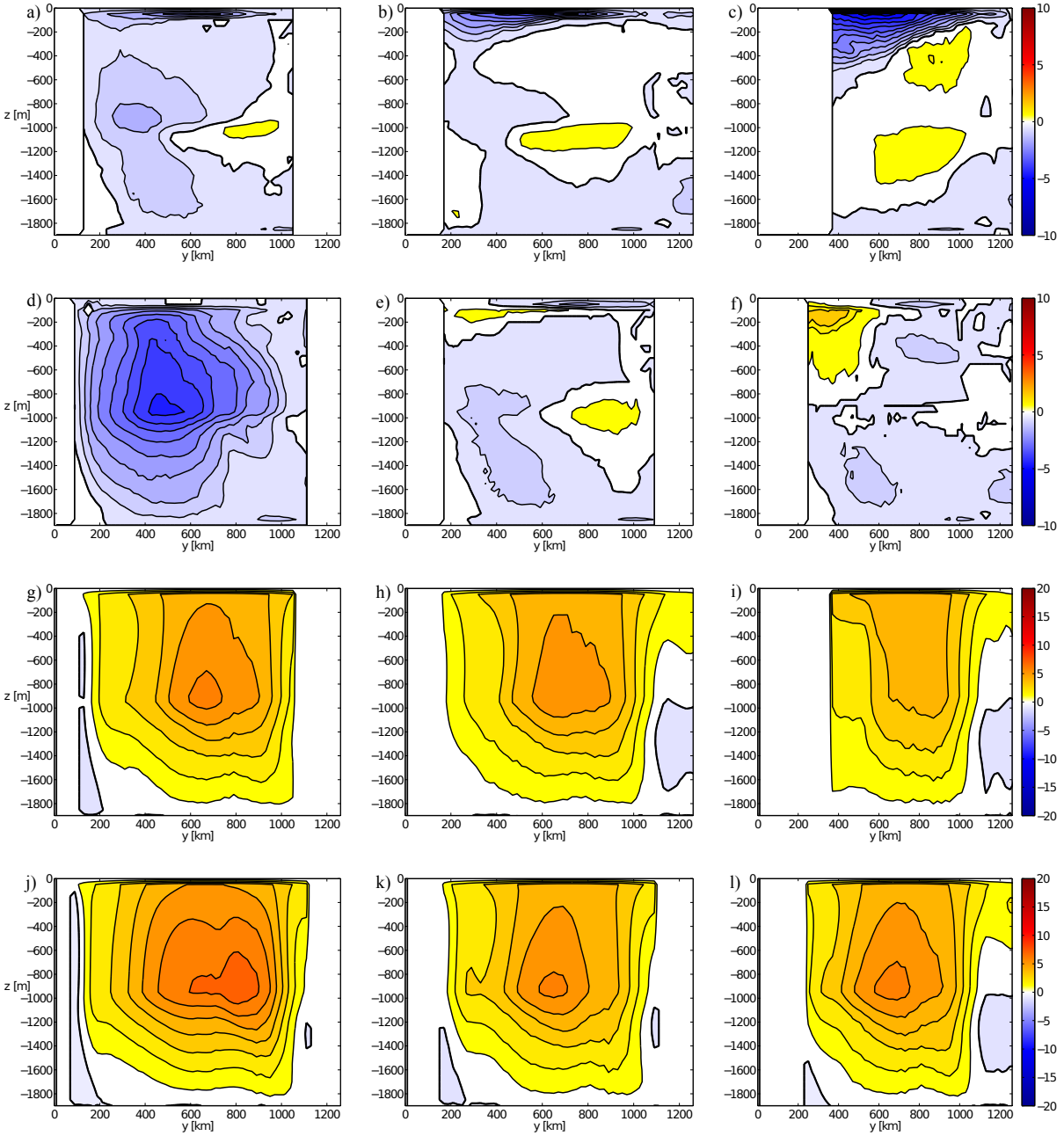

Figure 3.7: Standing eddy streamfunctions $\hat{\psi}_I^*$ for zonal integration along time-mean geostrophic streamlines (a-c) and isolines of time-mean buoyancy $\overline{b}$ (d-f). Eulerian streamfunctions $\overline{\Lambda}_I$ for zonal integration along time-mean geostrophic streamlines (g-i) and isolines of time-mean buoyancy $\overline{b}$ (j-l). From left to right the contour-depths are given by $z = -25$m, $z = -475$m and $z = -925$m.

integration is performed along horizontal isolines of either $\overline{p}/f_0$ or $\overline{b}$ at three selected contour-depths. In case $\overline{p}/f_0$ near the surface is used, we find three regions of significant standing eddy circulation (Fig. 3.7 a)): Two circulation patterns are located around the top of topography, namely a positive pattern located around $y = 800$km and a negative pattern of broader vertical extension and slightly larger magnitude located around $y = 400$km. However, the largest magnitudes are given by the negative third pattern situated in the surface layer. This pattern is due to the absence of the significant ageostrophic flow field component in the geostrophic surface streamlines. In contrast, in case the contour-depth for $\overline{p}/f_0$ lies below the surface layer, the standing eddy circulation $\hat{\psi}_I^*$ vanishes at the corresponding contour-depth (Fig. 3.7 b,c)). Moreover, with deeper contour-depths the negative circulation pattern around the top of topography diminishes and finally vanishes for contour-depths below $z = -325$m (Fig. 3.7 b)). However, simultaneously the positive circulation pattern extends with deeper contour-depths (by nearly constant magnitude) and for contour-depths below $z = -700$m a second corresponding positive circulation pattern at mid-depth appears (Fig. 3.7 c)). In addition and most important, with deeper contours-depths the negative circulation pattern in the surface layer extends vertically and significantly increases in magnitude with the maximal values near the surface (Fig. 3.7 a-c)). Consequently, using $\overline{p}/f_0$-isolines for zonal integration, the surface layer represents the contour-depths with minimal overall and surface layer standing eddy circulation $\hat{\psi}_I^*$ in our model experiment. However, a significant standing eddy circulation $\hat{\psi}_I^*$ in the surface layer appears unavoidable for $\overline{p}/f_0$ due to the missing ageostrophic surface layer component.

In contrast, using $\overline{b}$-isolines for zonal integration, the standing eddy circulation $\hat{\psi}_I^*$ vanishes at each contour-depth (including the surface layer), since no approximation is involved (Fig. 3.7 d-f)). However, for a contour-depth of $z = -25$m a strong, broad and deep reaching standing eddy circulation $\hat{\psi}_I^*$ appears below the contour-depth. Applying slightly deeper contour-depths, this large circulation pattern decomposes into an ensemble of circulation patterns similar to those obtained by zonal integration along $\overline{p}/f_0$-isolines with a contour-depth of $z = -25$m: On the one hand, a positive pattern is located around $y = 900$km and a negative pattern of broader vertical extension is located around $y = 400$km, which both are situated around the top of topography. On the other hand, a negative and small third pattern is situated in the surface layer. This similarity in the standing eddy circulations reflects the similarity between $\overline{p}/f_0$- and $\overline{b}$-isolines in the upper layers (below the uppermost layer). However, the depth-dependencies of these two types of zonal paths differ more and more with deeper depths and hence the dependency of the contour-depth of the

standing eddy circulations does too. Using $\overline{b}$-isolines for zonal integration, both circulation patterns situated around the top of topography diminish with deeper contour-depths and eventually vanish (the positive one at a contour-depth of $z = -575$m and the negative one at $z = -925$m). Moreover, the negative circulation pattern in the surface layer slightly increases in magnitude and extension down to a contour-depth of $z = -400$m, but then decreases again such that it nearly vanishes for a contour-depth of $z = -925$m. In contrast to zonal integration along $\overline{p}/f_0$-isolines and simultaneously to the diminishing standing eddy circulation patterns, a positive circulation pattern emerges in the surface layer around $y = 350$km for a contour-depth of $z = -325$m and increases significantly in magnitude for deeper contour-depths (Fig. 3.7 e,f)). Consequently, the determination of the contour-depth which leads to the minimal overall standing eddy circulation $\hat{\psi}_I^*$ is not as straightforward as for zonal integration along $\overline{p}/f_0$-isolines. We choose the criterion, that the standing eddy circulation $\hat{\psi}_I^*$ with the smallest maximal absolute value represents the minimal overall standing eddy circulation $\hat{\psi}_I^*$. In our experiments, the corresponding contour-depth lies around $z = -500$m.

Figure 3.7 also shows the corresponding Eulerian streamfunctions $\overline{\Lambda}_I$ of the hill case, where zonal integration is performed along horizontal isolines of either $\overline{p}/f_0$ or $\overline{b}$ at three selected contour-depths (so that $\overline{\Lambda}_I + \hat{\psi}_I^*$ represents the overall time-mean circulation). In both cases, the structure of two local maxima (see Fig. 3.1 b)) is lost, but now only one local maximum is situated in the center of the circulation cell, i.e. around the top of topography and around $y = -700$km (except in Fig. 3.7 i), where the maximum is close to the surface layer). In addition, the magnitude of the maximal values is generally reduced. Remember that if time-mean horizontal streamlines coincided with time-mean geostrophic streamlines and were depth-independent, we would not only expect $\hat{\psi}_I^* \equiv 0$, but also $\overline{\Lambda}_I \equiv 0$ (for zonal integration along time-mean geostrophic streamlines). Accordingly, for $\overline{p}/f_0$-isolines the overall magnitude of $\overline{\Lambda}_I$ is always smaller than $\overline{\Lambda}_I$ using $\overline{b}$-isolines at the same depth. However, for zonal integration along $\overline{p}/f_0$-isolines the dependency of the contour-depth of $\overline{\Lambda}_I$ and the standing eddy circulation $\hat{\psi}_I^*$ counteract each other: While the overall standing eddy circulation $\hat{\psi}_I^*$ intensifies, the overall Eulerian circulation $\overline{\Lambda}_I$ diminishes with deeper contour-depths. A different behaviour is present using $\overline{b}$-isolines: Here the minimal overall Eulerian circulation $\overline{\Lambda}_I$ and the minimal overall standing eddy circulation $\hat{\psi}_I^*$ are found for the same contour-depth, i.e. in our model experiments around the mid-depth of $z = -500$m. For both shallower contour-depths (more pronounced negative values in the standing eddy circulation $\hat{\psi}_I^*$) and deeper contour-depths (more pronounced positive

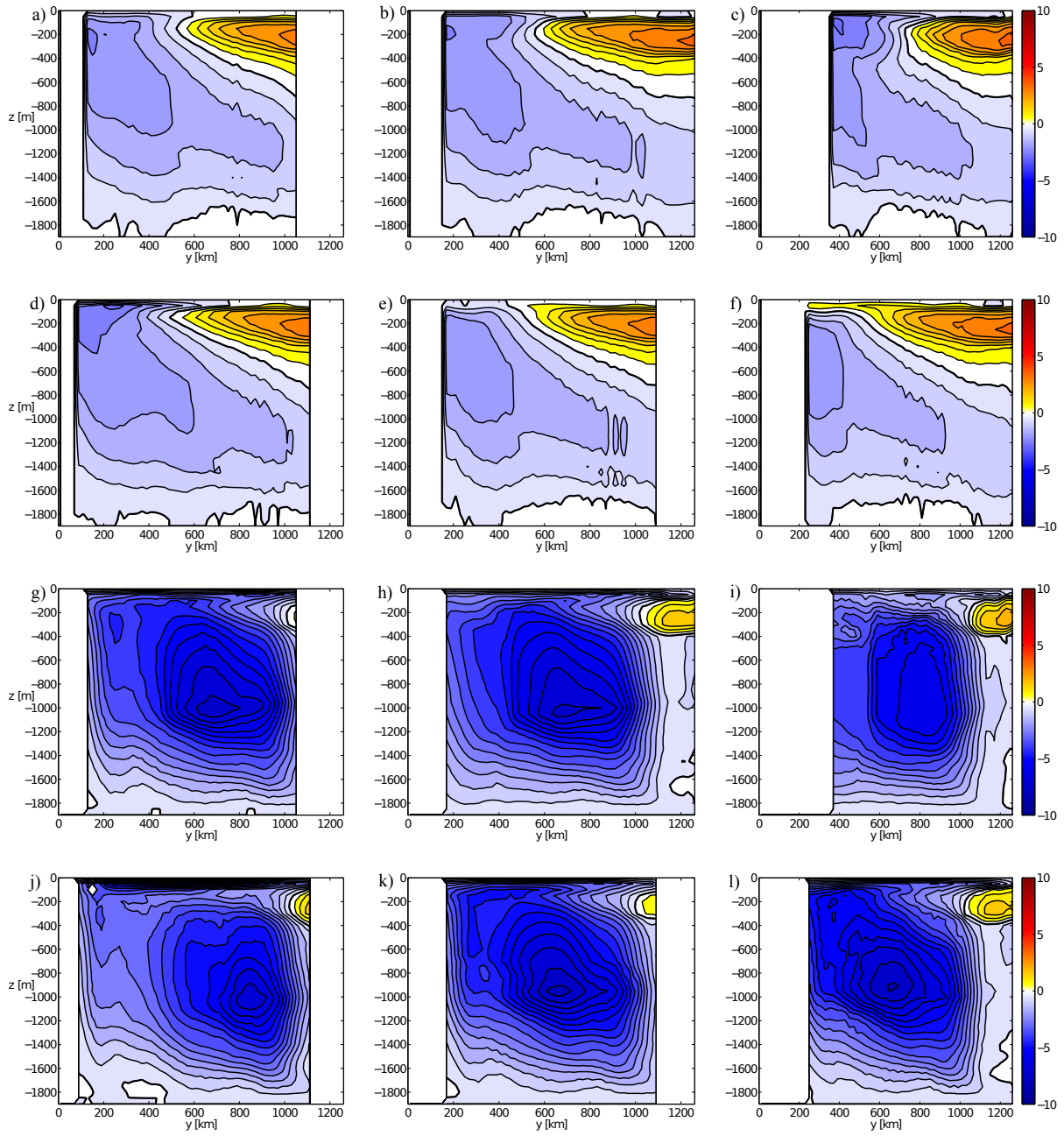

Figure 3.8: Isopycnal streamfunctions $\overline{\psi_I}$ for zonal integration along time-mean geostrophic streamlines (a-c) and isolines of time-mean buoyancy $\overline{b}$ (d-f). Transient eddy streamfunctions $\tilde{\psi}_I^*$ for zonal integration along time-mean geostrophic streamlines (g-i) and isolines of time-mean buoyancy $\overline{b}$ (j-l). From left to right the contour-depths are given by $z = -25$m, $z = -475$m and $z = -925$m.

values in the standing eddy circulation $\hat{\psi}_I^*$) $\overline{\Lambda}_I$ increases.

Finally, Figure 3.8 shows the corresponding total isopycnal streamfunctions $\overline{\psi_I}$ and transient eddy streamfunctions $\tilde{\psi}_I^*$ of the hill case. In the ocean interior, both the positive and the negative overturning cells are roughly equivalent in all cases, while in the surface layer qualitative differences occur for different contour-depths (Fig. 3.8 a-f)). As suggested by several studies, for zonal integration along surface $\overline{p}/f_0$-isolines (Fig. 3.8 a)), the shallower positive MOC is in accordance with the surface wind forcing conditions. The negative overturning cell is more restricted to the south in the surface layer and its overall magnitude is reduced, while the overall magnitude of the positive cell is essentially unchanged (compare with Fig. 3.2 d)). However, for deeper contour-depths of the time-mean geostrophic streamlines both the magnitude and the meridional extension in the surface layer of the negative overturning cell increase, such that the northward surface return flow of the positive overturning cell (whose overall magnitude remains unaltered) is more and more covered by the negative cell (Fig. 3.8 b,c)). This tendency is in correspondence with the dependency of the contour-depth of the respective standing eddy streamfunctions $\hat{\psi}_I^*$ (Fig. 3.7 a-c)), where the negative surface circulation significantly increases with deeper contour-depths. In particular, the magnitude of the corresponding negative transient eddy circulation $\tilde{\psi}_I^*$ in the surface layer decreases with deeper contour-depths (Fig. 3.7 g-i)), such that for a contour-depth of $z = -925$m the negative surface circulation in the total MOC $\overline{\psi_I}$ (Fig. 3.8 c)) is entirely due to the negative surface standing eddy circulation $\hat{\psi}_I^*$ (similar to the case of zonal integration along latitude circles, Fig. 3.4 b,d)).

Using horizontal $\overline{b}$-isolines as zonal integration paths, the overall magnitude of the positive overturning cell of the total isopycnal streamfunctions $\overline{\psi_I}$ also appears to be insensitive to changes in the contour-depth. However, the dependency of the contour-depth of the magnitude and the meridional extension in the surface layer of the negative overturning cell is opposite to the previous case: With deeper contour-depths the magnitude and the meridional extension in the surface layer of the negative overturning cell reduce (Fig. 3.8 d-f)). In case of the deep contour-depth $z = -925$m, the positive overturning cell even overflows the negative overturning cell in the entire SO (Fig. 3.8 f)). Obviously, since the negative transient eddy circulation $\tilde{\psi}_I^*$ in the surface layer only slightly decreases with deeper contour-depths (Fig. 3.7 j-l)), this behaviour is related to the emergence of a positive circulation pattern in the surface layer of the standing eddy streamfunction $\hat{\psi}_I^*$ (Fig. 3.7 f)). Nevertheless, the contour-depth which leads to the most appropriate surface circulation pattern (regarding the wind forcing) is found around the mid-depth of $z = -500$m (Fig. 3.8 e)). Hence, we obtain the important result that in both cases (zonal integration

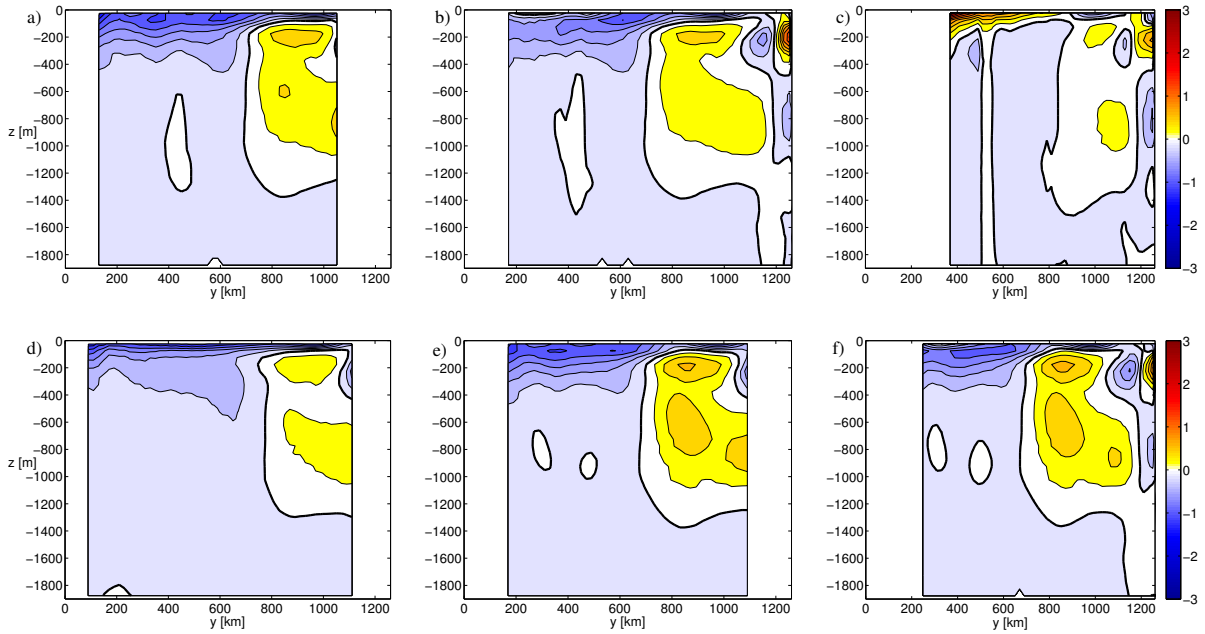

Figure 3.9: The difference (multiplied by 10^3) between the time-mean of the isopycnally and along time-mean contours averaged buoyancy distribution and the isopycnally and along latitude circles averaged buoyancy distribution. Contours are either time-mean geostrophic streamlines (a-c) or isolines of time-mean buoyancy (d-f). From left to right the contour-depths are given by $z = -25$m, $z = -475$m and $z = -925$m. The contour interval (of the plots) is $0.2m/s^2$ and zero lines are thick.

along time-mean geostrophic streamlines or isolines of buoyancy) the most appropriate surface circulation pattern and the minimal standing eddy circulation are related to the same contour-depth.

Related zonal-mean buoyancy distributions

Each of the above isopycnal streamfunctions (Fig. 3.8 a-f)) advects a different isopycnally averaged buoyancy (McDougall and McIntosh, 2001; Nurser and Lee, 2004a), corresponding to the zonal integration path. Per definition, each curvilinear zonal integration path with an equivalent coordinate y, although being longer, encompasses the same amount of area to the south as the latitude circle related to the latitude y. However, the zonal-mean buoyancy distribution is sensitive to the zonal integration paths. Similar to Fig. 3.3 b), the differences (not shown) between the isopycnally and along time-mean contours averaged buoyancy distributions (not shown) and the Eulerian mean buoyancy distribution averaged

along latitude circles (shown in Fig. 3.1 d)) are maximal and positive in the surface layer in each case. Figure 3.9 shows the differences between the isopycnally and along time-mean contours averaged buoyancy distributions and the isopycnally and along latitude circles averaged buoyancy distribution (not shown), which partly show significant values below the surface layer at mid-depth. The differences of Fig. 3.9 are of the same order of magnitude as those of Fig. 3.3 b). In other words, the effect of changing the zonal integration paths is of the same order as changing between Eulerian and isopycnal averaging. Fig. 3.9 and Fig. 3.6 suggest the following relation between zonal integration paths and the corresponding isopycnally averaged buoyancy distributions in our experiments: As long as the zonal integration paths roughly follow $\overline{b}$-isolines, being more northward above topography than above flat bottom (see Fig. 3.6 a,d-f)), the corresponding zonal-mean buoyancy distributions are colder in the surface layer than the zonal-mean buoyancy distribution resulting from zonal integration along latitude circles (Fig. 3.9 a,b,d-f)). Using $\overline{p}/f_0$-isolines (Fig. 3.9 a-c)), the surface layer values of the zonal-mean buoyancy distributions increase with deeper contour-depths, even exceeding, for the deepest set of contours, the values of the case of zonal integration along latitude circles. This is due to the development of a broad recirculation pattern in the geostrophic streamlines with deeper depths (see Fig. 3.6 a-c)), which "pushes" the geostrophic streamlines above flat bottom to the north. At larger depth, $\overline{p}/f_0$-isolines are more northward above flat bottom than above topography, in opposition to $\overline{b}$-isolines.

3.6 Summary

The zonal-mean isopycnal meridional streamfunction $\psi_I(y, b_a, t)$ (Eq. (3.5)) is the southward volume transport with buoyancy b smaller than a given value b_a across a given latitude y. In this case, the zonal integration is performed along latitude circles. Since the integration condition of ψ_I shows zonal and temporal dependencies, its time-mean $\overline{\psi_I}$ (Eq. (3.6)) includes deviations from the time- and zonal-means of both b and the meridional transport velocity v. In order to distinguish the relative impacts of the means and deviations of b and v, we decomposed the total isopycnal MOC $\overline{\psi_I}$ into three parts: (i) The Eulerian MOC $\overline{\Lambda}_I$ (Eq. (3.7)) is defined by the time- and zonal-means of b and v and may be considered as the classical Eulerian MOC (Eq. (3.4)) in isopycnal coordinates, if the time- and zonal-mean buoyancy distribution $[\overline{b}]$ is vertically monotonic. (ii) The isopycnal standing eddy MOC $\hat{\psi}_I^*$ (Eq. (3.8)) is defined by the difference between, on the one hand, the part of $\overline{\psi_I}$ which

is defined by the time-means of b and v and, on the other hand, the Eulerian MOC $\overline{\Lambda}_I$. (*iii*) The transient eddy MOC $\tilde{\psi}_I^*$ (Eq. (3.9)) of $\overline{\psi_I}$ is given by the residuum.

We applied the decomposition of $\overline{\psi_I}$ to the results of an eddy-permitting idealised numerical SO model in a configuration with a simple hill-like topographic feature. Expectedly, $\overline{\psi_I}$ shows a positive cell, which connects the SO and the Atlantic, and a negative cell related to bottom water formation. However, $\overline{\psi_I}$ exhibits a southward surface flow in the entire SO, which conflicts with the expectation of a northward wind-driven Ekman transport. The decomposition of $\overline{\psi_I}$ reveals that the standing eddy MOC $\hat{\psi}_I^*$ constitutes the southward surface transport of $\overline{\psi_I}$ in the SO.

Previous studies (e.g. Treguier et al. (2007)) suggest that a redefinition of the zonal integration paths, such that the standing eddy MOC $\hat{\psi}_I^*$ vanishes in the SO, may lead to a more appropriate MOC $\overline{\psi_I}$. In the key chapter of this study (section 3.5.2), we considered two types of zonal integration paths, which enable the reduction or even vanishing of the standing eddy MOC $\hat{\psi}_I^*$: time-mean horizontal streamlines and horizontal isolines of time-mean buoyancy $\overline{b}$.

It turned out that time-mean horizontal streamlines represent the more limited and complicated case. Exact time-mean horizontal streamlines may be used as zonal integration paths in the construction of a zonal-mean meridional streamfunction only, in case they are closed above topography (i.e. the horizontal velocity field is nondivergent), because otherwise mass balance is not guaranteed. We showed that if time-mean horizontal streamlines are both closed and depth-independent, the time-mean of the meridional cross-streamline transport velocity will vanish. It follows that under such conditions both the standing eddy MOC $\hat{\psi}_I^*$ *and* the Eulerian MOC $\overline{\Lambda}_I$ vanish exactly. However, as demonstrated by the model results of the hill case, time-mean horizontal streamlines generally are unclosed in the surface layer (due to the wind-driven Ekman transport) and significantly change with depth. Consequently, zonal integration along time-mean horizontal geostrophic streamlines may only lead to a reduction, but not an exact vanishing of the standing eddy MOC $\hat{\psi}_I^*$: On the one hand, streamlines have to be approximated by the isolines of a scalar field, e.g. the geostrophic streamfunction $\overline{p}/f_0$, such that in regions of dominant ageostrophic transports a significant standing eddy MOC $\hat{\psi}_I^*$ may appear. On the other hand, the significant depth-dependence of the (geostrophic) streamlines induces a non-orthogonality term with non-vanishing time-mean in the meridional cross-streamline transport velocity, which may lead to an additional significant contribution in the standing eddy MOC $\hat{\psi}_I^*$.

In case horizontal isolines of time-mean buoyancy $\overline{b}$ are adopted as the zonal coordinate

lines, the standing eddy component $\overline{b}^{+}$ vanishes and the circumstances are more promising and simple. On the one hand, $\overline{b}$-isolines are always closed above topography and hence do not conflict with mass balance and may be used without approximation. On the other hand, a vanishing standing eddy MOC $\hat{\psi}_I^*$ relies only on the integration conditions. It is independent of the determination of the cross-path transport velocity and therefore always exactly holds - even for a depth-dependent $\overline{b}$, which induces a non-orthogonal curvilinear coordinate system. However, the time-mean of the cross-path transport velocity and hence the Eulerian MOC $\overline{\Lambda}_I$ do not vanish in general.

In order to avoid the considerable technical complications implied by non-orthogonal coordinates, we computed the total isopycnal MOC $\overline{\psi_I}$ by using either $\overline{b}$-isolines or $\overline{p}/f_0$-isolines of a fixed depth ("contour-depth"), such that the applied curvilinear coordinate system is orthogonal. For $\overline{b}$-isolines the standing eddy MOC $\hat{\psi}_I^*$ now exactly vanishes at the corresponding contour-depth only. For the same result, $\overline{p}/f_0$-isolines additionally have to coincide with the exact horizontal time-mean streamlines at the contour-depth, which excludes the surface Ekman layer.

By applying different contour-depths, we found that for $\overline{p}/f_0$-isolines the minimal standing eddy MOC $\hat{\psi}_I^*$ emerges for contour-depths near the surface, including a significant negative standing eddy circulation in the surface layer due to the missed surface Ekman transport. For deeper contour-depths, the standing eddy surface circulation increases in both negative magnitude and vertical extension. For $\overline{b}$-isolines, the minimal standing eddy MOC $\hat{\psi}_I^*$ is found for contour-depths around $z = -500$m in our experiment and is of slightly smaller magnitude than the minimal $\hat{\psi}_I^*$ resulting from zonal integration along $\overline{p}/f_0$-isolines. Using shallower (deeper) contour-depths leads to stronger negative (positive) standing eddy circulations for $\overline{b}$-isolines. For both types of zonal integration paths, the corresponding Eulerian MOCs $\overline{\Lambda}_I$ are in general smaller than $\overline{\Lambda}_I$ obtained by zonal integration along latitude circles, with $\overline{p}/f_0$-isolines giving the smallest $\overline{\Lambda}_I$ for a certain contour-depth. For $\overline{p}/f_0$-isolines, $\overline{\Lambda}_I$ decreases with deeper contour-depths (in opposition to $\hat{\psi}_I^*$), while in case of $\overline{b}$-isolines the minimal $\overline{\Lambda}_I$ and the minimal $\hat{\psi}_I^*$ appear at the same contour-depth.

The corresponding total MOCs $\overline{\psi_I}$ show significant differences in the surface layer. For both types of zonal integration paths, the most appropriate surface layer circulation is obtained by using the contour-depth of the minimal standing eddy circulation $\hat{\psi}_I^*$. The dependency of contour-depths of the surface layer circulation in $\overline{\psi_I}$ is dominated by the corresponding $\hat{\psi}_I^*$: For $\overline{p}/f_0$-isolines, the negative surface circulation extends with deeper

contour-depths, while for $\overline{b}$-isolines the negative (positive) surface circulation extends with shallower (deeper) contour-depths.

Finally, we considered the corresponding isopycnally averaged buoyancy distributions. Changing from Eulerian to isopycnal averaging for zonal integration along latitude circles primarily leads to a warmer surface layer. We found that the effect of changing from latitude circles to curvilinear zonal integration paths is slightly smaller, but of the same order. $\overline{b}$-isolines generally lead to a cooling in the surface layer, while $\overline{p}/f_0$-isolines, becoming more northward with depth, lead to a cooling (warming) for shallow (deep) contour-depths.

3.7 Conclusions

We make the following conclusions:

1. The construction of a zonal-mean meridional isopycnal streamfunction $\overline{\psi_I}$ (Eq. (3.6)) with an exactly vanishing standing eddy part $\hat{\psi}_I^*$ (Eq. (3.8)) has to be performed by zonal integration along depth-dependent horizontal isolines of time-mean buoyancy $\overline{b}$.

2. If zonal integration paths approximate time-mean streamlines, one has to expect in general that the standing eddy part $\hat{\psi}_I^*$ is only reduced, i.e. $\hat{\psi}_I^*$ remains a constitutive part of the total MOC $\overline{\psi_I}$. First of all, because the significant ageostrophic transport in the surface layer is missed. Moreover, depth-dependent streamlines induce a term with non-vanishing time-mean in the meridional transport velocity, which is related to the vertical velocity and the vertical variation of the zonal integration paths ("non-orthogonality term").

3. If $\overline{b}$- or $\overline{p}$-contours of a certain depth ("contour-depth") are used at each depth, the standing eddy part $\hat{\psi}_I^*$ vanishes exactly only at the contour-depth (except the surface layer for $\overline{p}$). But, for adequate contour-depths, the overall standing eddy part $\hat{\psi}_I^*$ is significantly reduced (but not vanishing). For our model results, contours at mid-depth (in surface layer) are most appropriate for $\overline{b}$ (for $\overline{p}$). Hence, if a reduced standing eddy part $\hat{\psi}_I^*$ is sufficient, this approach represents a practical simplification ("orthogonal coordinates").

4. Regarding the zonally averaged buoyancy distribution in our model results, the effect of changing from latitude circles to curvilinear zonal integration paths is of the same

order as changing from Eulerian to isopycnal averaging (for zonal integration along latitude circles).

3.8 Appendix

3.8.1 General horizontal zonal integration paths

In order to consider general horizontal zonal integration paths, we have to turn to *curvilinear coordinates* $(m, n, \tilde{z})$ (see e.g. Aris (1989)). More precisely, we introduce a coordinate transformation[10] (where the Cartesian coordinates are denoted by (x, y, z)),

$$x = x(m, n, \tilde{z}) \ , \qquad y = y(m, n, \tilde{z}) \ , \qquad z = \tilde{z} \ , \tag{3.13}$$

$$m = m(x, y, z) \ , \qquad n = n(x, y, z) \ , \qquad \tilde{z} = z \ , \tag{3.14}$$

such that the coordinate lines of m represent the new zonal integration paths. In our context, n is defined via the contours of either $\overline{b}$ or $\overline{p}$.

A set of Cartesian base vectors tangent to the new coordinate lines is given by

$$\mathbf{g}_m = (\partial_m x, \partial_m y, 0) \ , \qquad \mathbf{g}_n = (\partial_n x, \partial_n y, 0) \ , \qquad \mathbf{g}_{\tilde{z}} = (\partial_{\tilde{z}} x, \partial_{\tilde{z}} y, 1) \ , \tag{3.15}$$

such that the covariant metric tensor g_{ij}, $i, j = m, n, \tilde{z}$, is given by the scalar products of these base vectors (e.g. $g_{mn} = \mathbf{g}_m \cdot \mathbf{g}_n$), and a basis of unit vectors tangent to the curvilinear coordinate lines is given by $\mathbf{e}_m = \mathbf{g}_m / \sqrt{g_{mm}}$, $\mathbf{e}_n = \mathbf{g}_n / \sqrt{g_{nn}}$, $\mathbf{e}_{\tilde{z}} = \mathbf{g}_{\tilde{z}} / \sqrt{g_{\tilde{z}\tilde{z}}}$. Since we permit $\partial_{\tilde{z}} x \neq 0$ and $\partial_{\tilde{z}} y \neq 0$ to hold, the curvilinear coordinate system is generally non-orthogonal. However, we choose m such that the curvilinear coordinate system is horizontally orthogonal ($\mathbf{e}_m \cdot \mathbf{e}_n = 0$), and hence $\mathbf{e}_n = (\nabla_h n / |\nabla_h n|, 0)$ and $\mathbf{e}_m = (\nabla_h m / |\nabla_h m|, 0)$ hold[11].

The velocity vector $\mathbf{v}$ may be expressed in this system of base vectors, $\mathbf{v} = u^m \mathbf{g}_m + v^n \mathbf{g}_n + w^{\tilde{z}} \mathbf{g}_{\tilde{z}}$, where the coefficients are the contravariant components of the velocity vector $\mathbf{v}$ in the given coordinate system. These components are related to the corresponding components of the velocity vector $\mathbf{v}$ in Cartesian coordinates, $\mathbf{v} = u\mathbf{e}_x + v\mathbf{e}_y + w\mathbf{e}_z$, via $(u^m, v^n, w^{\tilde{z}}) = (\nabla m \cdot \mathbf{v}, \nabla n \cdot \mathbf{v}, w)$.

[10] That is, the corresponding Jacobian exists and does not vanish at each point of our domain of definition.

[11] ∇_h denotes the horizontal gradient $\nabla_h \equiv (\partial_x, \partial_y)$. In our context, a function m, which satisfies $\mathbf{e}_m \cdot \mathbf{e}_n = 0$, generally may be constructed via the integral curves of the normal vector field $\nabla_h n$, in case $\partial_y n > 0$ at each point.

Finally, the zonal mean (at fixed depth) of any scalar quantity q is given via the line integrals along the coordinate lines of m (denoted by C_n),

$$[q](n) = \int_{C_n} q \; ds = \int_a^b q(x_n(m), y_n(m)) \; \sqrt{g_{mm}} \; dm \; , \tag{3.16}$$

where, for fixed n, $(x_n(m), y_n(m)) \equiv (x(m,n), y(m,n))$ is regular parameterisation of C_n. We transform each zonal-mean quantity $[q](n)$ to equivalent y-coordinates via areal integration (Tansley and Marshall, 2001): The equivalent y-coordinate of a coordinate line C_n is given by the latitude y that encompasses an equivalent area to the south.

3.8.2 No-normal-flow boundary condition in curvilinear coordinates and condition (ii) of section 3.5.2

We adopt the general framework of appendix 3.8.1. Let $m_{\mathcal{B}}(n, \tilde{z})$ describe a zonal topographic or continental barrier in the curvilinear coordinates $(m, n, \tilde{z})$. Then a normal vector $\mathbf{N}$ of the barrier is given by $\mathbf{N} = \mathbf{g}_m - (\partial_n m_{\mathcal{B}})\mathbf{g}_n - (\partial_{\tilde{z}} m_{\mathcal{B}})\mathbf{g}_{\tilde{z}}$. Consequently, the condition of vanishing cross-barrier velocity is given in curvilinear coordinates by

$$\begin{aligned} 0 \; &\stackrel{!}{=} \; \mathbf{N} \cdot \mathbf{v}|_{m_{\mathcal{B}}} \\ &= \; (u^m g_{mm} - v^n g_{nn} \partial_n m_{\mathcal{B}} - w g_{\tilde{z}\tilde{z}} \partial_{\tilde{z}} m_{\mathcal{B}} - 2u^m g_{m\tilde{z}} \partial_{\tilde{z}} m_{\mathcal{B}} - 2v^n g_{n\tilde{z}} \partial_{\tilde{z}} m_{\mathcal{B}})|_{m_{\mathcal{B}}} \; . \end{aligned} \tag{3.17}$$

Notice that the last two terms in Eq. (3.17) are due to the non-orthogonality of the curvilinear coordinate system. In contrast, the Leibniz integral rule applies in the same form as for Cartesian coordinates, e.g.

$$\partial_n \int_m^{m_{\mathcal{B}}} \left(\sqrt{g} \; v^n \right) \; dm' = \int_m^{m_{\mathcal{B}}} \partial_n \left(\sqrt{g} \; v^n \right) \; dm' + \left(\sqrt{g} \; v^n \right)|_{m_{\mathcal{B}}} \partial_n m_{\mathcal{B}} \; . \tag{3.18}$$

In order to satisfy condition (ii) of section 3.5.2 the corresponding boundary terms of Eq. (3.17) and Eq. (3.18) have to cancel each other (or vanish on their own). E.g. in case of orthogonal coordinates it would have to hold $g_{mm} = g_{nn} = g_{\tilde{z}\tilde{z}}$. Consequently, Cartesian coordinates represent the only familiar coordinate system, where condition (ii) is always exactly satisfied by solely imposing the boundary condition of no-normal-flow at topographic barriers. Therefore, both types of zonal integration paths, horizontal time-mean buoyancy contours and time-mean (geostrophic) streamlines, do not necessarily satisfy condition (ii), but further boundary conditions have to be included. For example, in case the

no-slip boundary condition is additionally applied (as in our experiments), i.e. the velocity $\mathbf{v}$ vanishes at topographic boundaries, the boundary terms in Eq. (3.17) and Eq. (3.18) vanish on their own.

3.8.3 The isopycnal streamfunction defined in isopycnal coordinates

The coordinate transformation to isopycnal coordinates represents the type of coordinate transformations, which leave the horizontal coordinates unchanged, but alter the vertical coordinate. In contrast to appendix 3.8.1, we have

$$x = \tilde{x} \ , \qquad y \ = \ \tilde{y} \ , \qquad z = z(\tilde{x}, \tilde{y}, b) \ , \qquad b = b(x, y, z) \ . \tag{3.19}$$

The properties of a coordinate transformation imply $\partial_b z = 1/\partial_z b \equiv \sigma$, $\partial_{\tilde{x}} z = -\partial_x b/\partial_z b \equiv s_x$ and $\partial_{\tilde{y}} z = -\partial_y b/\partial_z b \equiv s_y$, where we introduced the thickness σ and the zonal and meridional isopycnal slopes s_x and s_y.

The Cartesian base vectors tangent to the new coordinate lines are now given by

$$\mathbf{g}_{\tilde{x}} = (1, 0, s_x) \ , \qquad \mathbf{g}_{\tilde{y}} = (0, 1, s_y) \ , \qquad \mathbf{g}_b = (0, 0, \sigma) \ , \tag{3.20}$$

and hence the coordinate transformation is fully non-orthogonal, i.e. the elements of the covariant metric tensor g_{ij} are all non-vanishing. Nevertheless, we have[12] $g \equiv det(g_{ij}) = \sigma^2$. The contravariant components of the velocity vector, $\mathbf{v} = u^{\tilde{x}}\mathbf{g}_{\tilde{x}} + v^{\tilde{y}}\mathbf{g}_{\tilde{y}} + w^b\mathbf{g}_b$, are now related to the corresponding components of the velocity vector in Cartesian coordinates, $\mathbf{v} = u\mathbf{e}_x + v\mathbf{e}_y + w\mathbf{e}_z$, via $(u^{\tilde{x}}, v^{\tilde{y}}, w^b) = (u, v, \nabla b \cdot \mathbf{v})$. Consequently, we obtain for the continuity equation, $\nabla \cdot \mathbf{v} = 0$, in isopycnal coordinates (see Eq. 3.11)

$$\frac{1}{\sigma}\left[\partial_{\tilde{x}}\Big(\sigma \ u\Big) + \partial_{\tilde{y}}\Big(\sigma \ v\Big) + \partial_b\Big(\sigma \ w^b\Big)\right] = 0 \ , \tag{3.21}$$

where $\sigma w^b = \sigma(\nabla b \cdot \mathbf{v}) = -s_x u - s_y v + w$. For steady state conditions (assumed so far), the buoyancy budget reads $\mathbf{v} \cdot \nabla b = Q_b$ and hence we obtain the so-called thickness equation

$$\partial_{\tilde{x}}\Big(\sigma \ u\Big) + \partial_{\tilde{y}}\Big(\sigma \ v\Big) + \partial_b\Big(\sigma \ Q_b\Big) = 0 \ . \tag{3.22}$$

[12] Hence, σ is the Jacobian. Of course, $\sigma \neq 0$ has to hold everywhere.

Zonal integration along a closed path (with fixed $\tilde{y}$ and b) gives

$$\partial_{\tilde{y}}\left(L_x^{-1}[\sigma v]\right) + \partial_b\left(L_x^{-1}[\sigma Q_b]\right) = 0 \ . \tag{3.23}$$

Consequently, the transport function

$$\Psi_I(\tilde{y}, b_a) \equiv -\int_0^{b_a} L_x^{-1}[\sigma v]\ db = -\int_0^{b_a} \oint v\ \sigma d\tilde{x} db \tag{3.24}$$

is a streamfunction, i.e. $\partial_b \Psi_I = -L_x^{-1}[\sigma v]$ and $\partial_{\tilde{y}} \Psi_I = L_x^{-1}[\sigma Q_b]$.

However, the condition $\sigma \neq 0$ implies that isopycnal coordinates are possible only in case of a strictly vertically monotonic density distribution. Then Ψ_I is identical to ψ_I (Eq. 3.5).

4 Residual-mean eddy streamfunction and quasi-Stokes streamfunction

This chapter will be submitted as an article to Ocean Modelling.

4.1 Abstract

Using several idealised eddy-permitting zonal channel model experiments, the series expansion of the residual-mean eddy streamfunction and the quasi-Stokes streamfunction are compared up to third order in buoyancy perturbation. In model configurations with flat bottom, both streamfunctions may be well approximated by the first one or two leading order terms in the ocean interior, although terms up to third order still significantly impact the implied interior circulations. Further, differences in both series expansions up to third order remain small here. Near surface and bottom boundaries, on the other hand, the leading order terms differ and are initially of alternating sign and of increasing magnitude such that the low order approximate expressions break down there. In more realistic model configurations with significant topographic features, physically inconsistent recirculation cells also appear in the ocean interior and are not effectively reduced by the next higher order terms. A measure indicating an initially increasing or decreasing series expansion is proposed for practical use.

4.2 Introduction

Eulerian averaging of velocities and tracers is usually considered as the simplest way of averaging: Time and ensemble averages are performed at fixed position and space averages are solely defined by the geometrical framework (i.e. by the coordinate lines of the geometrically natural coordinate system). From a practical point of view, Eulerian averaging appears to be the most straightforward averaging procedure, because the physical proper-

ties of the fluid are not taken into account (Andrews and McIntyre, 1978a). Accordingly, the Eulerian meridional transport streamfunction Λ, i.e. the zonally integrated meridional transport of fluid across a given latitude y and below a constant height surface z, is defined in regard to the space coordinates y and z.

However, Λ gives rise to spurious diabatic circulations such as the Deacon cell (Döös and Webb, 1994). In an isopycnal averaging framework (Nurser and Lee, 2004a), the Deacon cell is reduced and therefore the isopycnal meridional transport streamfunction, i.e. the zonally integrated meridional transport of fluid across a given y and denser than a given density, is considered as a more appropriate description of the meridional overturning circulation (MOC). In order to obtain a physically meaningful MOC in the Eulerian framework, the initial simplification (i.e. the insensitivity to the physical state of the fluid) has to be revised and a more complicated redefinition of the total overturning streamfunction has to be introduced. More precisely, two different approaches of constructing physically more satisfying overturning streamfunctions in the Eulerian framework have been put forward: the residual-mean theory (Andrews and McIntyre, 1976; Eden et al., 2007) and the quasi-Stokes streamfunction Ψ^* (McDougall and McIntosh, 2001; Nurser and Lee, 2004b).

The residual streamfunction ψ_{res} is defined as the streamfunction which advects the Eulerian-mean buoyancy and it is constituted as the residual of two parts: On the one hand, the advection is due to the Eulerian-mean velocities (given by Λ), on the other hand, there is an eddy-induced streamfunction ψ^* due to the advective part of the eddy buoyancy flux. Physically, it is desired that, if there is no instantaneous diabatic buoyancy forcing, there should be also no diabatic effects in the Eulerian-mean buoyancy budget, i.e. the eddy-induced diabatic forcing should vanish too. Eden et al. (2007) (extending ideas of McDougall and McIntosh (1996); Medvedev and Greatbatch (2004)) demonstrate, by explicitly incorporating rotational eddy fluxes, that this physical criterion uniquely sets ψ^* and with it ψ_{res}. However, ψ^* is then given by a series involving fluxes of eddy buoyancy moments.

The quasi-Stokes streamfunction Ψ^* is the eddy-induced component of the total isopycnal streamfunction expressed in Eulerian space (McDougall and McIntosh, 2001; Nurser and Lee, 2004b). That is, the isopycnal streamfunction in Eulerian space may be given by the sum of Λ and Ψ^* and advects the isopycnally averaged buoyancy[1]. McDougall and McIntosh (2001) (see also Nurser and Lee (2004b)) apply a Taylor series analysis centerd around the mean height of isopycnals in order to express Ψ^* by Eulerian-mean quantities.

[1] The isopycnally averaged buoyancy is defined as inverse function of the mean height of isopycnals (McDougall and McIntosh, 2001; Nurser and Lee, 2004a).

Consequently, Ψ^* is given in two ways: On the one hand, it may be computed out of an isopycnal averaging framework. On the other hand, Ψ^* may be given directly in Eulerian space (i.e. in height coordinates) and is then expressed by a series expansion. Of course, this series expansion is different to the one of the residual-mean eddy streamfunction ψ^*, however, both are intimately connected as we discuss in this study.

Hence, if physically meaningful streamfunctions of the MOC are sought directly in the Eulerian framework, it seems that the appearance of series expansions generally represents a necessary and severe complication. Most problematic is that, practically, it is inevitable to cut off the series expansions at a certain order and hence one is left with approximate formulas. Typically, in a zonal-mean framework the first order terms of both series expansions are considered as good approximations in the nearly adiabatic ocean interior, but near horizontal boundaries (surface, bottom) the approximate formulas are found to break down, i.e. unphysical nonzero (and relatively large) values appear at the horizontal boundaries (Killworth, 2001; McDougall and McIntosh, 2001; Nurser and Lee, 2004b). A physically satisfactory solution of this serious problem is outstanding. In this study, this problem will be further explicated.

The subjects of this study are the following: We formally compare the first three orders of the series expansions of ψ^* and Ψ^* in order to specify the essential differences between these two intimately linked streamfunctions at low orders. Furthermore, we consider all terms up to the third order of both series expansions in different idealised models of the Southern Ocean (SO) in order to investigate the behaviour of both series expansions in different concrete model setups. It will turn out that, in a zonal-mean framework, the problems due to the convergence behaviour of both series expansions are more severe and hence the limitations of both approaches are stronger than discussed so far. Finally, we propose a measure to diagnose regions in the ocean where approximations of the series expansions break down.

The study is structured as follows: In section 4.3 we present our different model setups and experiments. In section 4.4 we consider the series expansion of the residual-mean eddy streamfunction ψ^*, while in section 4.5 we turn to the Taylor series of the quasi-Stokes streamfunction Ψ^*. Finally, section 4.6 provides a summary and discussion.

4.3 Models and experiments

In this study we use the code of CPFLAME[2] in two different configurations. The first configuration is largely a reproduction of the model setup considered in the study of Nurser and Lee (2004a,b), who used an idealised eddy-permitting zonal channel model in order to compare the isopycnal transport streamfunction with the quasi-Stokes first order approximation given by Eulerian-mean quantities. In our version, the primitive equations are formulated in Cartesian coordinates. The zonally reentrant channel extends over $L_x = 600$km in zonal direction and $L_y = 1000$km in meridional direction with 10km horizontal resolution. It is 1000m deep with 20m vertical resolution. The beta-plane approximation is used with a reference latitude situated at 49.31°S, such that at the center of the channel the Coriolis parameter becomes the one at 45°S for spherical coordinates. We simulate only buoyancy b in the model, which might be thought as proportional to temperature. The model is not forced with winds, but the circulation in the model is driven by three buoyancy restoring regions: At the surface, b is relaxed towards a target buoyancy varying linearly between $21.764 \times 10^{-3}\text{ms}^{-2}$ at $y = 95$km and $45.269 \times 10^{-3}\text{ms}^{-2}$ at $y = 905$km with a restoring time scale of 7 days. Within the southernmost 95km and the northernmost 95km, model buoyancies are relaxed throughout the water column to specified values: linearly varying with depth from $19.346 \times 10^{-3}\text{ms}^{-2}$ at the surface to zero at the bottom in the southern zone and from $48.365 \times 10^{-3}\text{ms}^{-2}$ to zero in the northern zone. The relaxation rate varies linearly between 1/(2 days) at the boundaries, and zero at the inner edges of the relaxation zone. Vertical viscosity is $5 \times 10^{-4}\text{m}^2\text{s}^{-1}$ and we use a horizontal biharmonic viscosity of $1.25 \times 10^{11}\text{m}^4\text{s}^{-1}$. The linear bottom friction parameter is $2 \times 10^{-5}\text{s}^{-1}$. Vertical diffusivity is $5 \times 10^{-5}\text{m}^2\text{s}^{-1}$, but we use no explicit lateral diffusion. The Quicker advection scheme is used as the advection scheme of buoyancy. The model was run for a total of 30 years. The diagnostics below are presented as temporal averages over the last 10 years of the run. We refer to this experiment as the *NL case*.

The second configuration is the idealised SO model setup introduced and discussed by Viebahn and Eden (2010, 2012), i.e. an eddy-permitting primitive equation model consisting of a zonally reentrant channel, which is connected to a northern ocean basin enclosed by land. The circulation in the model is driven by a sinusoidal westerly wind stress over the channel with a magnitude of $\tau = 1 \times 10^{-4} m^2 s^{-2}$, and a surface restoring boundary condition for buoyancy b (again, there is only buoyancy in the model). The corresponding target buoyancy increases northward over the channel, remains constant

[2] *http://www.ifm.zmaw.de/∼cpflame*

over the southern half of the northern ocean basin and decreases while approaching the northern end of the domain. Boundary conditions on the northern and southern edges of the domain are simply given by no-flux conditions. Hence, the watermass distribution is solely determined by the surface boundary conditions. The domain of the idealised model extends over $L = 2520$km in the zonal and meridional direction, with 20km horizontal resolution and 40 vertical levels with 50m thickness (1900m maximal water depth). The channel (i.e. the SO) extends from the southern boundary ($x = 0$km) to $x = L/2$. Further details may be found in Viebahn and Eden (2010, 2012). In particular, we consider the same two experiments already discussed by Viebahn and Eden (2012) in an isopycnal averaging framework. In the *flat case* experiment, the bottom is completely flat. In the *hill case* experiment, a simple hill-like topographic feature is imposed in the channel: The top of the hill is located at $z = -950$m and $x = 0$ (and $x = 2520$km respectively). According to an exponential map the height of the hill decreases eastward (westward), such that at the longitudes of the northern ocean basin (from $x = 850$km to $x = 1690$km) the channel has a flat bottom. In both experiments, the model has been run for 240 years. Additionally, we introduced harmonic viscosities, which act to damp EKE, in both experiments, in order to discuss the convergence behaviour of the series expansions of both ψ^* and Ψ^* subject to the "strength" of the eddy field. In the flat case, we introduced $A_h = 2000\text{m}^2\text{s}^{-1}$ and the model has been run for another 50 years, i.e. 290 years in total. In the hill case, we introduced $A_h = 2000\text{m}^2\text{s}^{-1}$, $A_h = 5000\text{m}^2\text{s}^{-1}$ and $A_h = 10000\text{m}^2\text{s}^{-1}$ respectively after 200 years of the initial model run and the model has been run for another 60 years, i.e. 260 years in total. In each experiment the time-mean is performed over the last 10 years.

In a way, the NL case represents the simplest model configuration in this study: Due to the lack of both zonal wind stress and the connection to a northern ocean basin, the time-zonal-mean meridional velocity $\overline{v}$ disappears almost completely in the NL case and hence it holds $\overline{\Lambda} \approx 0$, in contrast to the wind-driven flat case and the hill case experiments. Since $\overline{\Lambda}$ generally opposes the eddy-induced streamfunctions in the SO, the wind-driven model configuration shows eddy-induced streamfunctions of higher magnitudes at equal magnitudes of the overall overturning circulation.

4.4 Residual-mean framework

In a time-zonal-mean context, each quantity q generally may be decomposed into its temporal and zonal average $\overline{q}$ and its temporal and zonal deviation $q' \equiv q - \overline{q}$, i.e. $q = \overline{q} + q'$.

The time-zonal-mean residual streamfunction $\psi_{res}(y,z)$ is defined as the meridional streamfunction, which advects the Eulerian time-zonal-mean buoyancy $\overline{b}$. As outlined in appendix A, it is given by the sum of the time-zonal-mean Eulerian streamfunction $\overline{\Lambda}$ (defined by Eq. (4.14)) and the eddy streamfunction ψ^*,

$$\psi_{res} = \overline{\Lambda} + \psi^* \ . \tag{4.1}$$

A physically consistent determination of ψ^* (and with it ψ_{res}) was given by Eden et al. (2007) by explicitly incorporating rotational eddy fluxes (see appendix A for a synopsis). ψ^* is then given by a series involving fluxes of eddy buoyancy moments (see Eq. (4.22)),

$$\psi^* |\nabla \overline{b}| = -J_1 + \partial_m J_2 - \frac{1}{2}\partial_m^2 J_3 + O(b'^4) \ , \tag{4.2}$$

where $\partial_m() \equiv |\nabla\overline{b}|^{-1}\nabla\overline{b}\cdot\nabla|\nabla\overline{b}|^{-1}()$ and the $J_n \equiv \mathbf{F}_n \cdot \underset{\neg}{\nabla}\overline{b}|\nabla\overline{b}|^{-1}$ represent the along-isopycnal fluxes of the eddy buoyancy moments[3]. The terminology $O(b'^4)$ indicates additional terms that are of fourth or higher order in buoyancy perturbations. The orders of the series expansion (4.2) are defined solely by the fluxes of b'^n, i.e. via the order of the eddy buoyancy moment. The first order term in the expansion for ψ^* is identical to an eddy streamfunction of the transformed Eulerian mean (TEM) framework (Andrews and McIntyre, 1976, 1978b). The remainder of the expansion is due to the introduction of the rotational flux potential θ (see Eq. (4.23)). In the interior ocean, it typically holds $|\partial_y\overline{b}| \ll |\partial_z\overline{b}|$ and $|w| \ll |v|$ and we obtain

$$\psi^* \approx \frac{L_x\overline{v'b'}}{\partial_z\overline{b}} - \frac{1}{\partial_z\overline{b}}\partial_z\left(\frac{L_x\overline{\phi_2 v}}{\partial_z\overline{b}}\right) + \frac{1}{2}\frac{1}{\partial_z\overline{b}}\partial_z\left(\frac{1}{\partial_z\overline{b}}\partial_z\left(\frac{L_x\overline{\phi_3 v}}{\partial_z\overline{b}}\right)\right) + O(b'^4) \tag{4.3}$$

Now we consider the first three orders of the series expansion of the residual-mean eddy streamfunction ψ^* in our different model experiments. Notice that we calculated the terms as given by Eq. (4.2), but that differences to the terms as given by Eq. (4.3) are small in the entire model domain (including the diabatic boundary regions). In the following, we index the terms of the different orders of the series expansion of ψ^* by Roman numerals, i.e. $\psi^* = \psi^*_I + \psi^*_{II} + \psi^*_{III} + \psi^*_{IV} + ...$

[3] The eddy buoyancy moments are defined as $\phi_n = b'^n/n$ and the fluxes of the eddy buoyancy moments are given by $\mathbf{F}_n = L_x(\overline{v\phi_n}, \overline{w\phi_n})$, where n represents the order. The operator $\underset{\neg}{\nabla}$ is defined as $\underset{\neg}{\nabla} \equiv (-\partial_z, \partial_y)$. See appendix A for more details.

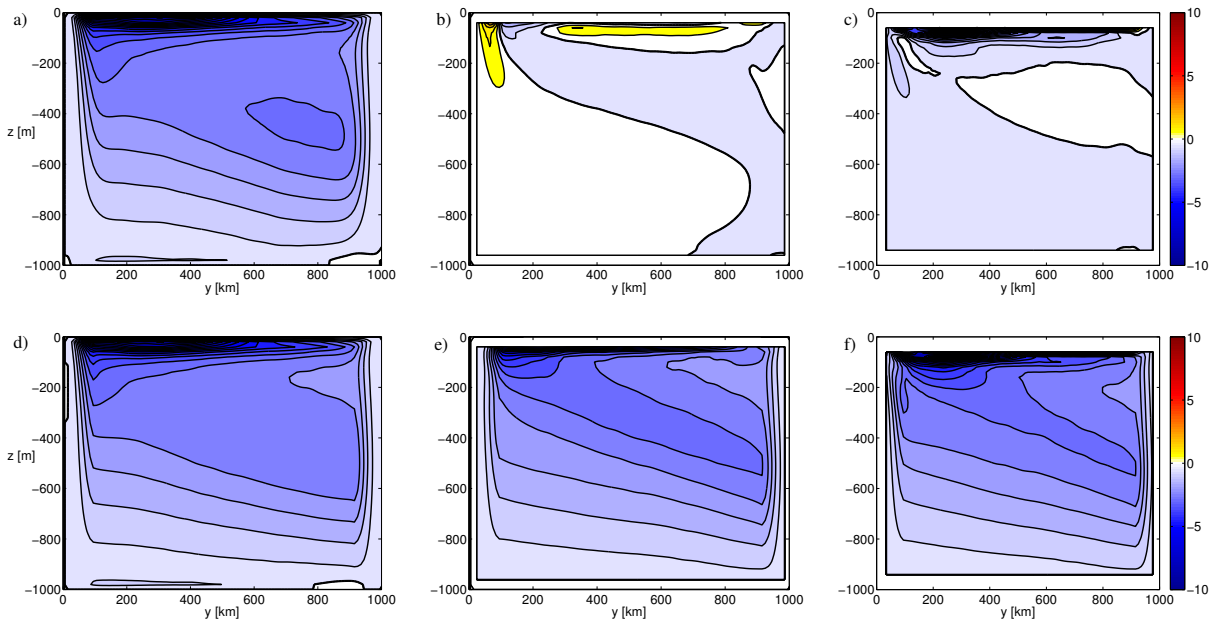

Figure 4.1: The first three terms of the series expansion of ψ^* for the NL case: $\psi^*_I \equiv -J_1/|\nabla\bar{b}|$ (a), $\psi^*_{II} \equiv \partial_m J_2/|\nabla\bar{b}|$ (b), $\psi^*_{III} \equiv -\frac{1}{2}\partial^2_m J_3/|\nabla\bar{b}|$ (c) and the corresponding residual streamfunctions including terms of ψ^* up to the first (d), second (e), third (f) order. The contour interval is 0.5Sv and zero lines are thick.

4.4.1 NL case

Fig. 4.1 a) shows the first term $\psi^*_I \equiv -J_1/|\nabla\bar{b}|$ of the series expansion of ψ^* (see Eq. (4.2)), i.e. the TEM eddy streamfunction, and Fig. 4.1 d) shows $\overline{\Lambda} + \psi^*_I$, i.e. the TEM residual MOC of the NL case. Since $\overline{\Lambda} \approx 0$ (not shown) due to the lack of zonal wind stress, both are largely identical, showing an anti-clockwise MOC with mainly along-isopycnal flow in the ocean interior and strong diapycnal flow in the three buoyancy restoring regions (but no bottom boundary layer). Only at mid-depth around $y = 750$km, the TEM residual MOC is slightly reduced in magnitude compared to ψ^*_I. However, physically inadequate is the extremely strong recirculation cell in the surface layer, which does not tend to zero at the surface (in Fig. 4.1 we simply set the surface values to zero).

Nurser and Lee (2004b) find a similar circulation pattern (see their Fig. 1). They discuss the unphysical surface circulation in the context of the classical TEM formalism, but the approaches of solving the problems at the boundaries by merging different eddy streamfunctions into each other are only partially successful and of unclear physical basis, hence remain unsatisfactory. In the physically logical approach of Eden et al. (2007), which

we adopt in this study (see appendix A for a synopsis), the problems at the boundaries are theoretically solved by incorporating the appropriate rotational eddy flux (given by Eq. (4.23)). However, since the appropriate rotational eddy flux is only given by a series expansion, the practical problem of including a sufficient number of terms of the series expansion in order to obtain an adequate approximation emerges.

Fig. 4.1 b,c) show the second term ψ^*_{II} and the third term ψ^*_{III} of the series expansion of ψ^*. In line with the expectation that ψ^*_I represents a good approximation of ψ^* in the nearly adiabatic ocean interior, the dominant values of the next higher order terms ψ^*_{II} and ψ^*_{III} are found in the surface diabatic boundary layer (for ψ^*_{IV} and ψ^*_V as well, not shown), although changes of the corresponding residual MOCs (Fig. 4.1 e,f)) are also visible in the ocean interior (compare also Fig. 4.1 d-f) with Fig. 4.6 a)). More precisely, ψ^*_{II} mainly opposes the surface layer circulation of ψ^*_I, while ψ^*_{III} amplifies it again. Hence, the series expansion (4.2) (or Eq. (4.23)) appears to be alternating, which is obvious in Fig. 4.1 a-c) and continued for the next higher order terms ψ^*_{IV} and ψ^*_V (not shown). This behaviour hampers the determination of an order at which the series expansion may be appropriately cut off, since the next higher order always compensates a part of the previous order. Moreover, it holds $|\psi^*_{II}| < |\psi^*_{III}|$ in the surface layer. More generally, the ratio $|\psi^*_i|/|\psi^*_I|$ (not shown) increases with increasing order i in the surface boundary layer, while it decreases in the ocean interior. That is, the magnitude of the terms of the series expansion (4.23) appears to be increasing in the diabatic surface region with increasing order, while a decreasing behaviour, which is found in the ocean interior, is necessary for an adequate approximation of ψ^* by low order terms.

We conclude: In the NL case, the series expansion of ψ^* may be adequately approximated by low order terms in the ocean interior, since there they appear to be decreasing with higher order - ψ^*_I alone already may seem sufficient (but notice section 4.5.3). However, in the diabatic surface boundary layer the series expansion of ψ^* is alternating and initially increasing[4], which precludes an adequate approximate surface layer representation by low order terms, i.e. leads to the "break down" of an approximation of ψ^*. Hence, the series approach of Eden et al. (2007) seems to be unable to practically solve the problems at the boundaries appearing in the residual-mean framework.

[4] In this study, we call a series expansion $s = \sum_{i=1}^{\infty} s_i$ *increasing* (or *decreasing*), if the magnitude of the terms of s is increasing (or decreasing) with higher order i, i.e. $|s_i| < |s_{i+1}|$ (or $|s_i| > |s_{i+1}|$).

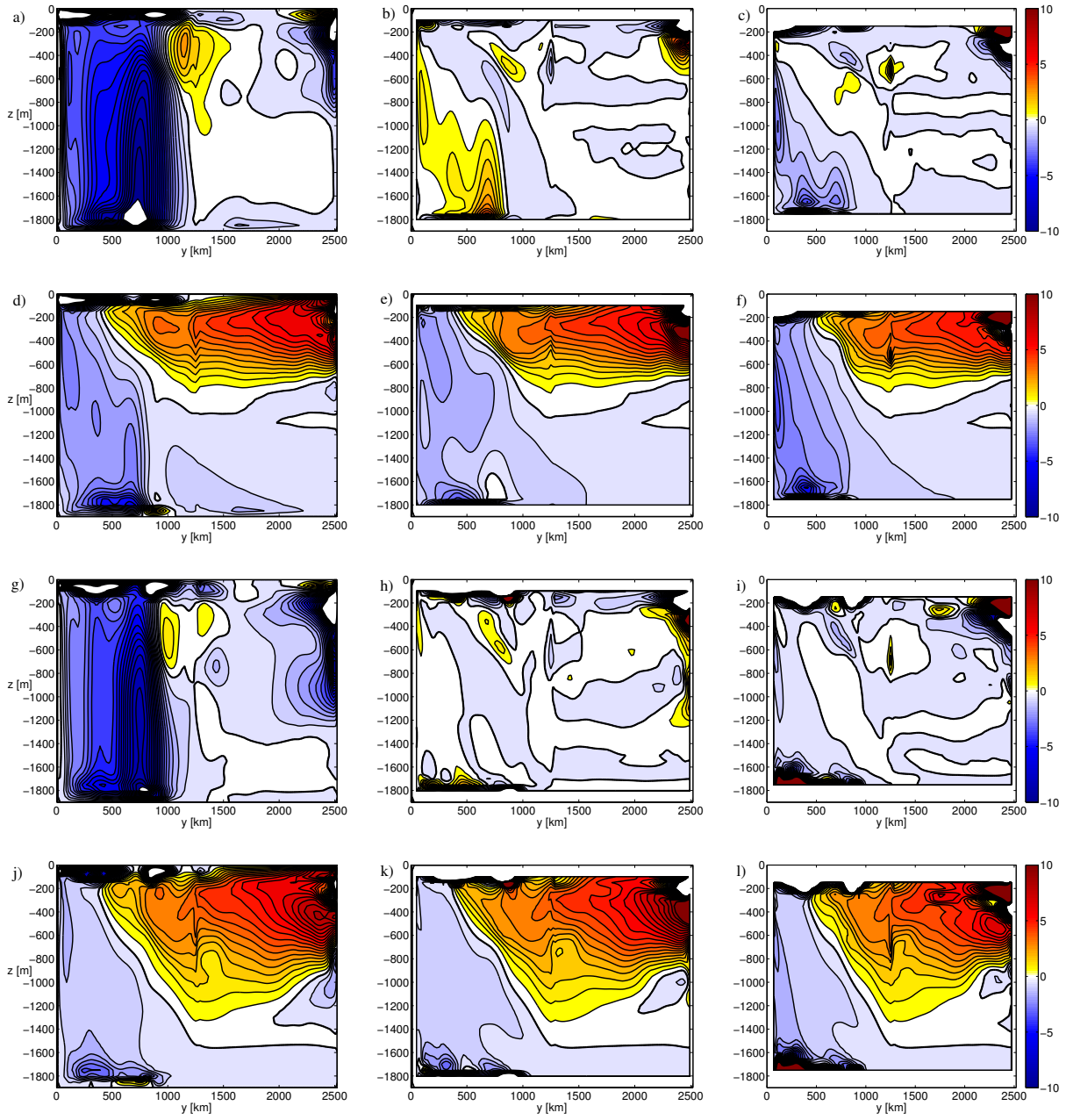

Figure 4.2: The first three terms of the series expansion of ψ^* for the flat case: ψ^*_I (a), ψ^*_{II} (b), ψ^*_{III} (c) and the corresponding residual streamfunctions including terms of ψ^* up to the first (d), second (e), third (f) order. (g-i) and (j-l) show the same quantities, but for the flat case experiment including a harmonic viscosity of $A_h = 2000\mathrm{m}^2\mathrm{s}^{-1}$. The contour interval is 0.5Sv and zero lines are thick.

4.4.2 Flat case

Fig. 4.2 a) shows ψ_I^*, i.e. the TEM eddy streamfunction of the flat case, which shows the well-known eddy-induced streamfunction behaviour in the SO (extending from $x = 0$km to $x = L/2$): A strong negative circulation pattern, which opposes the positive circulation pattern of $\overline{\Lambda}$ (not shown, see e.g. Viebahn and Eden (2012)) in the SO, such that the sum of both, i.e. the TEM residual streamfunction shown in Fig. 4.2 d), is given by two global overturning cells. Namely, a positive circulation cell which connects the SO and the Atlantic and a bottom reaching negative circulation cell. We notice that, on the one hand, the residual MOC in the SO is of equal magnitude as the residual MOC of the NL case[5], but, on the other hand, the magnitude of ψ_I^* is significantly larger, since $\overline{\Lambda}$ is not small. However, we find problems at the boundaries analog to the problems already encountered in the NL case. ψ_I^* now shows large and unphysical[6] negative recirculation cells in the surface boundary layer and in the bottom boundary layer in the SO, which are also present in the TEM residual MOC $\overline{\Lambda} + \psi_I^*$. Due to the coarser vertical resolution of our second model configuration, we can not discuss in detail the boundary layer behaviour of the next higher order terms of the series expansion of ψ^*. Nevertheless, the few boundary layer values suggest the same unsolved practical problem as in the NL case, namely, next higher order terms ψ_i^* of increasing magnitude such that an adequate approximate boundary layer circulation given by low order terms is impossible.

But we can consider the behaviour of the subsequent terms of the series expansion of ψ^* in the ocean interior. Fig. 4.2 b,c) show ψ_{II}^* and ψ_{III}^*. As expected, ψ_I^* dominates over ψ_{II}^* and ψ_{III}^* in the interior of the SO. However, both ψ_{II}^* and ψ_{III}^*, although being smaller than ψ_I^* everywhere in the interior of the SO, show magnitudes of the same order as ψ_I^* below $z = -950$m and at mid-depth around $y = 1000$km. Moreover, we notice the strong changes in the diabatic northern convective region. Hence, both terms induce significant changes in the residual MOC (Fig. 4.2 e,f)): Especially the negative circulation cell changes both magnitude and circulation pattern by the inclusion of each term. In case both ψ_{II}^* and ψ_{III}^* are included (Fig. 4.2 f)), the streamlines of the residual MOC in the SO are significantly more aligned along the time-zonal-mean isopycnals in the interior (compare Fig. 4.2 d-f)

[5] That is, the watermass transformations are similar in both cases (Walin, 1982; Marshall and Radko, 2003).

[6] We note that "unphysical" primarily means that ψ_I^* does not tend to zero at the horizontal boundaries, while, for averaging along latitude circles, negative recirculation cells at the surface are also found in an isopycnal averaging framework - as shown for both the flat case and the hill case in Fig. 4.6 b,c) and discussed by Viebahn and Eden (2012).

with Fig. 4.6 b,e)). Hence, in the flat case the inclusion of the next higher order terms ψ^*_{II} and ψ^*_{III} distinctly improves the approximation of ψ^* by ψ^*_I alone.

Furthermore, ψ^*_{II} mainly opposes the interior circulation of ψ^*_I, while ψ^*_{III} largely amplifies it. That is, the series expansion of ψ^* is again alternating (similar to the NL case), which is obvious in Fig. 4.2 a-c) and continued for the next higher order terms ψ^*_{IV} and ψ^*_V (not shown). However, with increasing order i the ratio $|\psi^*_i|/|\psi^*_I|$ (not shown) decreases in the interior of the SO, which suggests that the desired behaviour of an in general decreasing series expansion essentially holds in the interior of the SO. We can conclude: In the flat case, the series expansion of ψ^* is alternating and may be adequately approximated by low order terms in the ocean interior, since there they appear to be decreasing. However, the next higher order terms ψ^*_{II} and ψ^*_{III} significantly improve an approximation of ψ^* by ψ^*_I alone. Hence, the series approach of Eden et al. (2007) represents an advancement of the description of the ocean interior circulation within the residual-mean framework.

Now, in order to minimise the impact of the next higher order terms ψ^*_{II} and ψ^*_{III}, i.e. in order to obtain a faster convergence of the series expansion of ψ^* in the interior of the SO, we introduced a harmonic viscosity of $A_h = 2000\mathrm{m}^2\mathrm{s}^{-1}$ in the flat case. A_h acts to damp EKE and hence the corresponding TEM eddy streamfunction ψ^*_I, shown in Fig. 4.2 g), has a weaker but still strong negative circulation cell in the SO (while the negative circulation in the northern convective region is increased and extended). The TEM residual MOC, i.e. $\overline{\Lambda} + \psi^*_I$ (Fig. 4.2 j)), shows a significantly weaker bottom reaching negative circulation cell, while the global positive circulation cell extends much deeper, but remains of the same magnitude in the SO (of course, also $\overline{\Lambda}$ (not shown) changes). The next higher order terms ψ^*_{II} and ψ^*_{III} shown in Fig. 4.2 h,i) (as well as ψ^*_{IV} and ψ^*_V, not shown) are now significantly reduced (except for an increase in the northern convective region), such that in the interior of the SO, ψ^* is essentially given by ψ^*_I. Only in a small band at mid-depth around $y = 1000\mathrm{km}$ the next higher order terms ψ^*_{II} and ψ^*_{III} show significant values, which almost disappear for ψ^*_{IV} and ψ^*_V (not shown). The reduced impact of the next higher order terms is more accurately expressed by the behaviour of the ratio $|\psi^*_i|/|\psi^*_I|$ (not shown), which is also drastically reduced in the interior of the SO. Consequently, in the flat case the impact on the TEM eddy streamfunction ψ^*_I by the gauge potential introduced by Eden et al. (2007) (see Eq. (4.23)) related to rotational eddy fluxes depends directly on the "strength" of the eddy field, i.e. the magnitude of the EKE. Hence, if the EKE is adequately reduced, it seems acceptable to approximate ψ^* by ψ^*_I in the nearly adiabatic interior of the SO in the flat case. We notice that the series expansion remains

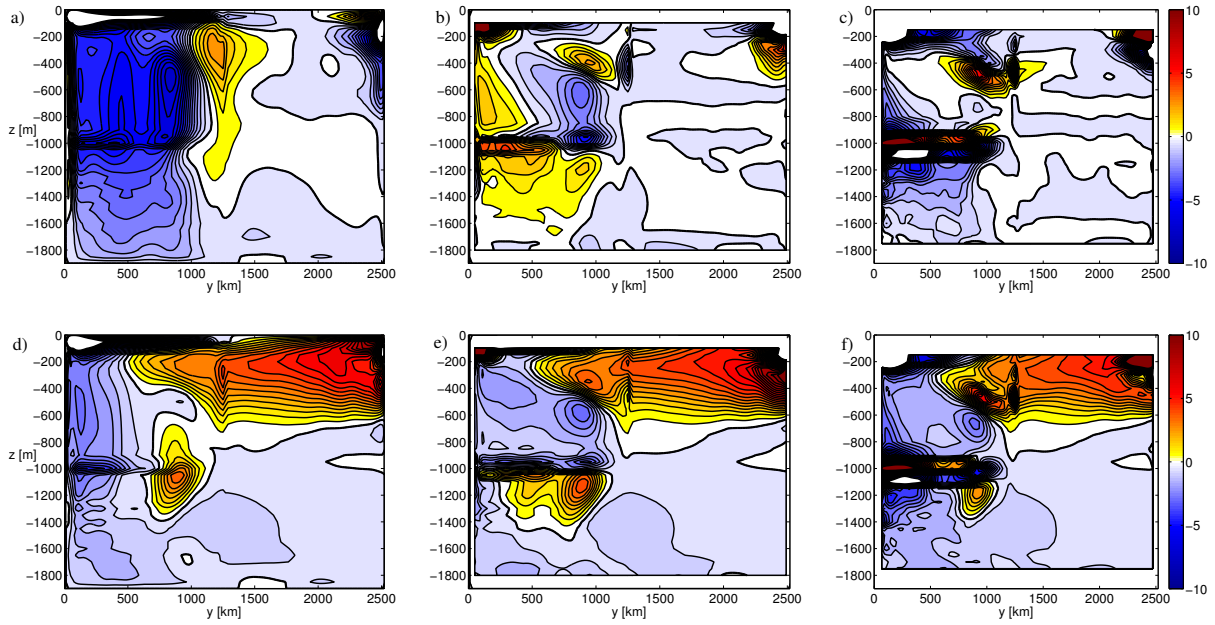

Figure 4.3: The first three terms of the series expansion of ψ^* for the hill case: ψ^*_I (a), ψ^*_{II} (b), ψ^*_{III} (c) and the corresponding residual streamfunctions including terms of ψ^* up to the first (d), second (e), third (f) order. The contour interval is 0.5Sv and zero lines are thick.

alternating and note that in the diabatic regions at the surface, at the bottom and at the northern and southern boundaries convergence is far from being reached by including the first three orders (see Fig. 4.2 g-i)).

4.4.3 Hill case

Fig. 4.3 a) shows the TEM eddy streamfunction ψ^*_I of the hill case. Compared to the flat case, the negative circulation is reduced at topographic depths, in particular a bottom boundary layer is absent. This is in accordance with the geostrophic return flow of $\overline{\Lambda}$ (not shown, see Viebahn and Eden (2012)) in the hill case, which extends over the depth range below the hill depth and is not confined to a bottom boundary layer as in the flat case. On the other hand, the number of local maxima in ψ^*_I is increased: One local maximum is found above topography around $y = 800$km and 500m depth. Moreover, meridional recirculation cells appear around the hill depth[7] ($z = -950$m), which induce a negative and a positive

[7] Note that in the isopycnal eddy streamfunction meridional recirculation cells around the hill depth do not appear, as shown by Viebahn and Eden (2012). See also Fig. 4.6 c).

recirculation cell around the hill depth in the TEM residual MOC $\overline{\Lambda} + \psi_I^*$ (Fig. 4.3 d)). These recirculation cells represent strong diapycnal flow and hence contradict the physical picture of a nearly adiabatic flow in the interior of the SO. Consequently, we would expect the next higher order terms to reduce these cells in order to obtain a physically more consistent circulation pattern.

Fig. 4.3 b,c) show ψ_{II}^* and ψ_{III}^*. While ψ_{II}^* and ψ_{III}^* exhibit the same circulation pattern in the Atlantic part as in the flat case, they are drastically increased in the SO part, in particular around the hill depth (along the entire meridional extension of the SO) and above topography (around $y = 800$km and 400m depth). The maximal values now lie around the hill depth and not near the bottom as in the flat case. ψ_{II}^* partially compensates for the spurious diabatic recirculation cells in the residual MOC $\overline{\Lambda} + \psi_I^*$ with a negative circulation around $y = 900$km and a positive circulation around $y = 400$km at the hill depth. Nevertheless, the inclusion of ψ_{II}^* appears to overcompensate (Fig. 4.3 e)): The number and the magnitude of the recirculation cells around the hill depth and above topography is increased such that the overall circulation pattern becomes more unphysical. This tendency of intensifying the recirculation cells and complicating the circulation pattern continues, if ψ_{III}^* is included (Fig. 4.3 f)).

Furthermore, the magnitude of ψ_{III}^* is even larger than the magnitude of ψ_{II}^* for most parts of the SO. More precisely, we find that with increasing order i the ratio $|\psi_i^*|/|\psi_I^*|$ (not shown) increases in the interior of the SO, with values greater 1 around the hill depth already for $i = II$. As in the flat case, the next higher order terms ψ_{II}^* and ψ_{III}^* (also ψ_{IV}^* and ψ_V^*, not shown) of the series expansion of ψ^* still show a type of alternating behaviour, but the behaviour of a decreasing series expansion seems to be completely lost in the hill case.

This drawback of a, at least initially, increasing series expansion does not disappear, if a harmonic viscosity A_h is introduced in the hill case[8]. By increasing A_h, expectedly the overall magnitude of the TEM eddy streamfunction ψ_I^* decreases. Moreover, the circulation pattern of ψ_I^* deforms with increasing A_h, such that the negative recirculation cell at the hill depth of the residual MOC $\overline{\Lambda} + \psi_I^*$ decreases. For example, if $A_h = 10000\text{m}^2\text{s}^{-1}$ is used, the negative circulation cell of the TEM residual MOC is nearly void of recirculation cells in the nearly adiabatic interior, but the accompanying positive recirculation cell is drastically increased. While $A_h = 2000\text{m}^2\text{s}^{-1}$ has a rather small impact on ψ^* and the residual MOC in the hill case, $A_h = 5000\text{m}^2\text{s}^{-1}$ leads to the strongest reduction of the next

[8] We do not show further hill case figures due to their physical disqualification.

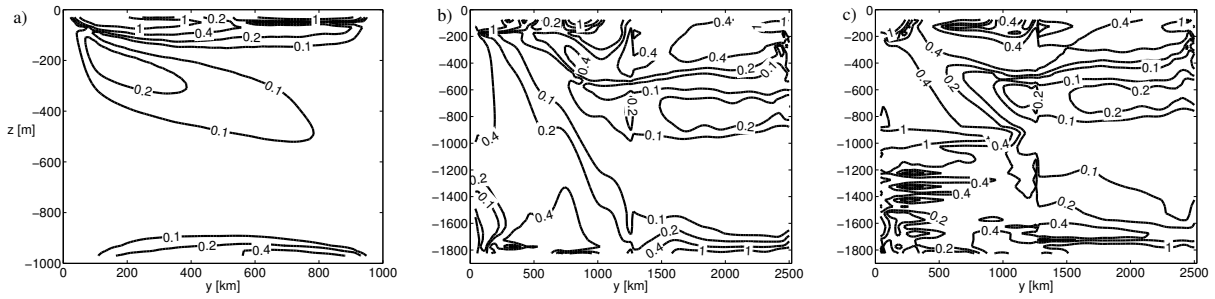

Figure 4.4: Series number S for the NL case (a), the flat case (b) and the hill case (c). Contour lines are 0.1, 0.2, 0.4 and 1.

higher order terms ψ^*_{II} and ψ^*_{III} (in particular above topography) for our set of A_h values. Nevertheless, for all three values of A_h the next higher order terms ψ^*_i (we considered terms up to $i = V$) conserve the previous features: In an alternating manner, the magnitudes increase and the circulation patterns complicate with higher orders i. In particular, the ratios $|\psi^*_i|/|\psi^*_I|$ (not shown) increase in the SO with more and more regions in the SO of values greater than 1.

Consequently, in the hill case the series expansion of ψ^* may not have a reasonable cut off, since it seems to be, at least initially, an increasing series expansion in broad regions of the SO. Now even in the interior the residual-mean approach, both in its classical TEM version and in its advancement by Eden et al. (2007), is dissatisfying.

4.4.4 Series number

In the previous sections, we demonstrated that an approximation of ψ^* by low order terms of its series expansion is impossible in certain regions of the ocean, since the series expansion of ψ^* is increasing there. These regions are mainly the horizontal boundary layers, which are generally characterised by diabatic processes, i.e. by large diapycnal diffusivities. An exception we found in the hill case, where the series expansion of ψ^* is also increasing at mid-depth above topography. We are able to give an indicator of whether the series expansion of ψ^* is initially increasing or decreasing by consulting the results of Eden et al. (2009b). They were able to derive the generalised Osborn-Cox relation,

$$\kappa + \mu = \mu\overline{(1 + C)\exp(-Db')} \ , \tag{4.4}$$

which relates the turbulent diapycnal diffusivity κ to the molecular diffusivity μ, the Cox number $C = |\nabla b'|^2/|\nabla \bar{b}|^2$ and the dimensionless ratio Db' relating the buoyancy perturbation with the mean curvature scale $D = (\nabla^2 \bar{b})/|\nabla \bar{b}|^2$. The ratio Db' appears in the argument of the exponential map, which represents a standard example of a converging series which is initially increasing, if the argument is greater than 1. Hence, as a measure of whether the series expansion of κ, given by Eq. (4.4), is initially increasing or decreasing, we define the *series number*,

$$S \equiv |D|\sqrt{2\overline{\phi_2}}\,, \tag{4.5}$$

such that we expect for $S > 1$ (or near 1) an initially increasing series expansion. Since κ appears on the one side and ψ^* on the other side of the Eulerian mean buoyancy budget (see Eq. (4.16) in appendix A), we carry this criterion over to the series expansion of ψ^*.

Fig. 4.4 a) shows S for the NL case. As expected, we find $S > 1$ only in the surface boundary layer. Below the surface boundary layer, it holds $S < 1$, with the highest values near the bottom. Fig. 4.4 b) shows S for the flat case. We find $S > 1$ in the southern surface boundary layer, the northern convective region and in the bottom boundary layer[9]. In the ocean interior of the SO, it holds $S < 1$. Introducing A_h (not shown) generally decreases S in the interior of the SO, but increases S in the boundary layers and in the Atlantic part. Finally, Fig. 4.4 c) shows S for the hill case. As expected, we find $S > 1$ now at the top of topography and not at the bottom in the SO, while in the rest of the ocean interior it holds $S < 1$. In particular, at mid-depth above topography in the SO, where the series expansion of ψ^* is initially increasing, S is increased compared to the flat case, but we still have $S < 1$. Hence, in regions of smaller diapycnal diffusivity the criterion is of reduced evidence. For $A_h = 5000\mathrm{m}^2\mathrm{s}^{-1}$ the series number S decreases at the hill depth, but it still holds $S > 1$ (not shown). For $A_h = 10000\mathrm{m}^2\mathrm{s}^{-1}$ the series number S is again drastically increased in the entire domain (not shown).

Consequently, in the diabatic boundary regions and at topographic depths the series number S represents a successful[10] measure in our model experiments of whether the series expansion of ψ^* is, at least initially, increasing or not, while in the nearly adiabatic interior above topography the criterion is of reduced evidence in the hill case.

[9] In the boundary layer of the SO, the values of S are around 0.96 (and the lowest two grid points are missing due to the second order derivatives), while in the cases with A_h, S significantly exceeds 1 in the bottom boundary layer of the SO.

[10] Notice that the ratios $|\psi_i^*|/|\psi_I^*|$ (not shown) generally are greater than 1 in the bottom boundary layer of the Atlantic part, so that $S > 1$ is appropriate there.

4.5 Quasi-Stokes streamfunction

Assuming that the buoyancy field $b(x, y, z, t)$ is vertically strictly monotonic in the entire ocean, the instantaneous isopycnal b_a lies at an instantaneous height $z(x, y, b_a, t) = z_a(y, b_a) + z'_a(x, y, b_a, t)$, where z_a is the time-zonal-mean height of b_a and z'_a is the deviation from the time-zonal-mean, i.e. $\overline{z'_a} = 0$. The time-zonal-mean isopycnal streamfunction $\overline{\psi_I}$ is then the temporally averaged and zonally integrated meridional transport below the instantaneous isopycnal b_a. We may write

$$\overline{\psi_I}(y, b_a) = -L_x \overline{\int_{bottom}^{z_a+z'_a} v \; dz} \; . \tag{4.6}$$

$\overline{\psi_I}$ may be transformed to Eulerian space by identifying each b_a with its mean height z_a. Therewith, the quasi-Stokes streamfunction Ψ^* is defined via the decomposition

$$- L_x \overline{\int_{bottom}^{z_a+z'_a} v \; dz} = \overline{\Lambda}(y, z_a) + \Psi^*(y, z_a) \; , \tag{4.7}$$

that is,

$$\Psi^*(y, z_a) \equiv -L_x \overline{\int_{z_a}^{z_a+z'_a} v \; dz} \; , \tag{4.8}$$

and gives the transport of $\overline{\psi_I}$ related to the perturbation z'_a. Ψ^* is the eddy-induced streamfunction of $\overline{\psi_I}$ in Eulerian space[11]. Expressions of both z'_a and Ψ^* by Eulerian mean quantities may be obtained by expanding b and v in Taylor series centerd around z_a (McDougall and McIntosh, 2001; Nurser and Lee, 2004b) as outlined in appendix B. If we define the orders of the series expansion by the perturbations of b in order to obtain a form comparable to the residual-mean framework (see Eq. (4.2) and Eq. (4.3)), we find the following series expansion for Ψ^* expressed by Eulerian mean quantities (see appendix B)

$$\Psi^* \;\; = \;\; \Psi^*_I + \Psi^*_{II} + \Psi^*_{III} + O(b'^4) \; , \tag{4.9}$$

where

[11] In Viebahn and Eden (2012) the corresponding decomposition is defined in an isopycnal framework.

$$\Psi^*_I = \frac{L_x\overline{b'v'}}{\partial_z\overline{b}} = \psi^*_I \tag{4.10}$$

$$\Psi^*_{II} = -\frac{1}{\partial_z\overline{b}}\partial_z\left(\frac{L_x\overline{\phi_2 v}}{\partial_z\overline{b}}\right) + \frac{\overline{v}}{\partial_z\overline{b}}\partial_z\left(\frac{L_x\overline{\phi_2}}{\partial_z\overline{b}}\right) = \psi^*_{II} + \psi^*_{\Delta II} \tag{4.11}$$

$$\begin{aligned}\Psi^*_{III} &= \frac{1}{2}\frac{1}{\partial_z\overline{b}}\partial_z\left(\frac{1}{\partial_z\overline{b}}\partial_z\left(\frac{L_x\overline{\phi_3 v}}{\partial_z\overline{b}}\right)\right) - \frac{1}{2}\frac{\overline{v}}{\partial_z\overline{b}}\partial_z\left(\frac{1}{\partial_z\overline{b}}\partial_z\left(\frac{L_x\overline{\phi_3}}{\partial_z\overline{b}}\right)\right) - \frac{L_x^{-1}}{\partial_z\overline{b}}\partial_z\left(\frac{L_x\overline{\phi_2}}{\partial_z\overline{b}}\right)\partial_z\left(\frac{L_x\overline{v'b'}}{\partial_z\overline{b}}\right) \\ &= \psi^*_{III} + \psi^*_{\Delta IIIa} + \psi^*_{\Delta IIIb}\end{aligned} \tag{4.12}$$

4.5.1 Comparison of ψ^* and Ψ^*

It is obvious that the complete series expansions of ψ^* and Ψ^* are essentially different, since ψ^* and Ψ^* advect different time-zonal-mean buoyancy distributions. However, the corresponding time-zonal-mean buoyancy distributions mainly differ in the boundary layers, while in the nearly adiabatic interior of the ocean they are generally found to be similar (Killworth, 2001; Nurser and Lee, 2004a; Viebahn and Eden, 2012). Hence, the two streamfunctions are expected to be similar there too.

By comparing Eq. (4.9) with Eq. (4.3), the similarity of ψ^* and Ψ^* is suggested by the identity of the first order terms. However, we find that with increasing order the series expansions of ψ^* and Ψ^* deviate more and more from each other. The difference between the second order terms, $\psi^*_{\Delta II}$, is given by a term including the time-zonal-mean meridional velocity, which is generally small in a zonal channel. The difference between the third order terms is constituted by a corresponding term, $\psi^*_{\Delta IIIa}$, including the time-zonal-mean meridional velocity and an additional term, $\psi^*_{\Delta IIIb}$, of a type not present in the residual-mean series expansion, namely, a product of a first order term (the vertical derivative of Ψ^*_I) with a second order term (a variance term). For higher order terms we expect even more complicated discrepancies, especially further products between different orders, i.e. types of terms not present in the residual-mean series expansion.

Moreover, only in case of Ψ^* we are able to compute the streamfunction directly in an isopycnal framework without referring to the series expansion (Nurser and Lee, 2004a; Viebahn and Eden, 2012). Hence, we know the result to which the series expansion of Ψ^* must converge. In case of ψ^*, we do not have another computational option besides the series expansion. Especially in the diabatic regions, the residual-mean circulation may therefore not be properly determined so far, as demonstrated in section 4.4. Furthermore, it is not even secure so far that the residual-mean series is a converging series expansion.

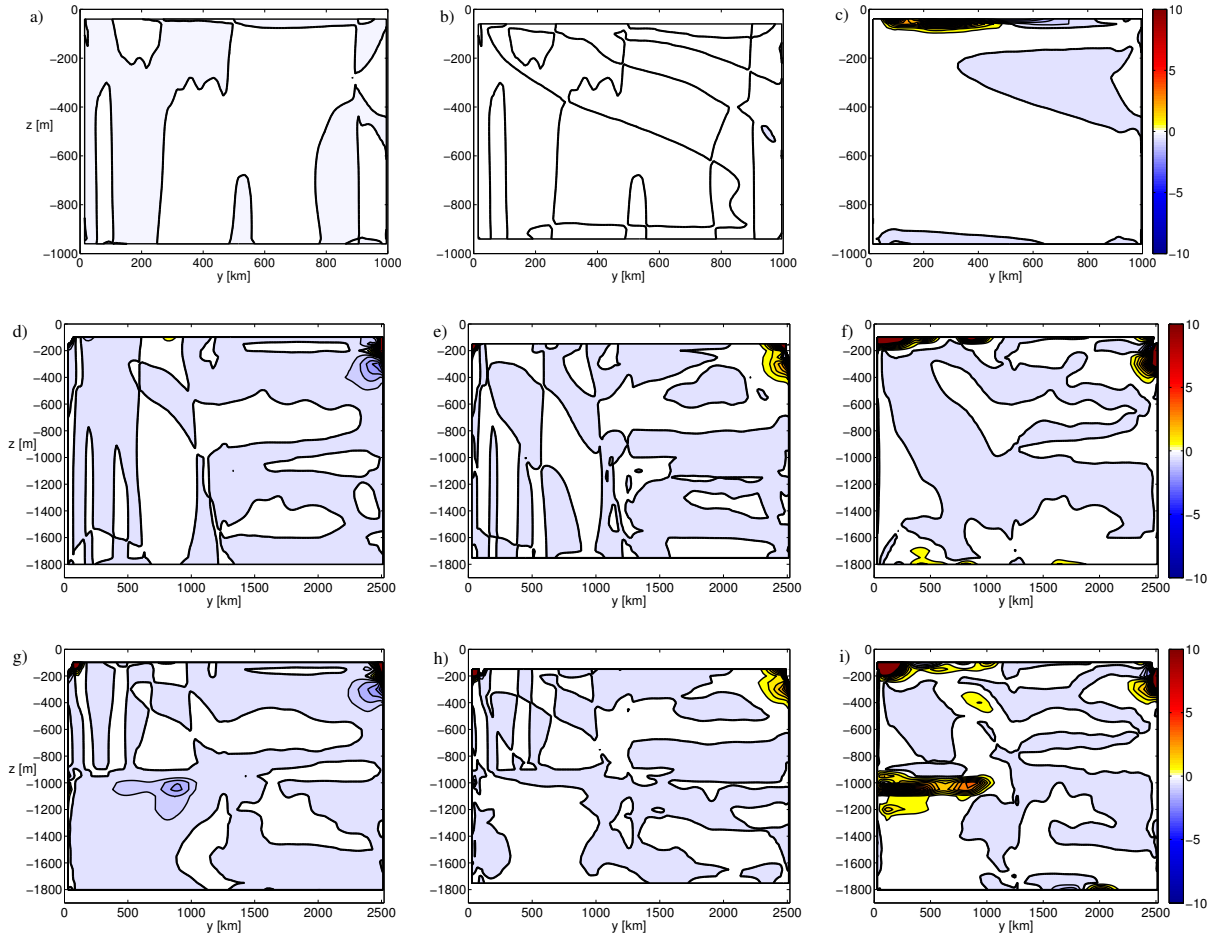

Figure 4.5: $\psi^*_{\Delta II}$, $\psi^*_{\Delta IIIa}$ and $\psi^*_{\Delta IIIb}$ for the NL case (a-c), the flat case (d-f) and the hill case (g-i). The contour interval is 0.5Sv and zero lines are thick.

Up to now, the advantage of the residual-mean series over series expansion of Ψ^* is that it is given in a compact and complete form, while we have not found a corresponding expression for the series expansion of Ψ^* yet.

Now we return to our three model experiments. In each case, we discuss the three additional terms appearing in Eq. (4.9) and not in Eq. (4.3), and we consider the streamfunction to which the series expansions Ψ^* has to converge .

4.5.2 Differences between the series expansions of ψ^* and Ψ^* in model experiments

Fig. 4.5 a-c) shows $\psi^*_{\Delta II}$, $\psi^*_{\Delta IIIa}$ and $\psi^*_{\Delta IIIb}$ for the NL case. Both $\psi^*_{\Delta II}$ and $\psi^*_{\Delta IIIa}$, related to $\overline{v} \approx 0$, essentially vanish, even in the surface boundary layer (as far as it is resolved). In contrast, the third order difference term $\psi^*_{\Delta IIIb}$, related to the product of a variance term and an eddy buoyancy flux term, exhibits significant values in the surface boundary layer. Consequently, the difference between the terms of the series expansions of Ψ^* and ψ^* appears to increase with higher order. In accordance with our expectation, the differences $\psi^*_{\Delta II}$, $\psi^*_{\Delta IIIa}$ and $\psi^*_{\Delta IIIb}$ suggest that ψ^* and Ψ^* mainly differ in the diabatic surface layer, while they are similar in the nearly adiabatic ocean interior. More precisely, $\psi^*_{\Delta IIIb}$ is of the same sign as ψ^*_{III} (Fig. 4.1 c)) in the northern part of the channel, while $\psi^*_{\Delta IIIb}$ is opposing ψ^*_{III} in the southern part of the channel. Hence, the maximal absolute values of Ψ^*_{III} are slightly smaller than those of ψ^*_{III}. This might indicate that the series expansion of Ψ^* converges faster then that of ψ^*. Nevertheless, the overall characteristics of the low order terms of the series expansion of Ψ^* remain those described in section 4.4.1.

Fig. 4.5 d-f) show $\psi^*_{\Delta II}$, $\psi^*_{\Delta IIIa}$ and $\psi^*_{\Delta IIIb}$ for the flat case. In line with our expectation, each term is small in the interior of the ocean, such that also the second and third orders of the series expansions of ψ^* and Ψ^* coincide in the ocean interior for the flat case (with characteristics described in section 4.4.2). In particular, the terms $\psi^*_{\Delta II}$ and $\psi^*_{\Delta IIIa}$ are small in the interior, although it holds $\overline{v} \neq 0$. Significant values of $\psi^*_{\Delta II}$, $\psi^*_{\Delta IIIa}$ and $\psi^*_{\Delta IIIb}$ are visible in the northern convective region, while in the surface and bottom boundary layers they are only obvious for $\psi^*_{\Delta IIIb}$ (and probably lost due to the few vertical grid points and the smaller extension for $\psi^*_{\Delta II}$ and $\psi^*_{\Delta IIIa}$). The significant values tend to counteract the corresponding next higher order contributions shown in Fig. 4.2 b,c). Furthermore and similar to the NL case, the term of highest order in perturbation quantities, $\psi^*_{\Delta IIIb}$, exhibits the highest values in the northern convective region and in the southern bottom and surface boundary layers. This tendency of increasing compensation again might indicate that the series expansion of Ψ^* converges faster than the one of ψ^* in the diabatic regions in the flat case.

By including a harmonic viscosity of $A_h = 2000\mathrm{m}^2\mathrm{s}^{-1}$ in the flat case configuration (not shown), the situation is essentially unchanged: The terms $\psi^*_{\Delta II}$, $\psi^*_{\Delta IIIa}$ and $\psi^*_{\Delta IIIb}$ remain small in the ocean interior. In accordance with Fig. 4.2 h,i), the magnitudes of the significant values in the boundary regions are increased compared to the case of vanishing A_h, such that significant values also appear in $\psi^*_{\Delta II}$ in the surface layer. The term $\psi^*_{\Delta IIIb}$

still shows the highest values, in particular in the southern bottom and surface boundary layers of the SO, so that a tendency of increasing compensation is furthermore present.

So far all considered cases are in line with expectations: In the ocean interior ψ^* and Ψ^* essentially coincide, while in the boundary regions significant differences between ψ^* and Ψ^* are given by $\psi^*_{\Delta II}$, $\psi^*_{\Delta IIIa}$ and $\psi^*_{\Delta IIIb}$, such that the next higher order terms of the series expansion of Ψ^* tend to be smaller than the corresponding terms of ψ^*.

Turning to the hill case, the question is: Do the additional terms $\psi^*_{\Delta II}$, $\psi^*_{\Delta IIIa}$ and $\psi^*_{\Delta IIIb}$ add to the residual-mean terms at each order such that the series expansion of Ψ^* is decreasing and that the recirculation cells in the ocean interior, encountered in section 4.4.3, disappear? This is not the case. Fig. 4.5 g-i) show $\psi^*_{\Delta II}$, $\psi^*_{\Delta IIIa}$ and $\psi^*_{\Delta IIIb}$ for the hill case. In the Atlantic part ($x > 1250$km), each term shows nearly the same pattern as in the flat case, similar to the terms ψ^*_I, ψ^*_{II} and ψ^*_{III} encountered in section 4.4.3. However, in the SO now significant values appear in the ocean interior. The second order term $\psi^*_{\Delta II}$, related to $\overline{v}$, exhibits a small negative recirculation cell around $y = 800$km at 1100m depth. This leads to a small reduction of the corresponding positive recirculation cell in Fig. 4.3 e), but the overall pattern remains unchanged (not shown). The same holds for the third order: Although $\psi^*_{\Delta IIIa}$, related to $\overline{v}$, vanishes, $\psi^*_{\Delta IIIb}$ induces a strong positive recirculation cell at the hill depth and a smaller one at mid-depth ($y = 900$km and $z = -400$m), which, however, only slightly change the circulation pattern of Fig. 4.3 f) (not shown). Consequently, also in the hill case we find that the significant values of the next higher order terms of the series expansion of Ψ^* tend to be reduced compared to than those of ψ^*. But the overall circulation pattern in not essentially changed by including the lower orders, so that the unphysical recirculation cells in the ocean interior remain.

Including a harmonic viscosity A_h in the hill case configuration does not change the situation. In case of $A_h \equiv 5000\text{m}^2\text{s}^{-1}$ (not shown), the magnitudes of both $\psi^*_{\Delta II}$ and $\psi^*_{\Delta IIIb}$ are reduced in the ocean interior, but still significant, while $\psi^*_{\Delta IIIa}$ now shows a negative recirculation cell around $y = 800$km at 1100m depth. However, the unphysical circulation patterns are only slightly changed by the inclusion of the quasi-Stokes terms (not shown). The analog situation is met if A_h is set to $A_h \equiv 10000\text{m}^2\text{s}^{-1}$ (not shown). Each term exhibits recirculation cells around the top of topography with drastically increased magnitudes. However, since the magnitudes of ψ_{II} and ψ_{III} are even more increased, the overall effect remains small (not shown).

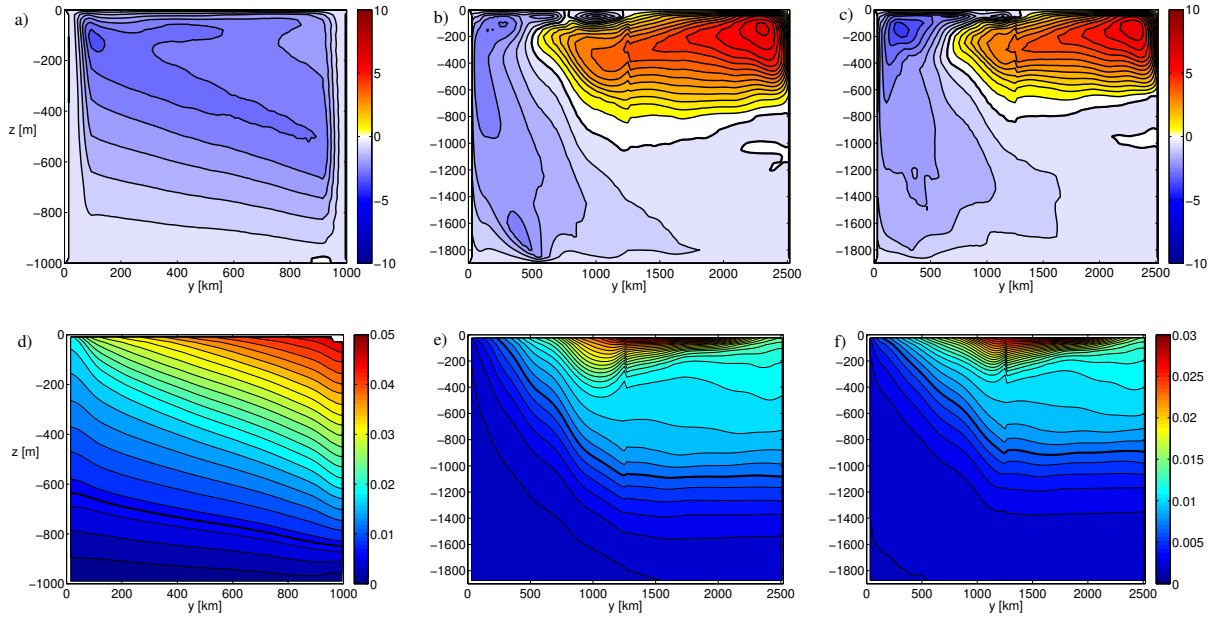

Figure 4.6: Isopycnal streamfunction transformed to depth coordinates via the mean height of isopycnals (Nurser and Lee, 2004a) for the NL case (a), flat case (b) and hill case (c). The contour interval is 0.5Sv and zero lines are thick. Below are shown the corresponding mean isopycnals (i.e. the isopycnally averaged buoyancy distributions), where in the NL case (d) the contour interval is $0.002\mathrm{m/s}^2$, while in the flat case (e) and the hill case (f) the contour interval is $0.001\mathrm{m/s}^2$. In all three cases the $0.007\mathrm{m/s}^2$ line is thick.

4.5.3 Ψ^* in model experiments computed from an isopycnal framework

For completeness we show in Fig. 4.6 the isopycnal streamfunction of the NL case (a), flat case (b) and hill case (c), and the corresponding mean isopycnals, which largely have been discussed in Nurser and Lee (2004a) and Viebahn and Eden (2012). Comparing Fig. 4.6 a) with Fig. 4.1 d-f) we again find that the interior circulation is significantly improved by the incorporation of the second and third order terms, while in the upper 200m convergence is far from being reached. In the flat case, comparing Fig. 4.6 b) and Fig. 4.2 d-f), the problems are slightly more severe, since also, beside the surface layer, in the northern convective region, the southern boundary and the bottom boundary layer in the SO convergence is far from being reached. Finally, the worst scenario we find in the hill case (compare Fig. 4.6 c) with Fig. 4.3 d-f)), where even the interior circulation of the SO becomes completely unphysical by including next higher order terms.

4.6 Summary and discussion

In this study we have considered the series expansion of the residual-mean eddy streamfunction ψ^* and the Taylor expansion of the quasi-Stokes streamfunction Ψ^* up to third order in buoyancy perturbation b'. Beside a formal comparison, we analysed the resulting MOCs at each order in three different eddy-permitting numerical model experiments, namely the NL case experiment, which is largely a reproduction of the idealised zonal channel model setup considered by Nurser and Lee (2004a,b), and the flat case and hill case experiments of the idealised SO model setup introduced by Viebahn and Eden (2010, 2012).

Formally, the series expansions of ψ^* and Ψ^* increasingly differ from each other with increasing order. While the first order terms are identical, the difference between the second order terms is related to the time-zonal-mean meridional velocity $\overline{v}$. Since $\overline{v}$ is generally small in a zonal channel, the second order difference may be expected to be small there as well. The third order difference is constituted by a corresponding term related to $\overline{v}$ and an additional term, which is related to v' and, hence, is of fourth order in perturbation quantities b' and v'. For orders higher than three we expect the emergence of further types of terms related to v'. Regarding a zonal channel, it is likely that the terms related to v' primarily need to be considered in order to distinguish between ψ^* and Ψ^*.

This expectation is confirmed in each of our three model experiments, where the third order difference term related to v' shows the largest magnitudes. Hence, at least initially and in regions of significant values, the magnitudes of the differences between ψ^* and Ψ^* tend to increase with higher order. Significant differences between the terms of the series expansion of ψ^* and the Taylor series of Ψ^* are present in the diabatic boundary regions in the NL case and the flat case, while in the hill case differences are also found in the ocean interior (around hill depth and above[12]). In the NL case and the flat case, this is in accordance with the expectation that both streamfunctions largely coincide in the nearly adiabatic interior, since the corresponding mean buoyancy distributions largely coincide there (Nurser and Lee, 2004a; Viebahn and Eden, 2012). Finally, we find that the terms of Ψ^* generally tend to have smaller magnitudes than the corresponding terms of ψ^*, which might indicate that the series expansion of Ψ^* converges faster than that of ψ^*.

However, despite significant differences in certain regions, the series expansion of ψ^* and the Taylor series of Ψ^*, considered up to the third order in our model experiments,

[12] That is, differences primarily appear in the regions where both series expansions are initially increasing - see two paragraphs further down.

show the same behaviour in several aspects: Both series expansions generally tend to be of alternating character, such that the next higher order always compensates a part of the previous order. Furthermore, in the NL case and the flat case, both series expansions may be adequately approximated by low order terms in the ocean interior, since there they appear to be decreasing with higher order. Nevertheless, including terms up to the third order still significantly improves the interior circulations in these two cases, in the sense that they further approach the corresponding circulation patterns of the isopycnal streamfunction and that streamlines become more aligned along the mean isopycnals in the ocean interior. For the flat case, we showed that the impact of the next higher order terms in the ocean interior may be reduced by the introduction of a harmonic viscosity A_h, which acts to damp EKE and also changes the strength and depth of the circulation cells.

In contrast, in the typically diabatic boundary regions, i.e. the surface boundary layer in the NL case and the surface and bottom boundary layers as well as the northern convective region in the flat case, both series expansions are alternating and increasing, which rules an adequate approximation by low order terms out, as previously discussed by Killworth (2001); McDougall and McIntosh (2001); Nurser and Lee (2004b). This intractable behaviour becomes more pronounced and severe in the hill case. There, physically inconsistent recirculation cells appear around the hill depth in the first order MOC, which are not effectively reduced by the inclusion of next higher order terms. On the contrary, the magnitude of the next higher order terms now even is increasing in the ocean interior (around hill depth and above topography around 500m depth), which further intensifies the recirculation cells and complicates the circulation patterns. This drawback of initially increasing series expansions does not disappear, if a harmonic viscosity A_h is introduced in the hill case. Consequently, an approximation of the ocean interior circulation by low order terms seems not to be possible in the hill case.

The increasing behaviour of both series expansions in certain regions of the ocean is the handicap which precludes a satisfying approximation of ψ^* or Ψ^* by low order terms. As an indicator of whether the series expansion of ψ^* is initially increasing or decreasing, we proposed the series number S, i.e. a dimensionless ratio relating the buoyancy perturbation with the mean isopycnal curvature scale. We find that in the diabatic boundary regions and at topographic depths, S represents a successful measure in our model experiments of whether the series expansion of ψ^* is initially increasing or not, while in the nearly adiabatic interior above topography, S is of reduced evidence. Since the increasing behaviour of the series expansion of Ψ^* is similar to the one of ψ^* in our model experiments, S applies in

the same way to Ψ^*.

Consequently, in our model experiment which is equipped with a significant topographic feature and which hence represents the most realistic model setup, the approximations of the zonal-mean streamfunctions ψ^* and Ψ^* are most inappropriate. In order to interpret this problematic behaviour in the ocean interior in the hill case, we distinguish two regions, namely, on the one hand, the region around the hill depth and below, and, on the other hand, the interior region above topography. We interpret the problematic behaviour of the low order terms of ψ^* and Ψ^* in the former region as a zonally integrated boundary layer effect. As demonstrated in the NL case (section 4.4.1) and the flat case (section 4.4.2) and discussed in several previous studies (Killworth, 2001; McDougall and McIntosh, 2001; Nurser and Lee, 2004b), the approximations of ψ^* and Ψ^* typically break down in the horizontal boundary layers, which are generally characterised by diabatic processes and a vertically non-monotonic buoyancy field. While in the flat case these regions (surface, bottom) remain at fixed depth in the zonal dimension, the bottom boundary layer extends zonally over the hill-like topography in the hill case. More precisely, in the hill case we find significant values of the vertical diffusivity (not shown) indicating a small bottom boundary layer all along the bottom, but most pronounced at the hill depth. Hence, in the hill case, bottom boundary layer regions and interior parts are mixed up at topographic depths in the zonal integration carried out at fixed depth and along latitude circles. This mixture of boundary and interior regions precludes appropriate approximations of ψ^* and Ψ^* at topographic depths in a zonal-mean framework.

The second region of significant and increasing contributions in the lower order terms $\psi^*_{II}, \psi^*_{III}, ...$ and $\Psi^*_{II}, \Psi^*_{III}, ...$ is found above topography and centered around $y = 900$km. We do not relate the pure appearance of these contributions to the presence of topography, since they are also found, although weaker, in the flat case, even if the EKE is reduced by the introduction of A_h (see Fig. 4.2). But we ascribe the increasing behaviour of these contributions to the impact of topography on the zonal structure of the velocity and buoyancy fields: Typically, undulations emerge horizontally in the physical fields as an effect of topography (so-called standing eddies, Viebahn and Eden (2012)). In a zonal-mean framework of zonal integration along latitude circles, these undulations induce the amplification of the significant contributions above topography. However, the effect of standing eddies on the eddy streamfunctions vanishes, if the zonal integration paths are redefined so that the topographic influence is taken into account, or, more precisely, if the zonal integration is performed along time-mean isolines of buoyancy (which coincide with

latitude circles in the flat case), as discussed by Viebahn and Eden (2012). If the zonal integration paths are defined this way, the zonal-mean eddy circulations of the flat case and the hill case are more similar to each other. Hence, we expect that in a framework of zonal integration along time-mean isolines of buoyancy, an approximation of ψ^* and Ψ^* in the interior above topography would be possible again, just like in the flat case. In other words, we interpret the increasing behaviour above topography in the hill case not as a boundary layer effect in the zonal average, but as a topographic effect which might be circumvented by the appropriate choice of zonal integration paths. Moreover, also at topographic depths a reduction of the impact of the lower order terms might result from an appropriate redefinition of the zonal integration paths, but probably an effect of the boundary layer presence in the zonal average is inevitable.

4.7 Appendix

4.7.1 Outline of the residual-mean framework

The time-zonal-mean residual streamfunction $\psi_{res}(y,z)$ is defined as the meridional streamfunction which advects the Eulerian time-zonal-mean buoyancy $\overline{b}$. The time-zonal-mean buoyancy budget under steady state conditions is given by

$$\overline{v}\partial_y\overline{b} + \overline{w}\partial_z\overline{b} + L_x^{-1}\big(\partial_y\big(L_x\overline{v'b'}\big) + \partial_z\big(L_x\overline{w'b'}\big)\big) = \overline{Q}\ , \tag{4.13}$$

where we used the decompositions[13] $b = \overline{b} + b'$, $v = \overline{v} + v'$ and $w = \overline{w} + w'$. The advection due to the time-zonal-mean velocity $(\overline{v}, \overline{w})$ is described by the time-zonal-mean Eulerian streamfunction $\overline{\Lambda}$,

$$\partial_z\overline{\Lambda} = -L_x\overline{v}\ , \qquad \partial_y\overline{\Lambda} = L_x\overline{w}\ . \tag{4.14}$$

The eddy buoyancy flux $\mathbf{F}_b \equiv L_x(\overline{v'b'}, \overline{w'b'})$ may be decomposed into an additional advective part[14] $-\psi^*\underline{\nabla}\overline{b}$ (directed along the time-zonal-mean isopycnals) and a diffusive part (Andrews and McIntyre, 1976). The natural choice is to direct the diffusive part perpendicular to the advective part, i.e. along the buoyancy gradient $\nabla\overline{b}$ (Andrews and McIntyre, 1978b). This decomposition of the eddy buoyancy flux $\mathbf{F}_b$ is defined only up to an arbitrary

[13] In a time-zonal-mean context, each quantity q generally may be decomposed into its temporal and zonal average $\overline{q}$ and its temporal and zonal deviation $q' \equiv q - \overline{q}$, i.e. $q = \overline{q} + q'$.

[14] The operator $\underline{\nabla}$ is defined as $\underline{\nabla} \equiv (-\partial_z, \partial_y)$.

rotational flux $\mathbf{F}_* = -\underset{\neg}{\nabla}\theta$, given by the gauge potential θ, since $\mathbf{F}_b$ appears in the mean buoyancy equation (4.13) inside the divergence operator. In general, we have

$$\mathbf{F}_b = \kappa\nabla\overline{b} - \psi^*\underset{\neg}{\nabla}\overline{b} - \underset{\neg}{\nabla}\theta \ . \tag{4.15}$$

Using Eq. (4.15), we obtain for the buoyancy budget (4.13),

$$v_{res}\partial_y\overline{b} + w_{res}\partial_z\overline{b} = \overline{Q} - L_x^{-1}\nabla\cdot\left(\kappa\nabla\overline{b}\right) \ , \tag{4.16}$$

where the residual velocities $v_{res} = \overline{v} - L_x^{-1}\partial_z\psi^*$ and $w_{res} = \overline{w} + L_x^{-1}\partial_y\psi^*$ represent the total advection velocities of $\overline{b}$. Hence, the residual streamfunction ψ_{res} is given by

$$\psi_{res} = \overline{\Lambda} + \psi^* \ . \tag{4.17}$$

ψ^* is the eddy streamfunction and defines the eddy-driven velocities

$$v^* = -L_x^{-1}\partial_z\psi^* \ , \qquad w^* = L_x^{-1}\partial_y\psi^* \ , \tag{4.18}$$

while the flux component $\kappa\nabla\overline{b}$ corresponds to a diffusive flux, and therefore the coefficient κ represents the diapycnal diffusivity induced by meso-scale eddies. Note that, since $\overline{b}$ does not retain the volumetric properties of the unaveraged buoyancy field b, the effect of eddies on $\overline{b}$ is inevitably both advective and diffusive (in contrast to isopycnal averaging, Nurser and Lee (2004b)).

The time-zonal-mean buoyancy $\overline{b}$ in Eq. (4.16) is forced by the small-scale diabatic forcing $\overline{Q}$ and the convergence of the meso-scale diffusive eddy flux $-L_x^{-1}\nabla\cdot\left(\kappa\nabla\overline{b}\right)$. In order to ensure that, if there is no instantaneous diabatic buoyancy forcing Q, there is also no diabatic effects in the mean buoyancy budget, we have to consider the rotational eddy fluxes.

While the choice of θ has no influence on the mean buoyancy equation[15], it affects the eddy streamfunction ψ^* and the diapycnal diffusivity κ,

$$\psi^* = -\frac{(\mathbf{F}_b + \underset{\neg}{\nabla}\theta)\cdot\underset{\neg}{\nabla}\overline{b}}{|\nabla\overline{b}|^2} \ , \qquad \kappa = \frac{(\mathbf{F}_b + \underset{\neg}{\nabla}\theta)\cdot\nabla\overline{b}}{|\nabla\overline{b}|^2} \ . \tag{4.19}$$

[15] More precisely, the sum of the additional eddy advection term $-\underset{\neg}{\nabla}(\underset{\neg}{\nabla}\theta\cdot\underset{\neg}{\nabla}\overline{b}/|\nabla\overline{b}|^2)\cdot\nabla\overline{b}$ and the additional eddy diffusion term $\nabla\cdot(\underset{\neg}{\nabla}\theta\cdot\nabla\overline{b}/|\nabla\overline{b}|^2\nabla\overline{b})$ identically vanishes.

Further, the choice of the gauge potential θ affects the conservation equation of eddy variance $\overline{\phi_2} = \overline{b'b'}/2$, which is given by

$$\nabla \cdot \mathbf{F_2} = -\mathbf{F}_b \cdot \nabla\bar{b} + L_x\overline{b'Q'} \ , \tag{4.20}$$

where $\mathbf{F_2} = L_x(\overline{v}\overline{\phi_2} + \overline{v'\phi_2}, \overline{w}\overline{\phi_2} + \overline{w'\phi_2})$ represents the total variance flux, consisting of mean and turbulent variance advection. The term $\overline{b'Q'}$ denotes dissipation of variance and the term $-\mathbf{F}_b \cdot \nabla\bar{b} = -\kappa|\nabla\bar{b}|^2 + \nabla\!\!\!\!\urcorner\,\theta \cdot \nabla\bar{b}$ is a variance production term. The first term is positive for $\kappa > 0$ and hence a source of variance, while the second term can have both signs.

By considering the analog budgets of the higher order buoyancy moments, defined as $\overline{\phi_n} = \overline{b'^n}/n$ for order n, and applying decompositions of the corresponding fluxes $\mathbf{F}_n = L_x(\overline{v}\overline{\phi_n} + \overline{v'\phi_n}, \overline{w}\overline{\phi_n} + \overline{w'\phi_n})$ analog to Eq. (4.15), i.e. $\mathbf{F}_n = \kappa_n\nabla\bar{b} - \psi_n^*\nabla\!\!\!\!\urcorner\,\bar{b} - \nabla\!\!\!\!\urcorner\,\theta_n$, Eden et al. (2007) are able to show that, if the rotational flux potentials are specified as $n\theta_n = \psi_{n+1}^*$, then the turbulent diffusivity κ of Eq. (4.19) is given by the series

$$\kappa|\nabla\bar{b}|^2 = L_x\overline{b'Q'} - \mathcal{D}(L_x\overline{\phi_2 Q}) + \frac{1}{2}\mathcal{D}^2(L_x\overline{\phi_3 Q}) - \frac{1}{3!}\mathcal{D}^3(L_x\overline{\phi_4 Q}) + \ldots \ , \tag{4.21}$$

where $\mathcal{D}() \equiv \nabla \cdot \nabla\bar{b}|\nabla\bar{b}|^{-2}()$. In Eq. (4.21) κ is related to covariances between the small-scale forcing or mixing and buoyancy fluctuations. Hence, by specifying the gauge potentials as $n\theta_n = \psi_{n+1}^*$, there is no diapycnal turbulent mixing if there is no molecular mixing. The gauge condition $\theta = \psi_2^*$ states that the rotational flux potential is given by the flux of variance circulating along the contours of $\bar{b}$ (where ψ_2^* is affected by the rotational flux potential of eddy variance θ_2).

Using $\psi_n^*|\nabla\bar{b}|^2 = -(\mathbf{F}_n + \nabla\!\!\!\!\urcorner\,\theta_n) \cdot \nabla\!\!\!\!\urcorner\,\bar{b}$ and the gauge condition $n\theta_n = \psi_{n+1}^*$, we obtain for the eddy streamfunction ψ^*,

$$\psi^*|\nabla\bar{b}| = -J_1 + \partial_m J_2 - \frac{1}{2}\partial_m^2 J_3 + \frac{1}{3!}\partial_m^3 J_4 - \ldots \ , \tag{4.22}$$

where $\partial_m() \equiv |\nabla\bar{b}|^{-1}\nabla\bar{b} \cdot \nabla|\nabla\bar{b}|^{-1}()$ and the $J_n \equiv \mathbf{F}_n \cdot \nabla\!\!\!\!\urcorner\,\bar{b}|\nabla\bar{b}|^{-1}$ represent the along-isopycnal fluxes of the eddy buoyancy moments. The first order term in the expansion for ψ^* is identical to an eddy streamfunction of the transformed Eulerian mean (TEM) framework (Andrews and McIntyre, 1976, 1978b), i.e. the decomposition of $\mathbf{F}_b$ with $\nabla\!\!\!\!\urcorner\,\theta \equiv 0$. The remainder of the expansion is due to the introduction of the rotational flux potential θ

given by

$$\theta|\nabla\overline{b}| = -J_2 + \frac{1}{2}\partial_m J_3 - \frac{1}{3!}\partial_m^2 J_4 + ... \ . \tag{4.23}$$

In the ocean interior, it typically holds $|\partial_y\overline{b}| \ll |\partial_z\overline{b}|$ and $|\overline{w}| \ll |\overline{v}|$ and we obtain

$$\psi^* \approx \frac{L_x\overline{v'b'}}{\partial_z\overline{b}} - \frac{1}{\partial_z\overline{b}}\partial_z\left(\frac{L_x\overline{\phi_2 v}}{\partial_z\overline{b}}\right) + \frac{1}{2}\frac{1}{\partial_z\overline{b}}\partial_z\left(\frac{1}{\partial_z\overline{b}}\partial_z\left(\frac{L_x\overline{\phi_3 v}}{\partial_z\overline{b}}\right)\right) - ... \tag{4.24}$$

$$\theta \approx \frac{L_x\overline{\phi_2 v}}{\partial_z\overline{b}} - \frac{1}{2}\frac{1}{\partial_z\overline{b}}\partial_z\left(\frac{L_x\overline{\phi_3 v}}{\partial_z\overline{b}}\right) + \frac{1}{3!}\frac{1}{\partial_z\overline{b}}\partial_z\left(\frac{1}{\partial_z\overline{b}}\partial_z\left(\frac{L_x\overline{\phi_4 v}}{\partial_z\overline{b}}\right)\right) - ... \tag{4.25}$$

$$\kappa \approx \frac{L_x\overline{b'Q'}}{(\partial_z\overline{b})^2} - \frac{1}{(\partial_z\overline{b})^2}\partial_z\left(\frac{L_x\overline{\phi_2 Q}}{\partial_z\overline{b}}\right) + \frac{1}{2}\frac{1}{(\partial_z\overline{b})^2}\partial_z\left(\frac{1}{\partial_z\overline{b}}\partial_z\left(\frac{L_x\overline{\phi_3 Q}}{\partial_z\overline{b}}\right)\right) - ... \tag{4.26}$$

4.7.2 The quasi-Stokes streamfunction

We assume that the buoyancy field $b(x, y, z, t)$ is vertically strictly monotonic in the interior of the ocean. The instantaneous isopycnal b_a lies at an instantaneous height $z(x, y, b_a, t) = z_a(y, b_a) + z'_a(x, y, b_a, t)$, where z_a is the time-zonal-mean height of b_a and z'_a is the deviation from the time-zonal-mean, i.e. $\overline{z'_a} = 0$. The time-zonal-mean isopycnal streamfunction $\overline{\psi_I}$ is the temporally averaged zonal and depth integral of the velocity v, integrated below the isopycnal b_a. We may write

$$\overline{\psi_I}(y, b_a) = -L_x\overline{\int_{bottom}^{z_a+z'_a} v \ dz} \ . \tag{4.27}$$

$\overline{\psi_I}$ may be transformed to Eulerian space by identifying each b_a with its mean height z_a. Therewith, the quasi-Stokes streamfunction Ψ^* is defined via the decomposition

$$-L_x\overline{\int_{bottom}^{z_a+z'_a} v \ dz} = \overline{\Lambda}(y, z_a) + \Psi^*(y, z_a) \ , \tag{4.28}$$

that is,

$$\Psi^*(y, z_a) \equiv -L_x\overline{\int_{z_a}^{z_a+z'_a} v \ dz} \ , \tag{4.29}$$

and gives the transport of $\overline{\psi_I}$ related to the perturbation z'_a. Ψ^* is the eddy-induced streamfunction of $\overline{\psi_I}$ in Eulerian space[16]. Approximations of both z' and Ψ^* by Eulerian mean quantities may be obtained by expanding b and v in Taylor series (McDougall and McIntosh, 2001; Nurser and Lee, 2004b).

A vertical Taylor series of b centered at $z = z_a$ gives

$$b_a = b(z_a + z'_a) = b(z_a) + z'_a \partial_z b|_{z=z_a} + \frac{1}{2}(z'_a)^2 \partial_z^2 b|_{z=z_a} + \frac{1}{6}(z'_a)^3 \partial_z^3 b|_{z=z_a} + ...$$

Using the decomposition $b = \overline{b} + b'$, we obtain as terms up to third order in perturbation quantities (denoted by a)

$$\begin{aligned} b(z_a + z'_a) = \overline{b}(z_a) + b'(z_a) + z'_a \partial_z \overline{b}|_{z=z_a} + z'_a \partial_z b'|_{z=z_a} + \frac{1}{2}(z'_a)^2 \partial_z^2 \overline{b}|_{z=z_a} + \\ + \frac{1}{2}(z'_a)^2 \partial_z^2 b'|_{z=z_a} + \frac{1}{6}(z'_a)^3 \partial_z^3 \overline{b}|_{z=z_a} + O(a^4) \end{aligned}$$

Taking the temporal and zonal average of this equation yields

$$b_a = \overline{b}(z_a) + \overline{z'_a \partial_z b'|_{z=z_a}} + \frac{1}{2}\overline{(z'_a)^2} \partial_z^2 \overline{b}|_{z=z_a} + \frac{1}{2}\overline{(z'_a)^2 \partial_z^2 b'|_{z=z_a}} + \frac{1}{6}\overline{(z'_a)^3} \partial_z^3 \overline{b}|_{z=z_a} + O(a^4)$$

The difference of both equations gives

$$\begin{aligned} -z'_a \partial_z \overline{b}|_{z=z_a} &= b'(z_a) + z'_a \partial_z b'|_{z=z_a} - \overline{z'_a \partial_z b'|_{z=z_a}} + \frac{1}{2}\big((z'_a)^2 - \overline{(z'_a)^2}\big) \partial_z^2 \overline{b}|_{z=z_a} \\ &\quad + \frac{1}{2}(z'_a)^2 \partial_z^2 b'|_{z=z_a} - \frac{1}{2}\overline{(z'_a)^2 \partial_z^2 b'|_{z=z_a}} + \frac{1}{6}\big((z'_a)^3 - \overline{(z'_a)^3}\big) \partial_z^3 \overline{b}|_{z=z_a} + O(a^4) \end{aligned}$$

From this last equation we obtain[17] a series expansion of z' (extending the approximation of McDougall and McIntosh (2001) about two orders),

$$\begin{aligned} z' &= -\frac{b'}{\partial_z \overline{b}} + \frac{1}{\partial_z \overline{b}} \partial_z \left(\frac{\phi_2}{\partial_z \overline{b}} \right) - \frac{L_x^{-1}}{\partial_z \overline{b}} \partial_z \left(\frac{L_x \overline{\phi_2}}{\partial_z \overline{b}} \right) + \frac{L_x^{-1}}{\partial_z \overline{b}} \partial_z \left(\frac{b'}{\partial_z \overline{b}} \right) \partial_z \left(\frac{L_x \overline{\phi_2}}{\partial_z \overline{b}} \right) - \\ &\quad - \frac{1}{2} \frac{1}{\partial_z \overline{b}} \partial_z \left(\frac{1}{\partial_z \overline{b}} \partial_z \left(\frac{\phi_3}{\partial_z \overline{b}} \right) \right) + \frac{1}{2} \frac{L_x^{-1}}{\partial_z \overline{b}} \partial_z \left(\frac{1}{\partial_z \overline{b}} \partial_z \left(\frac{L_x \overline{\phi_3}}{\partial_z \overline{b}} \right) \right) + O(b'^4) \end{aligned} \tag{4.30}$$

By expanding v in a vertical Taylor series, we obtain for the quasi-Stokes streamfunction

[16] In Viebahn and Eden (2012) the corresponding decomposition is defined in an isopycnal framework.

[17] Note that if the topography varies vertically, then the zonal average and the vertical derivative do not commute due to the depth-dependent factor L_x.

Ψ^*,

$$\begin{aligned}\Psi^* &= -L_x\Big(\overline{v(z_a)z'_a} + \frac{1}{2}\overline{(z'_a)^2\partial_z v|_{z=z_a}} + \frac{1}{6}\overline{(z'_a)^3\partial_z^2 v|_{z=z_a}} + ...\Big) \qquad (4.31)\\ &= -L_x\Big(\overline{v'(z_a)z'_a} + \frac{1}{2}\overline{(z'_a)^2}\partial_z\overline{v}|_{z=z_a} + \frac{1}{2}\overline{(z'_a)^2\partial_z v'|_{z=z_a}} + \frac{1}{6}\overline{(z'_a)^3}\partial_z^2\overline{v}|_{z=z_a} + \frac{1}{6}\overline{(z'_a)^3\partial_z^2 v'|_{z=z_a}} + ...\Big)\ ,\end{aligned}$$

where we used the decomposition $v = \overline{v} + v'$. Using Eq. (4.30) in Eq. (4.31), we obtain up to third order in perturbation quantities (extending the approximation of McDougall and McIntosh (2001) about one order)

$$\Psi^* = \Psi^*_1 + \Psi^*_2 + \Psi^*_3 + O(a^4)\ , \qquad (4.32)$$

where

$$\begin{aligned}\Psi^*_1 &\equiv 0 \qquad (4.33)\\ \Psi^*_2 &= \frac{L_x\overline{b'v'}}{\partial_z\overline{b}} - \frac{L_x\overline{\phi_2}\partial_z\overline{v}}{(\partial_z\overline{b})^2} \qquad (4.34)\\ \Psi^*_3 &= -\frac{1}{\partial_z\overline{b}}\partial_z\left(\frac{L_x\overline{\phi_2 v'}}{\partial_z\overline{b}}\right) + \frac{1}{2}\frac{\partial_z\overline{v}}{(\partial_z\overline{b})^2}\partial_z\left(\frac{L_x\overline{\phi_3}}{\partial_z\overline{b}}\right) + \frac{1}{2}\frac{1}{\partial_z\overline{b}}\partial_z\left(\frac{L_x\overline{\phi_3}\partial_z\overline{v}}{(\partial_z\overline{b})^2}\right) \qquad (4.35)\end{aligned}$$

In order to make the relation between Ψ^* and the residual-mean eddy streamfunction ψ^* (see (4.24)) more obvious, we arrange the expansion of Ψ^* in orders of buoyancy perturbations b' (extending the approximation of Nurser and Lee (2004b) and of Eq. (4.32)),

$$\Psi^* = \Psi^*_I + \Psi^*_{II} + \Psi^*_{III} + O(b'^4)\ , \qquad (4.36)$$

where

$$\begin{aligned}\Psi^*_I &= \frac{L_x\overline{b'v'}}{\partial_z\overline{b}} = \psi^*_I \qquad (4.37)\\ \Psi^*_{II} &= -\frac{1}{\partial_z\overline{b}}\partial_z\left(\frac{L_x\overline{\phi_2 v}}{\partial_z\overline{b}}\right) + \frac{\overline{v}}{\partial_z\overline{b}}\partial_z\left(\frac{L_x\overline{\phi_2}}{\partial_z\overline{b}}\right) = \psi^*_{II} + \psi^*_{\Delta II} \qquad (4.38)\\ \Psi^*_{III} &= \frac{1}{2}\frac{1}{\partial_z\overline{b}}\partial_z\left(\frac{1}{\partial_z\overline{b}}\partial_z\left(\frac{L_x\overline{\phi_3 v}}{\partial_z\overline{b}}\right)\right) - \frac{1}{2}\frac{\overline{v}}{\partial_z\overline{b}}\partial_z\left(\frac{1}{\partial_z\overline{b}}\partial_z\left(\frac{L_x\overline{\phi_3}}{\partial_z\overline{b}}\right)\right) - \frac{L_x^{-1}}{\partial_z\overline{b}}\partial_z\left(\frac{L_x\overline{\phi_2}}{\partial_z\overline{b}}\right)\partial_z\left(\frac{L_x\overline{v'b'}}{\partial_z\overline{b}}\right)\\ &= \psi^*_{III} + \psi^*_{\Delta IIIa} + \psi^*_{\Delta IIIb} \qquad (4.39)\end{aligned}$$

5 Synthesis

The first research paper of this PhD thesis (chapter 2) addresses crucial questions of the present climate change debate, namely: How does the MOC in the SO respond to decadal-scale trends in wind stress forcing? And: To what extent are up-to-date eddy diffusivity parameterisations able to represent the corresponding changes in the eddy field in climate models?

Therefore, in a first step, the results of an eddy-permitting idealised numerical model of the SO (at 5 km horizontal resolution) were used. It was found that the MOC strengthens with increasing wind stress. The wind-driven component $\overline{\psi}$ is increasing nearly linearly according to the increase in wind stress, whereas the (absolute) increase of the eddy-driven component ψ^* amplifies with increasing wind stress. Consequently, the sensitivity of the MOC on wind stress can be described by three aspects, termed as *eddy compensation effect*, namely, the general behaviour of ψ^* to oppose $\overline{\psi}$ such that (*i*) the absolute value and (*ii*) the increase of the MOC are generally smaller compared to $\overline{\psi}$ and (*iii*) the increase of the MOC reduces with amplifying winds. Furthermore, magnitude and depth of the MOC are correlated. Aspect (*iii*) opens the possibility, that the MOC may become completely insensitive to wind stress. However, for the considered wind stress range a state of total compensation between $\overline{\psi}$ and ψ^* is not reached but the MOC is still significantly increasing for increasing wind stress.

The corresponding eddy diffusivity K is characterised by a manifold spatial structure and by a strong sensitivity towards changing winds: K increases with increasing wind stress and, similar to the MOC, the increase of K (averaged at 200 m depth) diminishes monotonically with increasing wind stress for the wind stress range under consideration. Consequently, the sensitivity of the eddy diffusivity K to wind stress has to be distinguished from the corresponding response of the eddy-driven component ψ^*. It turns out that a nearly constant increase of the isopycnal slopes s, though quantitatively much smaller than the increase of the eddy diffusivity K, is relevant in order to capture the correct sensitivity to wind stress of ψ^*.

In a second step, the Gent and McWilliams (1990) parameterisation was implemented in the idealised numerical model of the SO in order to assess the effect of parameterising the meso-scale eddy field on the residual MOC of the SO. On the one hand, the eddy diffusivity K was specified by different constant values; on the other hand, the flow-interactive meso-scale eddy closure by Eden and Greatbatch (2008) (EG) was implemented and it was found: The EG closure represents well the spatial structure of K and its qualitative response to increasing wind stress which is, however, quantitatively underestimated. The latter effect becomes even more clear for constant eddy diffusivity parameterisations, since they lack any sensitivity by definition. Consequently, for both, the EG closure and any constant K, there are wind stress ranges of over- or underestimation of the eddy diffusivity K. Furthermore, the eddy diffusivity and isopycnal slopes are intimately linked in the parameterised models as well: The underestimated response of K corresponds an overestimated response of s, such that for all parameterisations the response of the eddy-driven MOC of the eddying model tends to be underestimated by the parameterised eddy-driven MOCs.

The overall MOC behaves accordingly in the parameterised models: All parameterisations reproduce the MOC for a fixed wind stress qualitatively well. However, the response of the MOC towards increasing winds is overestimated by each parameterisation, with the EG closure being slightly more adequate than a constant K. Consequently, each parameterisation will always under- or overestimate the residual MOC in a certain wind stress range.

The results of the first research paper (chapter 2) clearly demonstrate that the correct behaviour of the eddy diffusivity in coarse-resolution climate models is essential for a correct simulation of changes in the SO and thus a thorough assessment of climate change. In particular, the simulation of the MOC and the related CO_2 content in the SO and its response to changing winds depends crucially on the subgrid-scale parameterisation. Up-to-date eddy diffusivity parameterisations lead to under- or overestimations of the MOC and the related CO_2 content in the SO for different wind stresses. The results strengthen the necessity of further improvements of meso-scale eddy diffusivity parameterisations.

The second research paper (chapter 3) and the third research paper (chapter 4) of this PhD thesis are guided by a more conceptual perspective. They focus on the concept of a MOC streamfunction and explore difficulties and possible optimisations of the most prominent definitions of the MOC streamfunction: Is it possible to define a MOC streamfunction completely void of standing eddies? What are the differences between the series expansion of the residual-mean eddy streamfunction and the series expansion of the quasi-

Stokes streamfunction and how applicable are the approximate formulas of both in order to diagnose the MOC?

The second research paper (chapter 3) addresses the first question. Previous studies suggest that zonal integration should be performed along time-mean horizontal streamlines in order to exclude standing eddies in the MOC streamfunction. However, it turns out that time-mean horizontal streamlines represent only an approximate solution. Exact time-mean horizontal streamlines may be used as zonal integration paths in the construction of a zonal-mean meridional streamfunction only, in case they are closed above topography (i.e. the horizontal velocity field is nondivergent), because otherwise mass balance is not guaranteed. It is showed that if time-mean horizontal streamlines are both closed and depth-independent, the time-mean of the meridional cross-streamline transport velocity will vanish. It follows that under such conditions the entire time-mean component of the MOC streamfunction (including the standing eddy part) exactly vanishes. However, as demonstrated by results of the idealised numerical model of the SO, time-mean horizontal streamlines generally are unclosed in the surface layer (due to the wind-driven Ekman transport) and significantly change with depth. Consequently, zonal integration along time-mean horizontal geostrophic streamlines may only lead to a reduction, but not to an exact vanishing of the standing eddy component of the MOC streamfunction: On the one hand, streamlines have to be approximated by the isolines of a scalar field, e.g. the geostrophic streamfunction, such that in regions of dominant ageostrophic transports a significant standing eddy component may appear. On the other hand, the significant depth-dependence of the (geostrophic) streamlines induces a non-orthogonality term with non-vanishing time-mean in the meridional cross-streamline transport velocity, which may lead to an additional significant contribution in the standing eddy component.

However, an optimisation could be given in the second research paper (chapter 3): It is formally showed that the construction of a zonal-mean meridional streamfunction with an exactly vanishing standing eddy part has to be performed by zonal integration along depth-dependent horizontal isolines of time-mean buoyancy. Isolines of time-mean buoyancy are always closed above topography and hence do not conflict with mass balance and may be used without approximation. Moreover, the vanishing of the standing eddy part in this case relies only on the integration conditions. It is independent of the determination of the cross-path transport velocity and therefore always exactly holds - even for a depth-dependent isolines of time-mean buoyancy, which induce a non-orthogonal curvilinear coordinate system. However, the time-mean of the cross-path transport velocity and

hence the time-zonal-mean part (the Eulerian part) of the overall MOC do not vanish in general.

Finally, in the third research paper (chapter 4) the series expansion of the residual-mean eddy streamfunction ψ^* and the Taylor expansion of the quasi-Stokes streamfunction Ψ^* are considered up to third order in buoyancy perturbation b'.

Formally, the series expansions of ψ^* and Ψ^* increasingly differ from each other with increasing order. While the first order terms are identical, the difference between the second order terms is related to the time-zonal-mean meridional velocity $\overline{v}$. Since $\overline{v}$ is generally small in a zonal channel, the second order difference may be expected to be small there as well. The third order difference is constituted by a corresponding term related to $\overline{v}$ and an additional term, which is related to the velocity perturbation v' and, hence, is of fourth order in perturbation quantities b' and v'. For orders higher than three it is likely that further types of terms related to v' emerge. Regarding a zonal channel, it is likely that the terms related to v' primarily need to be considered in order to distinguish between ψ^* and Ψ^*.

This expectation is confirmed in different idealised model experiments of the SO which include either a flat bottom or a hill-like topographic feature. In each experiment the third order difference term related to v' shows the largest magnitudes. Hence, at least initially and in regions of significant values, the magnitudes of the differences between ψ^* and Ψ^* tend to increase with higher order. Significant differences between the terms of the series expansion of ψ^* and the Taylor series of Ψ^* are present in the diabatic boundary regions of the flat bottomed experiments, while in the presence of topography differences are also found in the ocean interior (around hill depth and above). In the flat bottomed experiments, this is in accordance with the expectation that both streamfunctions largely coincide in the nearly adiabatic interior, since the corresponding mean buoyancy distributions largely coincide there (Nurser and Lee (2004a), see also chapter 3). Finally, it is found that the terms of Ψ^* generally tend to have smaller magnitudes than the corresponding terms of ψ^*, which might indicate that the series expansion of Ψ^* converges faster than that of ψ^*.

However, despite significant differences in certain regions, the series expansion of ψ^* and the Taylor series of Ψ^*, considered up to the third order in the different idealised SO model experiments, show the same behaviour in several aspects: Both series expansions generally tend to be of alternating character, such that the next higher order always compensates a part of the previous order. Furthermore, in the experiments with a flat bottom, both series

expansions may be adequately approximated by low order terms in the ocean interior, since there they appear to be decreasing with higher order. Nevertheless, including terms up to the third order still significantly improves the interior circulations in the flat experiments, in the sense that they further approach the corresponding circulation patterns of the isopycnal streamfunction and that streamlines become more aligned along the mean isopycnals in the ocean interior.

In contrast, in the diabatic boundary regions both series expansions are alternating and increasing, which rules an adequate approximation by low order terms out, as previously discussed by Killworth (2001); McDougall and McIntosh (2001); Nurser and Lee (2004b). This intractable behaviour becomes more pronounced and severe in the experiment with bottom topography. There, physically inconsistent recirculation cells appear around the hill depth in the first order MOC, which are not effectively reduced by the inclusion of next higher order terms. On the contrary, the magnitude of the next higher order terms now even is increasing in the ocean interior (around hill depth and above topography), which further intensifies the recirculation cells and complicates the circulation patterns. Consequently, in the model experiment which is equipped with a significant topographic feature and which hence represents the most realistic model setup, the approximation of the ocean interior circulation by low order terms seems not to be possible. Therefore, the diagnosis of the MOC from empirical data or realistic model results via approximations of the zonal-mean streamfunctions ψ^* and Ψ^* must be treated with care or even completely ruled out.

Author contributions

The author contributions to the main chapters 2, 3 and 4 are the following:
Jan Viebahn performed all experiments, calculations, figures and wrote the manuscripts.
Carsten Eden contributed to discussions, the design of the research and commented on the manuscripts.

List of Figures

1.1 Empirical estimate of the world ocean heat content for 1955-2008 from Levitus et al. (2009). 3

1.2 Strongly simplified sketch of the global overturning circulation system from Kuhlbrodt et al. (2007). The circulation that leads to a continuous renewal of the waters in the deep ocean by the sinking of dense waters to the abyssal ocean at high latitudes in the North Atlantic (L, N) and near Antarctica (W, R), and by widespread upwelling of these watermasses elsewhere is called global MOC. Wind-driven upwelling occurs along the Antarctic Circumpolar Current (ACC). The MOC is considered to be crucial in the climate system e.g. due to its role in the poleward heat transport and the ventilation of the deep ocean. 4

1.3 (A) Column inventories and (B) air-sea fluxes of anthropogenic carbon simulated in an ocean-climate model by Caldeira and Duffy (2000). Maximum air-sea fluxes of anthropogenic carbon into the Southern Ocean occur farther south than maximum column inventories. Note that the column inventories are in good agreement with empirical estimates e.g. by Sabine et al. (2004). 6

1.4 Seasonal values of the SAM index calculated from station data (updated by the IPCC (2007) from Marshall (2003)). The smooth black curve shows decadal variations. Enhanced SO westerlies occur in the positive phase of the SAM. 10

2.1 Schematic representation of the MOC of the SO. Further details are given in the text. Redrawn from Olbers and Visbeck (2005). 19

2.2 Left: target buoyancy $b^*/\Delta b$ for the surface restoring boundary condition and different wind forcings T_i/τ_1 imposed in the idealised ACC model. Middle: zonal velocity at the surface from the idealised ACC model for $\tau_1 = 0.5 \times 10^{-4} m^2 s^{-2}$ (contour interval is $0.15 m s^{-1}$). Right: maxima of the residual streamfunction ψ_{res} [Sv] at $200m$ depth in the ACC part for a 1-year-mean (green), 5-year-mean (blue), and a 15-year mean (thick red) for increasing wind stresses $\tau_2 = 1 \times 10^{-4} m^2 s^{-2}$, $\tau_3 = 1.5 \times 10^{-4} m^2 s^{-2}$, and $\tau_5 = 2.5 \times 10^{-4} m^2 s^{-2}$. 29

2.3 Zonal and time mean (upper left) Eulerian ($\overline{\psi}$), (upper right) eddy (ψ^*) and (lower left) residual streamfunction (ψ_{res}) from the idealised ACC model for $\tau_1 = 0.5 \times 10^{-4} m^2 s^{-2}$. Contour interval is 0.2 Sv in each case and zero lines are thick. Also shown is the zonal and time mean buoyancy distribution with a contour interval of $0.001 m/s^2$ and a thick $0.007 m/s^2$ line. 31

2.4 Zonal and time mean (upper) residual streamfunctions (ψ_{res}) and (lower) buoyancy distributions ($\overline{b}$) from the eddy-permitting idealised ACC model for wind stress amplitudes (from left to right) $\tau_1 = 0.5 \times 10^{-4} m^2 s^{-2}$, $\tau_2 = 1 \times 10^{-4} m^2 s^{-2}$ and $\tau_3 = 1.5 \times 10^{-4} m^2 s^{-2}$. The contour intervals are (upper) $0.2 Sv$ and (lower) 0.001 m/s^2. Thick lines are (upper) zero lines and (lower) 0.007 m/s^2 lines. 35

2.5 Left: maximal transport values [Sv] of the residual streamfunction ψ_{res}, the Eulerian streamfunction $\overline{\psi}$ and $-\tau/f$ at $-150m$ depth between the southern boundary and $y|_{\psi^*=0}$ (around $y = 1100km$) for the eddy-permitting ACC model configuration with different horizontal resolutions. Thick red: ψ_{res} for ΔR_1, magenta dashed: ψ_{res} for ΔR_2, magenta dash-dot: ψ_{res} for ΔR_3, thin red: $\overline{\psi}$ for ΔR_1, blue dashed: $\overline{\psi}$ for ΔR_2, blue dash-dot: $\overline{\psi}$ for ΔR_3, thin black: $-\tau/f$. Black dots denote data points. Right: the corresponding mean eddy diffusivities $\overline{K}$ [$10^3 m^2/s$] and isopycnal slopes $\overline{s}$ [-10^{-3}]. Averages are taken at $-200m$ depth and between $110km$ and $910km$. 36

2.6 Zonal and time mean eddy diffusivity K [m^2/s] for three different wind stress amplitudes (from left to right) $\tau_1 = 0.5 \times 10^{-4} m^2 s^{-2}$, $\tau_2 = 1 \times 10^{-4} m^2 s^{-2}$ and $\tau_3 = 1.5 \times 10^{-4} m^2 s^{-2}$ from (upper) the eddy-permitting idealised model and the parameterised idealised ACC model using the closure of Eden and Greatbatch (2008), given by (2.12), with (middle) $c = 4$ and (lower) $c = 2$. The contour intervals are $250 m^2/s$ and the $2500 m^2/s$ line is thick. 39

2.7 Zonal and time mean (upper) residual streamfunctions (ψ_{res}), (middle) buoyancy distributions ($\overline{b}$) and (lower) eddy diffusivities (K) from the idealised ACC model for $\tau_2 = 1 \times 10^{-4} m^2 s^{-2}$ with different horizontal resolutions (from left to right): $\Delta R_1 = 5km$, $\Delta R_2 = 10km$, $\Delta R_1 = 20km$. The contour intervals are (upper) $0.2Sv$, (middle) $0.001\ m/s^2$ and (lower) $250m^2/s$. Thick lines are (upper) zero lines, (middle) $0.007\ m/s^2$ lines and (lower) $2500m^2/s$ lines. 40

2.8 Mean (left) eddy diffusivities $\overline{K}$ $[10^3 m^2/s]$ and (middle, right) isopycnal slopes $\overline{s}$ $[-10^{-3}]$ for the different idealised ACC model configurations. Averages are taken at $-200m$ depth and between $110km$ and $910km$. Red: eddy-permitting reference case ΔR_1, blue thick: K_{EG1}, blue dashed: K_{EG2}, blue dash-dot: K_{EG3}, blue thin: K_{EG4}, blue dotted: K_{EG5}, black thick: K_{1000}, black dashed: K_{2000}, black dash-dot: K_{3000}, black thin: K_{4000}, black dotted: K_{5000}. Left black dotted lines denote the corresponding constant eddy diffusivities. 43

2.9 Zonal and time mean residual streamfunctions (ψ_{res}) from the idealised ACC model for $\tau_2 = 1 \times 10^{-4} m^2 s^{-2}$ and different model configurations: K_{EG1} (upper left), K_{EG3} (upper right), K_{1000} (lower left), K_{3000} (lower right). The contour intervals are $0.2Sv$ and zero lines are thick. 44

2.10 Percentages of the transport values of (left) the residual streamfunction ψ_{res} and (right) the eddy streamfunction $\psi^*_{para} \equiv Ks$ at $150m$ depth and $y = 970km$, from the parameterised idealised ACC model using (blue) the closure of Eden and Greatbatch (2008), given by (2.12), and (magenta) using constant eddy diffusivities. Values are taken relative to the eddy-permitting reference setup ΔR_1 (red line). Blue thick: K_{EG1}, blue dashed: K_{EG2}, blue dash-dot: K_{EG3}, blue thin: K_{EG4}, blue dotted: K_{EG5}, magenta thick: K_{1000}, magenta dashed: K_{2000}, magenta dash-dot: K_{3000}, magenta thin: K_{4000}, magenta dotted: K_{5000}. 45

2.11 Zonal and time mean residual streamfunctions (ψ_{res}) from (upper) the eddy-permitting idealised ACC model for case ΔR_3 and from the application of equation (2.16) with (middle) an eddy diffusivity diagnosed from the eddy-permitting model and (lower) prescribing a fixed eddy diffusivity of $1000m^2/s$. The wind stress amplitudes are (left) $\tau_1 = 0.5 \times 10^{-4}m^2s^{-2}$, (right) $\tau_2 = 1 \times 10^{-4}m^2s^{-2}$ and in between $\tau = 0.75 \times 10^{-4}m^2s^{-2}$. The contour intervals are $0.2Sv$ and zero lines are thick. 49

3.1 Top: Time-mean Eulerian meridional streamfunction ($\overline{\Lambda}$) with a contour interval of 1 Sv and thick zero lines for the flat (a) and the hill (b) case. Bottom: Eulerian zonal- and time-mean buoyancy distribution ($[\overline{b}]$) with a contour interval of $0.001m/s^2$ and a thick $0.007m/s^2$ line for the flat (c) and the hill (d) case. 58

3.2 The isopycnal streamfunction ($\overline{\psi_I}$) in (top) isopycnal coordinates and (bottom) transformed to depth coordinates via the mean height of isopycnals (Nurser and Lee, 2004a) for the flat (a,c) and the hill (b,c) case. The contour interval is 0.5 Sv and zero lines are thick. 60

3.3 The difference (multiplied by 10^3) between the time-mean of the isopycnally averaged buoyancy and $[\overline{b}]$ (shown in Fig. 3.1) for the flat (a) and the hill (b) case. The contour interval is $0.2m/s^2$ and zero lines are thick. 62

3.4 Top: The standing eddy streamfunction ($\hat{\psi}_I^*$) for the flat (a) and the hill (b) case. Bottom: The transient eddy streamfunction ($\tilde{\psi}_I^*$) for the flat (c) and the hill (d) case. The contour interval is 0.5 Sv and zero lines are thick. They were transformed to depth coordinates via the mean height of the respective isopycnals (Nurser and Lee, 2004a). 64

3.5 Time-mean horizontal streamlines in the SO region for (top) the flat case at $z = -25$m (a), $z = -75$m (b), $z = -1875$m (c) and (bottom) the hill case at $z = -25$m (d), $z = -75$m (e), $z = -825$m (f). In each case streamlines with a starting point at $x = 0$ and $y = 290$km, 610km, 970km are black and thick. 68

3.6 Top: Time-mean geostrophic streamfunction $\overline{p}/f_0$ [$10^5\ m^2/s$] of the hill case at $z = -25$m with a contour interval of $5 \times 10^3\ m^2/s$ (a), $z = -975$m with a contour interval of $1 \times 10^3\ m^2/s$ (b) and $z = -1525$m with a contour interval of $5 \times 10^2\ m^2/s$ (c). Bottom: Time-mean buoyancy $\overline{b}$ [$10^{-3}\ m/s^2$] of the hill case at $z = -25$m with a contour interval of $1 \times 10^{-3}\ m/s^2$ (d), $z = -975$m with a contour interval of $2 \times 10^{-2}\ m/s^2$ (e) and $z = -1525$m with a contour interval of $2 \times 10^{-1}\ m/s^2$ (f). 70

3.7 Standing eddy streamfunctions $\hat{\psi}^*_I$ for zonal integration along time-mean geostrophic streamlines (a-c) and isolines of time-mean buoyancy $\overline{b}$ (d-f). Eulerian streamfunctions $\overline{\Lambda}_I$ for zonal integration along time-mean geostrophic streamlines (g-i) and isolines of time-mean buoyancy $\overline{b}$ (j-l). From left to right the contour-depths are given by $z = -25$m, $z = -475$m and $z = -925$m. 73

3.8 Isopycnal streamfunctions $\overline{\psi_I}$ for zonal integration along time-mean geostrophic streamlines (a-c) and isolines of time-mean buoyancy $\overline{b}$ (d-f). Transient eddy streamfunctions $\tilde{\psi}^*_I$ for zonal integration along time-mean geostrophic streamlines (g-i) and isolines of time-mean buoyancy $\overline{b}$ (j-l). From left to right the contour-depths are given by $z = -25$m, $z = -475$m and $z = -925$m. 76

3.9 The difference (multiplied by 10^3) between the time-mean of the isopycnally and along time-mean contours averaged buoyancy distribution and the isopycnally and along latitude circles averaged buoyancy distribution. Contours are either time-mean geostrophic streamlines (a-c) or isolines of time-mean buoyancy (d-f). From left to right the contour-depths are given by $z = -25$m, $z = -475$m and $z = -925$m. The contour interval (of the plots) is $0.2m/s^2$ and zero lines are thick. 78

4.1 The first three terms of the series expansion of ψ^* for the NL case: $\psi^*_I \equiv -J_1/|\nabla\overline{b}|$ (a), $\psi^*_{II} \equiv \partial_m J_2/|\nabla\overline{b}|$ (b), $\psi^*_{III} \equiv -\frac{1}{2}\partial^2_m J_3/|\nabla\overline{b}|$ (c) and the corresponding residual streamfunctions including terms of ψ^* up to the first (d), second (e), third (f) order. The contour interval is 0.5Sv and zero lines are thick. 93

4.2 The first three terms of the series expansion of ψ^* for the flat case: ψ^*_I (a), ψ^*_{II} (b), ψ^*_{III} (c) and the corresponding residual streamfunctions including terms of ψ^* up to the first (d), second (e), third (f) order. (g-i) and (j-l) show the same quantities, but for the flat case experiment including a harmonic viscosity of $A_h = 2000\text{m}^2\text{s}^{-1}$. The contour interval is 0.5Sv and zero lines are thick. 95

4.3 The first three terms of the series expansion of ψ^* for the hill case: ψ^*_I (a), ψ^*_{II} (b), ψ^*_{III} (c) and the corresponding residual streamfunctions including terms of ψ^* up to the first (d), second (e), third (f) order. The contour interval is 0.5Sv and zero lines are thick. 98

4.4 Series number S for the NL case (a), the flat case (b) and the hill case (c). Contour lines are 0.1, 0.2, 0.4 and 1. 100

4.5 $\psi^*_{\Delta II}$, $\psi^*_{\Delta IIIa}$ and $\psi^*_{\Delta IIIb}$ for the NL case (a-c), the flat case (d-f) and the hill case (g-i). The contour interval is 0.5Sv and zero lines are thick. 104

4.6 Isopycnal streamfunction transformed to depth coordinates via the mean height of isopycnals (Nurser and Lee, 2004a) for the NL case (a), flat case (b) and hill case (c). The contour interval is 0.5Sv and zero lines are thick. Below are shown the corresponding mean isopycnals (i.e. the isopycnally averaged buoyancy distributions), where in the NL case (d) the contour interval is 0.002m/s^2, while in the flat case (e) and the hill case (f) the contour interval is 0.001m/s^2. In all three cases the 0.007m/s^2 line is thick. 107

List of Tables

2.1 Numerical constants used in the idealised numerical model in the standard configuration. 30

Bibliography

Andrews, D. G. and M. E. McIntyre, 1976: Planetary waves in horizontal and vertical shear: The generalized Eliassen-Palm relation and the zonal mean accelaration. *J. Atmos. Sci.*, **33**, 2031–2048.

Andrews, D. G. and M. E. McIntyre, 1978a: An exact theory of nonlinear waves on a Lagrangian-mean flow. *J. Fluid Mech.*, **89**, 609–646.

Andrews, D. G. and M. E. McIntyre, 1978b: Generalized Eliassen-Palm and Charney-Drazin theorems for waves on axisymmetric mean flows in compressible atmosphere. *J. Atmos. Sci.*, **35**, 175–185.

Aris, R., 1989: *Vectors, tensors, and the basic equations of fluid mechanics*. Dover.

Böning, C. W., A. Dispert, M. Visbeck, S. R. Rintoul, and F. U. Schwarzkopf, 2008: The response of the Antarctic Circumpolar Current to recent climate change. *Nature Geoscience*, **1**(12), 864–869. doi:10.1038/ngeo362.

Caldeira, K. and P. B. Duffy, 2000: The role of the Southern Ocean in uptake and storage of anthropogenic carbon dioxide. *Science*, **287**, 620–622. doi:10.1126/science.287.5453.620.

Döös, K., J. Nycander, and A. C. Coward, 2008: Lagrangian decomposition of the Deacon Cell. *J. Geophys. Res.*, **113**(C07028). doi:10.1029/2007JC004351.

Döös, K. and D. J. Webb, 1994: The Deacon Cell and the other meridional cells of the Southern Ocean. *J. Phys. Oceanogr.*, **24**(2), 429–442.

Eden, C., 2006: Thickness diffusivity in the Antarctic Circumpolar Current. *Geophys. Res. Letters*, **33**(L11606). doi:10.1029/2006GL026157.

Eden, C., 2007: Eddy length scales in the North Atlantic. *J. Geophys. Res.*, **112**(C06004). doi:10.1029/2006JC003901.

Eden, C. and R. J. Greatbatch, 2008: Towards a mesoscale eddy closure. *Ocean Modelling*, **20**, 223–239.

Eden, C., R. J. Greatbatch, and D. Olbers, 2007: Interpreting eddy fluxes. *J. Phys. Oceanogr.*, **37**, 1282–1296.

Eden, C., M. Jochum, and G. Danabasoglu, 2009a: Effects of different closures for thickness diffusivity. *Ocean Modelling*, **26**, 47–59.

Eden, C., D. Olbers, and R. J. Greatbatch, 2009b: A generalized Osborn-Cox relation. *J. Fluid Mech.*, **632**, 457–474.

England, M. H. and S. Rahmstorf, 1998: Sensitivity of ventilation rates and radiocarbon uptake to subgrid-scale mixing in ocean models. *J. Phys. Oceanogr.*, **29**, 2802–2827.

Ferreira, D. and J. Marshall, 2006: Formulation and implementation of a "residual-mean" ocean circulation model. *Ocean Modelling*, **13**, 86–107.

Ferreira, D., J. Marshall, and P. Heimbach, 2005: Estimating eddy stresses by fitting dynamics to observations using a residual-mean ocean circulation model and its adjoint. *J. Phys. Oceanogr.*, **35**, 1891–1910.

Fyfe, J. C. and O. A. Saenko, 2006: Simulated changes in the extratropical Southern Hemisphere winds and currents. *Geophys. Res. Letters*, **33**(L06701). doi:10.1029/2005GL025332.

Fyfe, J. C., O. A. Saenko, K. Zickfeld, M. Eby, and A. J. Weaver, 2007: The role of poleward-intensifying winds on Southern Ocean warming. *J. Climate*, **20**, 5391–5400.

Gent, P. R. and J. C. McWilliams, 1990: Isopycnal mixing in ocean circulation models. *J. Phys. Oceanogr.*, **20**, 150–155.

Gent, P. R., J. Willebrand, T. J. McDougall, and J. C. McWilliams, 1995: Parameterizing eddy-induced tracer transports in ocean circulation models. *J. Phys. Oceanogr.*, **25**, 463–474.

Gille, S., 1997a: The Southern Ocean momentum balance: Evidence for topographic effects from numerical model output and altimeter data. *J. Phys. Oceanogr.*, **27**, 2219–2232.

Gille, S., 1997b: Why potential vorticity is not conserved along mean streamlines in a numerical Southern Ocean. *J. Phys. Oceanogr.*, **27**, 1286–1299.

Gille, S., 2002: Warming of the Southern Ocean since the 1950s. *Science*, **295**(5558), 1275–1277.

Gille, S., 2008: Decadal-scale temperature trends in the southern hemisphere ocean. *J. Climate*, **21**, 4749–4765.

Gloor, M., N. Gruber, J. J. Sarmiento, C. L. Sabine, R. A. Feely, and C. Rödenbeck, 2003: A first estimate of present and preindustrial air-sea CO_2 flux patterns based on ocean interior carbon measurements and models. *Geophys. Res. Letters*, **30**(1), 1010. doi:10.1029/2002GL015594.

Gouretski, V. and K. Jancke, 1998: A new world ocean climatology: objective analysis on neutral surfaces. Technical Report 3, WHP Special Analysis Centre, Hamburg, Germany.

Greatbatch, R. J. and K. Lamb, 1990: On parameterizing vertical mixing of momentum in non-eddy-resolving ocean models. *J. Phys. Oceanogr.*, **20**, 1634–1637.

Green, J. S., 1970: Transfer properties of the large-scale eddies and the general circulation of the atmosphere. *Quart. J. Royal Met. Soc.*, **96**, 157–185.

Gruber, N., M. Gloor, S. E. Mikaloff Fletcher, S. C. Doney, S. Dutkiewicz, M. Follows, M. Gerber, A. R. Jacobson, F. Joos, K. Lindsay, D. Menemenlis, A. Mouchet, S. A. Müller, J. L. Sarmiento, and T. Takahashi, 2009: Oceanic sources, sinks, and transport of atmospheric CO_2. *Glob. Biochem. Cycles*, **23**(GB1005). doi:10.1029/2008GB003349.

Hallberg, B. and A. Gnanadesikan, 2001: An exploration of the role of transient eddies in determining the transport of a zonally reentrant current. *J. Phys. Oceanogr.*, **31**, 3312–3330.

Hallberg, B. and A. Gnanadesikan, 2006: The role of eddies in determining the structure and response of the wind-driven Southern Hemisphere overturning: results from the Modeling Eddies in the Southern Ocean (MESO) project. *J. Phys. Oceanogr.*, **36**, 2232–2252.

Hogg, A. M., M. P. Meredith, J. R. Blundell, and C. Wilson, 2008: Eddy heat flux in the Southern Ocean: Response to variable wind forcing. *J. Climate*, **21**, 608–620.

IPCC, 2007: Climate change 2007: The Physical Science Basis. Contribution of Working Group I to the Fourth Assessment Report of the Intergovernmental Panel on Climate Change [Solomon, S., D. Qin, M. Manning, Z. Chen, M. Marquis, K.B. Averyt, M. Tignor and H.L. Miller (eds.)]. *Cambridge University Press, Cambridge, United Kingdom and New York, NY, USA*.

Ivchenko, V. O., K. J. Richards, and D. P. Stevens, 1996: The dynamics of the Antarctic Circumpolar Current. *J. Phys. Oceanogr.*, **26**, 753–774.

Johnson, G. C. and H. L. Bryden, 1989: On the size of the Antarctic Circumpolar Current. *Deep-Sea Res.*, **36**(1), 39–53.

Karoly, D., P. C. McIntosh, P. Berrisford, T. J. McDougall, and A. C. Hirst, 1997: Similarities of the Deacon cell in the Southern Ocean and Ferrel cells in the atmosphere. *Quart. J. Royal Met. Soc.*, **123**(538), 519–526.

Karsten, R., H. Jones, and J. Marshall, 2002: The role of eddy transfer in setting the stratification and transport of a circumpolar current. *J. Phys. Oceanogr.*, **32**, 39–54.

Karsten, R. and J. Marshall, 2002: Constructing the residual circulation of the ACC from observations. *J. Phys. Oceanogr.*, **32**, 3315–3327.

Killworth, P. D., 2001: Boundary conditions on quasi-Stokes velocities in parameterizations. *J. Phys. Oceanogr.*, **31**, 1132–1155.

Kuhlbrodt, T., A. Griesel, M. Montoya, A. Levermann, M. Hofmann, and S. Rahmstorf, 2007: On the driving processes of the Atlantic meridional overturning circulation. *Rev. Geophys.*, **45**(RG2001). doi:10.1029/2004RG000166.

Le Quéré, C., C. Rödenbeck, E. T. Buitenhuis, T. J. Conway, R. Langenfelds, A. Gomez, C. Labuschagne, M. Ramonet, T. Nakazawa, N. Metzl, N. Gillett, and M. Heimann, 2007: Saturation of the Southern Ocean CO_2 sink due to recent climate change. *Science*, **316**, 1735–1738. doi:10.1126/science.1136188.

Lee, M.-M. and A. C. Coward, 2003: Eddy mass transport for the Southern Ocean in an eddy-permitting global ocean model. *Ocean Modelling*, **5**, 249–266.

Lee, M.-M., A. J. Nurser, A. C. Coward, and B. A. de Cuevas, 2007: Eddy advective and diffusive transports of heat and salt in the Southern Ocean. *J. Phys. Oceanogr.*, **37**, 1376–1393.

Levitus, S., J. I. Antonov, T. P. Boyer, R. A. Locarnini, H. E. Garcia, and A. V. Mishonov, 2009: Global ocean heat content 1955-2008 in light of recently revealed instrumentation problems. *Geophys. Res. Letters*, **36**(L07608). doi:10.1029/2008GL037155.

Lovenduski, N. S., N. Gruber, S. C. Doney, , and I. D. Lima, 2007: Enhanced CO_2 outgassing in the Southern Ocean from a positive phase of the Southern Annular Mode. *Glob. Biochem. Cycles*, **21**(GB2026). doi:10.1029/2006GB002900.

Lovenduski, N. S., N. Gruber, and S. C. Doney, 2008: Toward a mechanistic understanding of the decadal trends in the Southern Ocean carbon sink. *Glob. Biochem. Cycles*, **22**(GB3016). doi:10.1029/2007GB003139.

Marshall, G., P. A. Stott, J. Turner, W. M. Connolley, J. C. King, and T. A. Lachlan-Cope, 2004: Causes of exceptional atmospheric circulation changes in the Southern Hemisphere. *Geophys. Res. Letters*, **31**(L14205). doi:10.1029/2004GL019952.

Marshall, G. J., 2003: Trends in the Southern Annular Mode from Observations and Reanalyses. *J. Climate*, **16**, 4134–4143.

Marshall, J., D. Olbers, H. Ross, and D. Wolf-Gladrow, 1993: Potential vorticity constraints on the dynamics and hydrography of the Southern Ocean. *J. Phys. Oceanogr.*, **23**, 465–487.

Marshall, J. and T. Radko, 2003: Residual-mean solutions for the Antarctic Circumpolar Current and its associated overturning circulation. *J. Phys. Oceanogr.*, **33**, 2341–2354.

Marshall, J., E. Shuckburgh, H. Jones, and C. Hill, 2006: Estimates and implications of surface eddy diffusivity in the Southern Ocean derived from tracer transport. *J. Phys. Oceanogr.*, **36**, 1806–1821.

McDougall, T. J. and P. C. McIntosh, 1996: The temporal-residual-mean velocity. Part I: Derivation and the scalar conservation equations. *J. Phys. Oceanogr.*, **26**, 2653–2665.

McDougall, T. J. and P. C. McIntosh, 2001: The temporal-residual-mean velocity. Part II: Isopycnal interpretation and the tracer and momentum equations. *J. Phys. Oceanogr.*, **31**, 1222–1246.

McIntosh, P. and T. McDougall, 1996: Isopycnal averaging and the residual mean circulation. *J. Phys. Oceanogr.*, **26**, 1655–1660.

McNeil, B. I., N. Metzl, R. M. Key, R. J. Matear, and A. Corbiere, 2007: An empirical estimate of the Southern Ocean air-sea CO_2 flux. *Glob. Biochem. Cycles*, **21**(GB3011). doi:10.1029/2007GB002991.

Medvedev, A. S. and R. J. Greatbatch, 2004: On advection and diffusion in the mesosphere and lower thermosphere: The role of rotational fluxes. *J. Geophys. Res.*, **109**(D07104). doi:10.1029/2003JD003931.

Meehl, G. A., T. F. Stocker, W. D. Collins, P. Friedlingstein, A. T. Gaye, J. M. Gregory, A. Kitoh, R. Knutti, J. M. Murphy, A. Noda, S. C. B. Raper, I. G. Watterson, A. J. Weaver, and Z.-C. Zhao, 2007: *Climate Change 2007: The Physical Science Basis. Contribution of Working Group I to the Fourth Assessment Report of the Intergovernmental Panel on Climate Change*, chapter Global Climate Projections, pp. 747–845. Cambridge University Press, Cambridge, UK and New York, USA.

Meredith, M. P. and A. M. Hogg, 2006: Circumpolar response of Southern Ocean eddy activity to a change in the Southern Annular Mode. *Geophys. Res. Letters*, **33**(L16608). doi:10.1029/2006GL026499.

Mikaloff Fletcher, S. E., N. Gruber, A. R. Jacobson, S. C. Doney, S. Dutkiewicz, M. Gerber, M. Follows, F. Joos, K. Lindsay, D. Menemenlis, A. Mouchet, S. A. Müller, and J. L. Sarmiento, 2006: Inverse estimates of anthropogenic CO_2 uptake, transport, and storage by the ocean. *Glob. Biochem. Cycles*, **20**(GB2002). doi:10.1029/2005GB002530.

Mikaloff Fletcher, S. E., N. Gruber, A. R. Jacobson, M. Gloor, S. C. Doney, S. Dutkiewicz, M. Gerber, M. Follows, F. Joos, K. Lindsay, D. Menemenlis, A. Mouchet, S. A. Müller, and J. L. Sarmiento, 2007: Inverse estimates of the oceanic sources and sinks of natural CO_2 and the implied oceanic carbon transport. *Glob. Biochem. Cycles*, **21**(GB1010). doi:10.1029/2006GB002751.

Munk, W. and E. Palmén, 1951: Note on the dynamics of the Antarctic Circumpolar Current. *Tellus*, **3**, 53–55.

Nurser, A. J. G. and M.-M. Lee, 2004a: Isopycnal averaging at constant height. Part I: The formulation and a case study. *J. Phys. Oceanogr.*, **34**, 2721–2739.

Nurser, A. J. G. and M.-M. Lee, 2004b: Isopycnal averaging at constant height. Part II: Relating to the residual streamfunction in Eulerian space. *J. Phys. Oceanogr.*, **34**, 2740–2755.

Nycander, J., J. Nilsson, K. Döös, and G. Broström, 2007: Thermodynamic analysis of ocean circulation. *J. Phys. Oceanogr.*, **37**, 2038–2052.

Oke, P. R. and M. H. England, 2004: On the oceanic response to changes in the latitude of the Southern Hemisphere subpolar westerly winds. *J. Climate*, **17**, 1040–1054.

Olbers, D., Borowski, C. D. Völker, and J.-O. Wolff, 2004: The dynamical balance, transport and circulation of the Antarctic Circumpolar Current. *Anarctic Science*, **16**(4), 439–470.

Olbers, D. and V. O. Ivchenko, 2001: On the meridional circulation and balance of momentum in the Southern Ocean of POP. *Ocean Dyn.*, **52**, 79–93.

Olbers, D. and M. Visbeck, 2005: A zonally averaged model of the meridional overturning in the Southern Ocean. *J. Phys. Oceanogr.*, **35**, 1190–1205.

Olbers, D., J. Willebrand, and C. Eden, 2011: *Ocean dynamics*. Springer.

Oreskes, N., 2004: The scientific consensus on climate change. *Science*, **306**, 1686. doi:10.1126/science.1103618.

Orr, J., E. Maier-Reimer, U. Mikolajewicz, P. Monfray, J. L. Sarmiento, J. R. Toggweiler, N. K. Taylor, J. Palmer, N. Gruber, C. L. Sabine, C. Le Quere, R. M. Key, and J. Boutin, 2001: Estimates of anthropogenic carbon uptake from four three-dimensional global ocean models. *Glob. Biochem. Cycles*, **15**(1), 43–60.

Phillips, H. E. and S. R. Rintoul, 2000: Eddy variability and energetics from direct current measurements in the Antarktic Circumpolar Current south of Australia. *J. Phys. Oceanogr.*, **30**, 3050–3076.

Polton, J. A. and D. P. Marshall, 2007: Overturning cells in the Southern Ocean and subtropical gyres. *Ocean Sci.*, **3**, 17–30.

Rintoul, S. R., C. Hughes, and D. Olbers, 2001: *Ocean Circulation and Climate*, chapter The Antarctic Circumpolar Current system, pp. 271–302. Academic Press, New York, USA.

Sabine, C. L., R. A. Feely, N. Gruber, R. M. Key, K. Lee, J. L. Bullister, R. Wanninkhof, C. S. Wong, D. W. R. Wallace, B. Tilbrook, F. J. Millero, T.-H. Peng, A. Kozyr, T. Ono,

and A. F. Rios, 2004: The oceanic sink for anthropogenic CO_2. *Science*, **305**, 367–371. doi:10.1126/science.1097403.

Saenko, O. A., J. C. Fyfe, and M. H. England, 2005: On the response of the oceanic wind-driven circulation to atmospheric CO_2 increase. *Climate Dyn.*, **25**, 415–426. doi:10.1007/s00382-005-0032-5.

Siedler, G., J. Church, and J. Gould (eds.), 2001: Ocean circulation and climate. *Academic Press*.

Speer, K., S. R. Rintoul, and B. Sloyan, 2000: The Diabatic Deacon Cell. *J. Phys. Oceanogr.*, **30**(12), 3212–3222.

Stevens, D. P. and V. O. Ivchenko, 1997: The zonal momentum balance in an eddy-resolving general-circulation model of the Southern Ocean. *Quart. J. Royal Met. Soc.*, **123**, 929–951.

Straub, D. N., 1993: On the transport and angular momentum balance of channel models of the Antarctic Circumpolar Current. *J. Phys. Oceanogr.*, **23**, 776–782.

Tansley, C. E. and D. P. Marshall, 2001: On the dynamics of wind-driven circumpolar currents. *J. Phys. Oceanogr.*, **31**, 3258–3273.

Thompson, D. W. J. and S. Solomon, 2002: Interpretation of recent Southern Hemisphere climate change. *Science*, **296**, 895–899. doi:10.1126/science.1069270.

Townsend, R. D. and D. R. Johnson, 1985: A diagnostic study of the isentropic zonally averaged mass circulation during the first garp global experiment. *J. Atmos. Sci.*, **42**, 1565–1579.

Treguier, A. M., M. H. England, S. R. Rintoul, G. Madec, J. Le Sommer, and J.-M. Molines, 2007: Southern Ocean overturning across streamlines in an eddying simulation of the Antarctic Circumpolar Current. *Ocean Sci.*, **3**, 491–507.

Viebahn, J. and C. Eden, 2010: Towards the impact of eddies on the response of the Southern Ocean to climate change. *Ocean Modelling*, **34**, 150–165.

Viebahn, J. and C. Eden, 2012: Standing eddies in the meridional overturning circulation. *J. Phys. Oceanogr.*. doi:10.1175/JPO-D-11-087.1.

Visbeck, M., J. Marshall, T. Haine, and M. Spall, 1997: Specification of eddy transfer coefficients in coarse-resolution ocean circulation models. *J. Phys. Oceanogr.*, **27**, 381–402.

Walin, G., 1982: On the relation between sea-surface heat flow and thermal circulation in the ocean. *Tellus*, **34**, 187–195.

Webb, D. J. and N. Suginohara, 2001: Vertical mixing in the ocean. *Nature*, **409**(6816), 37.

Wüst, G., 1935: Schichtung und Zirkulation des Atlantischen Ozeans. Die Stratosphäre des Atlantischen Ozeans. *Wiss. Ergebn. Dt. Atlant. Exped. "Meteor" 1925–1927*, **6**, 109–288.

Zickfeld, K., J. C. Fyfe, O. A. Saenko, M. Eby, and A. J. Weaver, 2007: Response of the global carbon cycle to human-induced changes in Southern Hemisphere winds. *Geophys. Res. Letters*, **34**(L12712). doi:10.1029/2006GL028797.